BIOLOGICAL, SIMULATION, AND ROBOTIC STUDIES TO DISCOVER PRINCIPLES OF SWIMMING WITHIN GRANULAR MEDIA

A Thesis
Presented to
The Academic Faculty

by

Ryan D. Maladen

In Partial Fulfillment
of the Requirements for the Degree
Doctor of Philosophy in the
Interdisciplinary Bioengineering Graduate Program
Department of Biomedical Engineering

Georgia Institute of Technology
December 2010

BIOLOGICAL, SIMULATION, AND ROBOTIC STUDIES TO DISCOVER PRINCIPLES OF SWIMMING WITHIN GRANULAR MEDIA

Approved by:

Dr. Daniel I. Goldman, Advisor
School of Physics
Georgia Institute of Technology

Dr. Young-Hui Chang
School of Applied Physiology
Georgia Institute of Technology

Dr. Shella Keilholz
Department of Biomedical Engineering
Georgia Institute of Technology & Emory University

Dr. Hang Lu
School of Chemical & Biomolecular Engineering
Georgia Institute of Technology

Dr. Jeanette Yen
School of Biology
Georgia Institute of Technology

Date Approved: 1^{st} November 2010

To my parents, who inspired me to challenge myself always

ACKNOWLEDGEMENTS

This PhD work was possible due to the support of a number of special people who have influenced me both as a person and a researcher.

I would like to thank my PhD advisor, Dr. Daniel I. Goldman for taking the 'risk' and recruiting me as a graduate student even before arriving on site at Georgia Tech. His hard work and dedication to doing good science has been a key motivator and guide to helping me improve my abilities as a researcher and a communicator of my research. I also thank him for the opportunity to pursue aspects of the research that interested me the most, while teaching me to keep in mind the big picture. Most of all, I thank him for the opportunity to work on the fascinating project presented here.

I would like to thank my committee members for their mentoring and support during this project. Working with Dr. Lu, Dr. Yen, Dr. Keilholz, and Dr. Chang provided a unique and multi-disciplinary educational experience. Their ideas and expertise made a valuable contribution to this project. I would like to specially thank Dr. Chang for introducing me to my advisor and the potentially interesting work I could do with him. A special thanks to Dr. Lena Ting without whose encouragement and advice I would not have reached Georgia Tech to pursue my doctoral studies. I would also like to acknowledge all the members of the CRAB Lab, specially the graduate students - Yang Ding, Chen Li, Niole Mazouchova, Andrei Savu, Nick Gravish, and Sarah Steinmetz, for always being available to bat around research ideas and being a fun group to work with. I am deeply grateful to Dr. Paul Umbanhowar of Northwestern University for the long discussions that helped me sort out the technical details of my work and his critical guidance in bringing the robotic component of this work to fruition. A special thanks to the various under-graduates I have had the opportunity to mentor over the years and whose help was invaluable to putting together the work presented here - Mateo Garcia, Adam Kamor, Danny Guigou, and Andrew Masse.

I would like to thank Dr. Elizabeth Brainerd, Brown University for inviting me to

her laboratory to learn the x-ray imaging techniques that formed an essential part of the biological experiments presented here. I would also like to thank Dr. Tonia Hsieh, Temple University for accompanying me on a field trip to the Mojave desert, and teaching me essential field biology skills.

Special thanks to all the administrative staff in the School of Physics, the BME and the Bioengineering programs, specially - Vicki Speights, Debbie James, Felicia Goolsby, Keith Garner, Chris Ruffin, Sally Gerrish, Beth Bullock, and Shannon Sullivan - whose help at various points in the PhD program made the mundane but critical paperwork components of the PhD painless. I would also like to acknowledge the National Science Foundation (NSF) and the Burroughs Wellcome Fund for supporting my research over the past four years.

I would like to dedicate this work to my parents – Olga and Dominic Maladen, without whose endless struggles and sacrifices I would not have been able to pursue graduate studies in the US. I thank them for their seamless trust in my judgment when I decided to move away from human rehabilitation research (which was focused on improving the quality of life of the impaired), to studying lizard locomotion. Their ability appreciate and understand the choices I've made over the years, and their unbridled happiness and excitement for my every achievement has and always will be a source of encouragement and inspiration - thank you so much Mum and Dad.

I would also like to thank my sister, Michelle Percy, who made coming and acclimatizing to a new country easy. She has always been available to lend a ear and advice me on dealing with the endless barrage of issues that cropped up over the years. She always made me believe that I was doing the best research around ! Thanks Mich, I've learned and am sure will continue to learn much from you. I would also like to thank my brother-in-law, Dennis Percy, for being extremely supportive and for always making sure I had a great time whenever we met. Thanks also to my God-daughter, Diya Caroline, whose sense of humor has been source of entertainment when work was really too taxing. Over the past 2 years, I have also been blessed with the love and support of another family, my in-laws Dr. Mercy Joseph and Joseph Chacko, and Joveeta, Christopher, Rhea, and Neil Ruben. Thank you

all for your love and constant words of encouragement.

I have also had the good fortune of finding an great group of friends, who have made the troughs of the PhD process momentary and fleeting. I would specially like to thank Stephen Brink for his scientific intellect and easy going nature that always made him fun to hang out with. The camaraderie over past four years that involved countless Taco-bell trips, NBA heartaches, and deep scientific discussions while running the Pi mile around Tech, that led to us being grooms men for each others weddings. I'd also like to thanks Drs. Kartik Sundar, Abbey Wojtowicz, and Rekha Nair for the crazy halloween costume parties,and various other occasions we celebrated together. Hanging out with my 'desi' gang – Vijay Balasubramian, Karishma Babu, Arpan Ghosh, Ranjith Subramanian, Pavithra Vembu, and Nivedhya Ramaswamy was always a delight and a key to surviving the rigors of graduate school. I really like to thank Nick Gravish who has been a great friend over the past years. Work in the lab and our travels to various conferences and Africa was great fun owing to his unwavering company when posed with the option of taking a break at a watering hole to cope with the pressures of research at the CRAB lab. Few additional friends that deserve special mention are Lauren Reese, Yang Ding, Chen Li, Andrei Savu, Sarah Steinmetz, Nicole Mazouch, Rachel Whitmire, Jay Sy, and Dr. Murali Padala who have helped make the PhD experience really memorable. I would also like thank my undergraduate friends back home in India for their unfailing support over the many years in my abilities, Navneet Singh, Ashish Uchil, Manish Agarwal, Vikas Garg, Mohammad Jhanjhariya, and Neil Castelino. I would specially like to thank Dr. Prakriti Parijat for always being around to listen to me. I would also like to thank Trisha Kesar, for being a great friend over all these years. A special thanks also to Drs. Thommen Korah and Anoop Mathew for encouraging and advising me over all these years, you have both been great friends.

Finally, my greatest achievement at Georgia Tech has undoubtedly been convincing my wife, Dr. Laveeta Joseph-Maladen, to marry me. Thank you my love for being extremely patient with my demanding work schedule, crazy soccer obsession, and my inability to work through any important non-scientific paperwork. You have and will always continue to be my biggest source of happiness and encouragement and thank you for pushing me to realize

my potential. Georgia Tech and the PhD will always be special, because of you!

TABLE OF CONTENTS

LIST OF TABLES

LIST OF FIGURES

SUMMARY

The locomotion of organisms whether by running, flying, swimming, or crawling, is the result of multiple degree-of-freedom nervous and musculoskeletal systems interacting with an environment that often flows and deforms in response to movement. Nearly all experiments and models of terrestrial locomotion have been developed for running and walking on rigid, flat, no-slip frictional substrates for which the complication of substrate flow is not considered. In contrast, complexity in interaction with the environment in aquatic and aerial locomotion (swimming and flying) is well recognized and determining mechanisms for drag or lift in these media is always possible in principle by solving Navier-Stokes hydrodynamics in the presence of moving boundary conditions. A major challenge in biology is to understand the locomotion of organisms that walk, crawl, or burrow on or within terrestrial substrates like sand, soil, and muddy sediments that display both solid and fluid-like behavior. In such materials, validated theories such as the Navier-Stokes equations for fluids do not exist, and visualization techniques [such as particle image velocimetry in fluids] are nearly nonexistent.

In this dissertation we integrated biological experiment, numerical simulation, and a physical robot model to reveal principles of undulatory locomotion in granular media. First, we used high speed x-ray imaging techniques to reveal how a desert dwelling lizard, the sandfish, swims within dry granular media without limb use by propagating a single period traveling sinusoidal wave along its body, resulting in a wave efficiency η, the ratio of its average forward speed to wave speed, of approximately 0.5. The wave efficiency was independent of the media preparation (loosely and closely packed). We compared this observation against two complementary modeling approaches: a numerical model of the sandfish coupled to a discrete particle simulation of the granular medium, and an undulatory robot which swims within granular media. We used these mechanical models to vary the ratio of undulation

amplitude (A) to wavelength (λ) and demonstrated that an optimal condition for sand-swimming exists that results from competition between η and λ. The animal simulation and robot model, predicted that for a single period sinusoidal wave, maximal speed occurs for $A/\lambda = 0.2$; the same kinematics used by the sandfish. Finally, inspired by the tapered head shape of the sandfish lizard, we demonstrated that the lift forces and hence vertical position of the sand-swimming robot as it moves forward within granular media can be controlled by varying its head shape. These results support the biological hypotheses which propose that morphological adaptations of desert dwelling organisms aid in their subsurface locomotion. This work also demonstrates that the discovery of biological principles of high performance locomotion within sand can help create the next generation of biophysically inspired robots that could explore potentially hazardous complex flowing environments.

CHAPTER I

INTRODUCTION

The locomotion of organisms [3], whether by running, flying, swimming or crawling, is the result of multiple degree of freedom nervous and musculo-skeletal systems interacting with an environment that often flows and deforms in response to movement. Nearly all experiments and models of terrestrial locomotion have been developed for running and walking on rigid, flat, no-slip substrates in which the possible complication of substrate flow has been ignored, and for which foot interaction is mainly frictional. In contrast, complexity in interaction with the environment in aquatic and aerial locomotion (i.e. flying and swimming) is well recognized [116]. Determining mechanisms for lift or drag in these environments is always possible in principle, they require solving Newtonian Navier-Stokes hydrodynamics in the presence of moving boundary conditions. A frontier in biology is to understand locomotion of organisms that walk, crawl or burrow on or *within* terrestrial substrates like dirt, debris and sand that can act like both solids and fluids. In such materials, validated theory at the level of fluids (the equations of motion like Navier-Stokes) do not exist, and visualization techniques like Particle Image Velocimetry (PIV) in fluids [71] are nearly non-existent.

With observations from biological organisms that interact with complex substrates as motivation, the development of animal-inspired mechanical models that couple the dynamics of the locomotor to its environment allows us to vary parameters that are difficult to vary/explore with an organism and can thus address questions concerning optimal kinematics and morphology, mechanical cost of transport, maneuvering, and control. These models can be used as design tools to develop the next generation of biophysically inspired robots that could explore potentially hazardous complex flowing environments like those following disasters like earthquakes and cave-ins. Such models could also be used to evaluate biological hypotheses on the locomotion and morphological adaptation of organisms that move

within these substrates.

1.1 Specific Aims

The overall goal of this work was to discover principles that maximize the swimming speed within granular media. To achieve this I studied the subsurface sand-swimming ability of a desert dwelling lizard using high speed x-ray imaging techniques. I utilized a numerical simulation to test biological hypotheses of sand-swimming, and also used it as a design tool to develop a biophysically inspired sand-swimming robot. I then used these mechanical models in conjunction with the biological observations to establish principles for high performance swimming in sand.

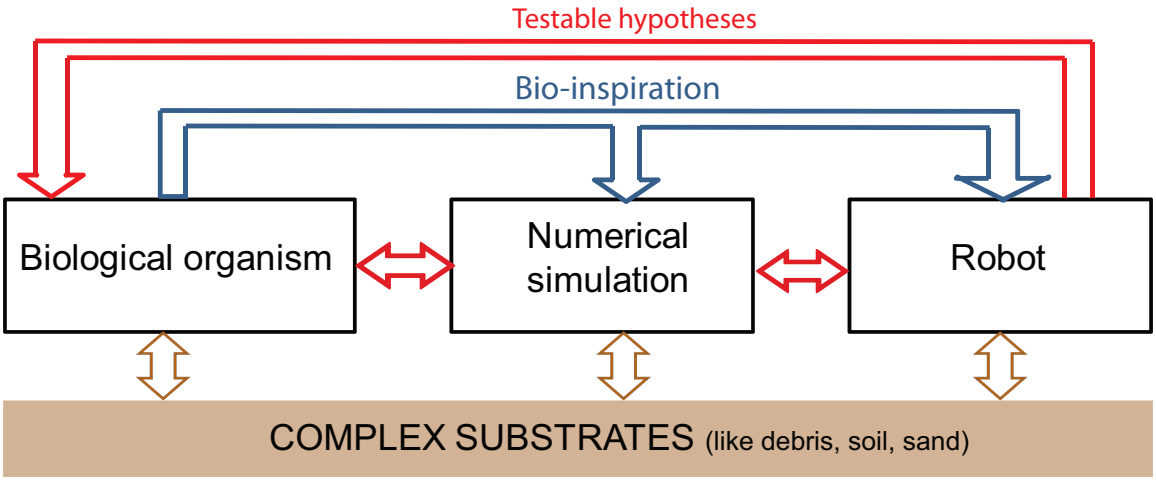

Figure 1: Block diagram of the approach utilized in this dissertation to discover principles of locomotion within complex substrates. The blue and red arrows correspond to 'bio-inspiration' and 'testable hypotheses', respectively.

Specific Aim 1: To study the subsurface locomotion of a small desert dwelling lizard, the sandfish, using high speed x-ray imaging techniques.

Study 1 A: Characterize body and limb use of the sandfish as it swims subsurface.

Study 1 B: Characterize the effect of media preparations on the subsurface kinematics of the sandfish.

Study 1 C: Characterize the effect of particle size on the subsurface kinematics of the sandfish.

Specific Aim 2: To utilize a numerical sandfish simulation to study the effect of kinematic parameters on subsurface locomotion.

Study 2 A: Investigate the effect of varying the amplitude of undulation (for a single period wave) on sand-swimming performance.

Study 2 B: Investigate the effect of number of periods of undulation (for a fixed amplitude of undulation) on sand-swimming performance.

Study 2 C: Identify an optimal kinematics condition that maximizes the speed of the sandfish subsurface.

Specific Aim 3: To design a robot inspired by the sand-swimming ability of the sandfish, compare its performance to biological observations, and test the predictions of the numerical simulation in a real world environment.

Study 3 A: Compare the performance of the physical sand swimming robot to the animal, and explain the differences in performance using a numerical robot simulation.

Study 3 B: Investigate the effect of varying kinematic parameters (as in Study 2 A and B) on the sand-swimming performance of the physical and simulated robot.

Study 3 C: Test the predicted optimal kinematics condition (Study 2 C) using the physical and simulated robot.

Study 3 D: Investigate the effect of head morphology on sand-swimming performance using the physical robot.

1.2 Biological background and significance

Animal burrowing and movement within ground is as common [3, 25] as movement on solid ground, but has not been studied or modeled to the same extent [3]. Studying the movement of organisms within complex substrates like sand, brush, and dirt helps in discovering locomotion principles such as which kinematics optimize performance parameters like speed and stability, and also allows us test biological hypotheses of how morphological adaptations of these animals aid in their locomotor ability. Such studies can also provide insight into the ecological significance of animal burrowing and subterranean locomotion.

1.2.1 Ecological significance of subsurface locomotion

Animals move within complex materials by using various modes of locomotion, e.g., earthworms use peristalsis [3] and nereidid polychaetes [32] use undulation to burrow and move within wet mud and soils, while desert moles [108] and crabs [21, 49] use their limbs to burrow into dry desert and beach sand. As each of these organisms burrow they participate in the biological reworking of the medium in a process referred to as bioturbation [87].

The importance of bioturbation for soil processes and geomorphology was first realized by Darwin in his last scientific work [26]. In modern ecological theory, bioturbation is recognized as an example of ecosystem engineering, modifying geochemical gradients,redistributing food resources, viruses, bacteria,resting stages and eggs. Observing animal behavior in sediments is useful for quantifying their influence on the physical, chemical, and microbiological properties of the mediums in which they live [16]. Furthermore, contaminants in these substrates can influence their burrowing behavior [95], and variations in this behavior can be used as an indicator of potentially hazardous pollutants. From an evolutionary perspective, recent investigations provide evidence that bioturbation had a key role in the evolution of metazoan life at the end of the Precambrian Era [87].

Bioturbation by animals in the desert generally occurs in areas with lower daytime temperatures and the more abundant food sources, like under the canopy of dominant shrubs which often leads to a further increase in foliage in these areas [109]. A recent study on the landscape evolution in the Northern Mojave Desert reported that over time sites

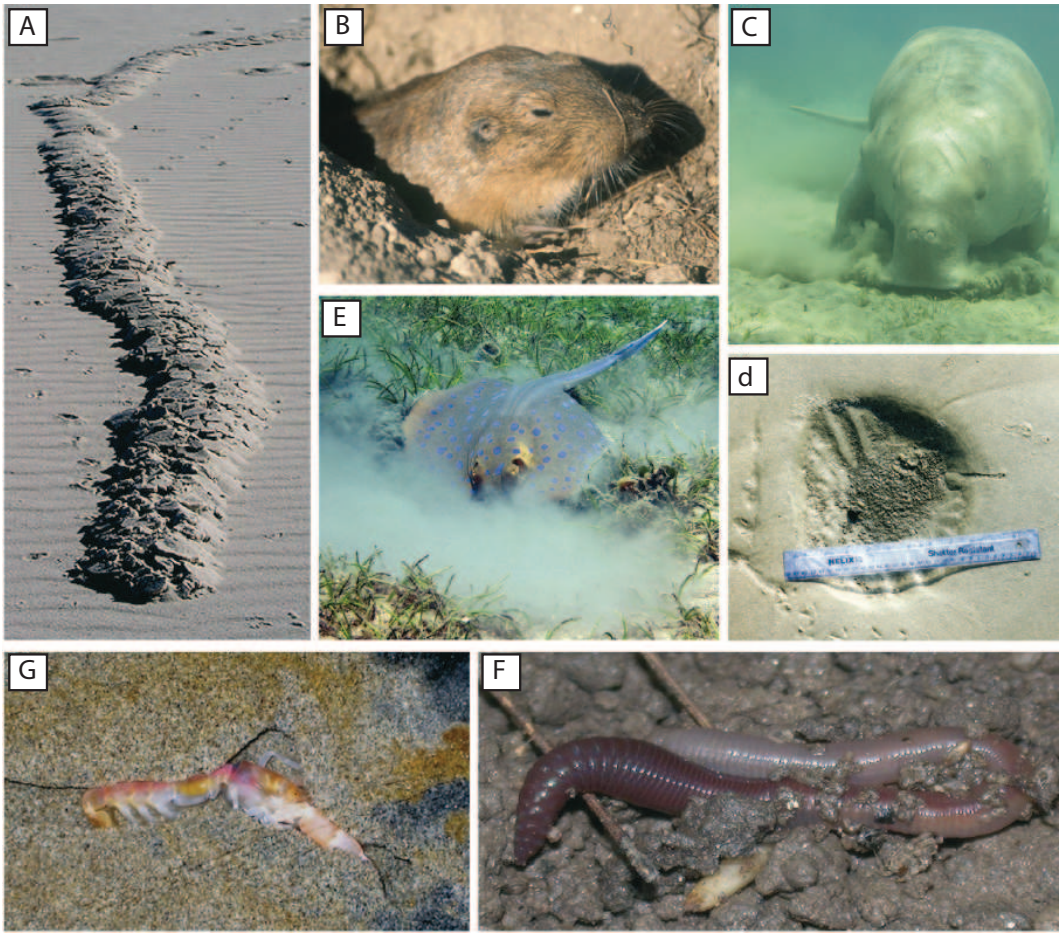

Figure 2: Bioturbation results from a range of animal activities. (A) Insectivorous moles and (B) herbivorous pocket gophers in prairie grasslands.(C) In sea grass meadows, large-sized pits and trails are created by herbivores, such as dugong feeding on rhizomes. On tidal flats, (D) smaller feeding pits attributed to stingrays. Small invertebrates have a dominant from a global perspective because of their sheer abundance and ubiquity; examples include ants, termites and (F) the common earthworm. In the marine environment, the predominant bioturbators are deposit-feeding polychaetes and various burrowing crustaceans, such as (E) burrowing shrimp. Figure reproduced from [87].

of once active burrows that had collapsed trapping seed caches deposited by the animals and animal waste, had become the location of new shrubs [109]. The burrowing of animals near the roots of these desert plants prevents the soil surface under the plant canopies from hardening and allows focused water infiltration closer to the root mass [110].

1.2.2 Locomotion within desert sand

Desert sand (which covers 6-10% of land surface [35]) is a granular material composed of a collection of particles that interact through dissipative contact forces and in bulk can

display solid and fluid-like features [63]) which disturbed. Within this environments live a number of desert organisms like scorpions, snakes and lizards that move within sand to escape heat and predators, and hunt for prey [6, 119, 99].

1.2.2.1 Subsurface locomotion of desert lizards

A number of desert-dwelling lizards found in open dune environments where they are often exposed to predators due to the lack of refuges like open burrows or vegetation have evolved submerging rapidly into sand as a mode of predator avoidance [7]. Within the same desert environment however there are instances of lizards that have evolved sand burying techniques while other in the same environment have not. Groups that have expanded along ecological continua into habitats with specialized requirements often have robust phylogenies and many clades with terminal sand-diving groups fits this pattern [5].

Sand-diving behaviour has evolved separately in *Uma* and other closely related lizards and in some *Phrynosoma* and *Sceloporus* (Phrynosomatidae, North America), *Phrynocephalus* and its sister-group *Bufoniceps* (Agamidae, south-west and central Asia), *Agama etoshae* (Agamidae, Namibia), some Meroles (Lacertidae, south-west Africa), *Scincus* (Scincidae, North Africa and Arabia), and *Angolosaurus* (Gerrhosauridae, Africa) [7]. Methods of rapidly burying in sand are varied among the independently evolved cases listed in Fig. 3. For example, some forms enter the sand head-first while others may sink vertically and, even when general modes of entry are similar, there may be marked differences in the way these are achieved and in the way the tail is finally concealed [7].

Subterranean activity of desert dwelling lizards are of three types [99, 90]: (1) True burrowers that construct open burrows in firm soils like amphisbaedids. (2) Quiescent burrowers like the *Phrynocephalus* that are cursorial species, many of which can run at high speeds over the surface, and are also able to burrow. They do not, however, proceed beneath the surface of the sand for any considerable horizontal distance. (3) Sand swimmers, such as *Scincus* and *Chionactis*, who move freely through sand and spend much of their time buried but do not construct burrows. The last type of lizards are true subterranean forms and have been referred to as 'subarenaceous' to distinguish them from other subterranean forms.

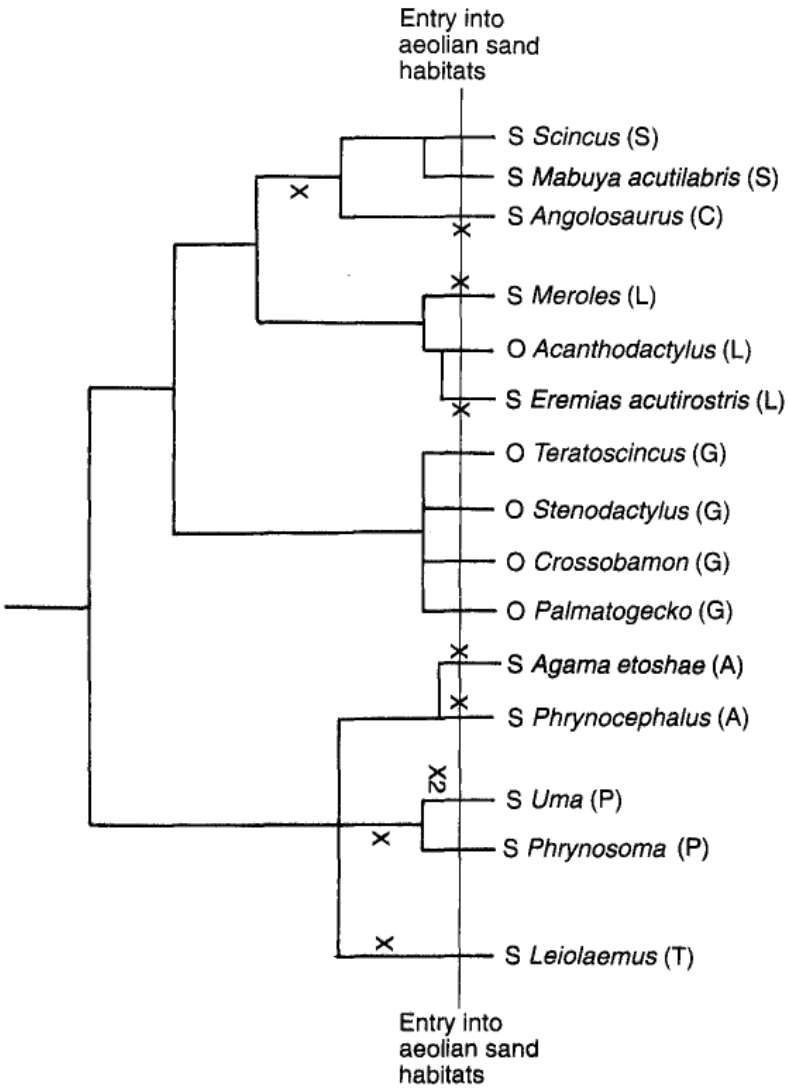

Figure 3: Phylogenetic relationships of the desert-dwelling lizards. S- and O- correspond to sand diving, and not sand diving. X-Approximate position where basic pattern of burial first developed, X2 subsequent modification of basic pattern in *Uma* lineage. A-Agamidae, C-Gerrhosauridae, G-Gekkonidae, L-Lacertidae, P-Phrynosomatidae; S-Scincidae, T- Tropiduridae. Figure reproduced from [7].

The sand-diving techniques of species that are quiescent burrowers and sand swimmers with well-developed limbs show much variation [99, 90, 7].

Quiescent burrowers employ many different techniques to bury themselves into sand. The *Lacertids* of the genus *Meroles* use all limbs and serpentine body movements to dive into the sand and progress forward and into the medium at about $15-20^{\circ}$ from the horizontal [99, 7] (see Fig. 4). The agamids, *Phrynocephalus* and *Agama etoshae* employ lateral body

oscillations and descend vertically into the medium. The phrynosomatid, *Uma*, oscillates its head at a high frequency, folds its forelimbs back and supplements the thrust with its hind limbs while the scales on the upper arms act like ratchets. This basic pattern of motion is used for rapid diving in compact sand with the snout hypothesized to act like a reciprocating drill. *Phrynosoma* species which has a similar blunt head shape as that of the *Uma* also buries rapidly into sand but like *Phrynocephalus* does so with a strong vertical component.

True sand swimmers like the scincid, *Scincus* and gerrhosaurid, *Angolosaurus*, both use high amplitude sinusoidal movements of the body and tail to move within sand. Arnold observed that the sand-swimming lizard, *Scincus mitranus* entered loose sand by turning its snout steeply downward and plunging into the sand, and then raising itself to a shallower angle [7]. Arnold also observed that at slow burial speeds, normal walking movements of the limbs helped propel the lizard forward into the material initially. As the forelegs became submerged they were laid back along the body, but the hind legs were laid back along the body while they were still fully exposed. As the lizard entered the sand, the head and foreparts were flexed laterally in one direction and then in the other. When the body was approximately half buried, the whole animal assumed a sinusoidal body form and from this stage the locomotion was hypothesized to be essentially serpentine with the body and tail of the lizard following the high-amplitude sinusoidal course adopted by the head, with the limbs placed along its side [7]. A recent study using nuclear magnetic resonance (NMR) to visualize subsurface motion of the sandfish lizard proposed that the animal used its limbs in a paddling motion along with body undulations on its body to generate thrust subsurface (see Fig. 6). However, the observation quality and number of trials were limited [10].

The main indication that the high performance locomotor behavior of subsurface sand-swimming occurs to avoid pursuit is evident from the number of species that employ this mode when fleeing while resorting to legged locomotion during foraging. Another indication is that the burial into sand is primarily carried out using the movements of normal surface locomotion i.e. fleeing lizards essentially run into the sand.

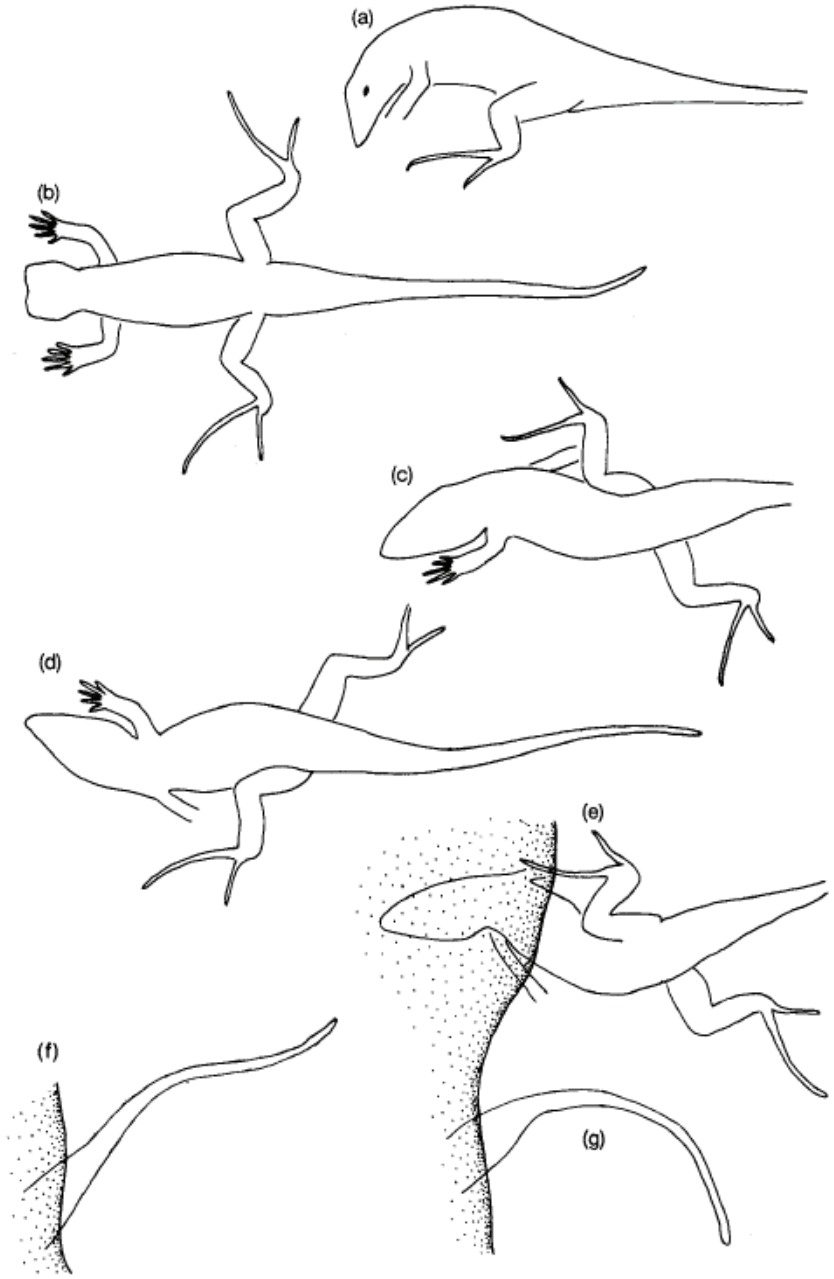

Figure 4: Sand diving in the lacertid lizard, *Meroles cuneirostris*: (a, b) head lowered and limbs turned forwards to some extent at beginning of dive; (c, d) use of both pairs of limbs; (e) forelimbs folded back as they enter the sand; (f, g) successive positions of the tail in the final stages of burial. Figure reproduced from [7].

1.2.3 Undulatory locomotion

One of the most common modes of locomotion for moving within fluids, specially for elongate organisms with no or reduced limbs is undulatory locomotion [40]. Undulatory locomotion

Figure 5: Hypothesized locomotion mode of a sand-swimming scincid, *Scincus mitranus*. As the foreparts enter the sand, the pairs of limbs are successively laid back along the body which is thrown into strong lateral sinusoidal waves that carry the lizard forward until it is completely buried. Figure reproduced from [7].

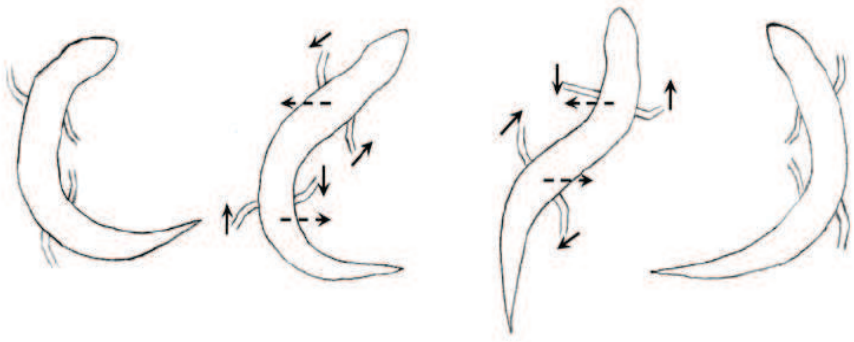

Figure 6: Diagrams of the subsurface locomotion ability of the sandfish using nuclear magnetic resonance (NMR) imaging. The study concluded that the animal used its limbs like paddles along with body undulations to locomote. Figure reproduced from [10].

is a means of self-propulsion that relies on the generation and propagation of waves along a body. Typically, to move in a given direction, the wave must propagate opposite to the direction of motion (i.e., from head to tail to achieve forward motion). This simple yet primitive mode of locomotion is prevalent across a range of biological scales from motile bacteria to gigantic prehistoric snakes [22].

Animals use a variety of different forms of undulation to locomote. These can crudely be classified into lateral or vertical, direct (in the direction of motion) or retrograde (opposite

the direction of motion) and longitudinal or transverse. Fish usually flap their bodies laterally, whereas whales and other marine mammals undulate up and down. All species of terrestrial limbless tetrapods can and often do make use of lateral undulation. It is also used by many non-limbless forms, particularly by species with an elongate trunk and relatively short legs, and by individuals that have been startled or excited [40].

Undulatory motion typically experiences the frictional or drag forces of the environment, rather than gravitational forces [22]. For instance, most swimmers like fish can float in water using buoyancy but need to optimize their kinematics to minimize energy expenditure while locomoting. Similarly for terrestrial undulators like lizards and snakes the proximity to the ground ensures that their motion is constrained by the frictional forces of the environment [22].

In the case of low Reynolds (Re) number swimmers like nematodes [48] and spermatozoa [47] the inertial forces become negligible. Previous studies have found that the undulations of such organisms are well fit by a traveling sinusoidal wave [13, 48, 69], which makes analyzing various wave parameters like amplitude and frequency for different test conditions possible. Since the movement of slender objects through a low Re number fluids is well understood [47] and theory for this regime well studied [75], the propulsive force of an undulating organism moving in an aqueous medium can be derived from the resistance encountered by each element of the body to displacement in a direction normal to its own surface and by knowing the characteristics of the wave traveling down the body. The organism progresses forward provided the coefficient of resistance to such displacement normally (thrust) is greater than that to displacement tangentially (drag) to its surface [47].

On the surface of terrestrial substrates, organisms like nematodes on an agar surface [48, 69, 13], and snakes on sand [46, 64, 65] progress forward by creating in their sinusoidal tracks (due to the lateral undulations) an indentation (or groove) which prevents them from slipping (discussed next).

Measure of performance in deformable media - Wave efficiency η

Under no slip conditions the speed of the animal's forward progression is equal to the speed at which the waves of muscular contraction pass backward relative to the head of the animal; the waves remain stationary relative to the ground and the animal leaves behind it a sinusoidal track whose wavelength and amplitude are the same as those of the muscular waves. The mechanics of the movement are identical with those of a snake gliding through a sinusoidal tube with rigid walls [46].

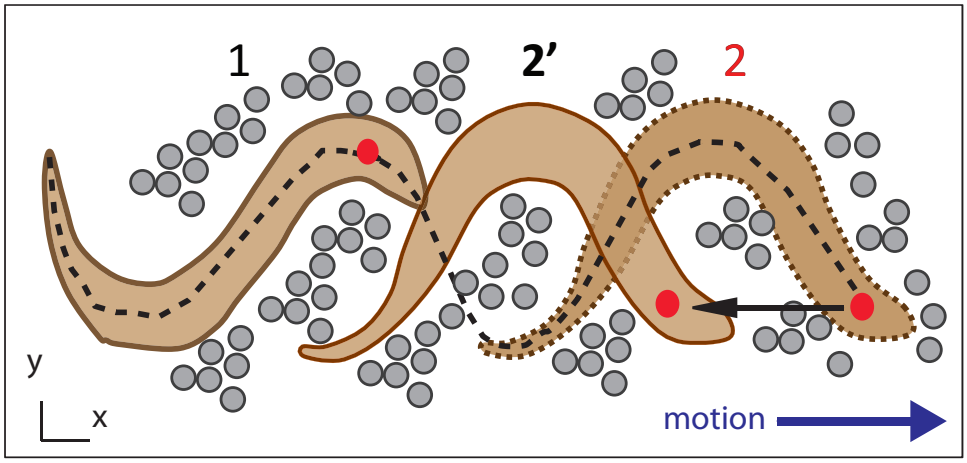

Figure 7: Wave efficiency η is a measure of kinematic performance in deformable media. For the same traveling wave propagating down the body of the organism its position at the end of time t would be: 2 if it is moving in a tube with rigid walls ($\eta = 1$), and $2'$ if moving in a deformable medium ($\eta < 1$). The position of the organism is measured relative to 1. The gray circular symbols correspond to a deformable media like sand.

While swimming in a deformable medium undulatory swimmers across scales (e.g. eels and spermatozoa in fluids) [47, 48, 42] progress a distance that is a percentage of its wavelength within a cycle of motion. The reduced performance is referred to as 'slip' and can be characterized by the wave efficiency ($\eta = 1-$ slip), defined as the ratio between the forward speed of the animal (v_x) and the velocity of the wave traveling down its body (v_w), i.e. $\eta = v_x/v_w$. Typical wave efficiencies of organisms in moving in fluids at low Re (like nematodes) are 0.25 [48], while undulating along the solid surface of an agar-air interface can have $\eta \approx 0.8$ [48].

1.2.3.1 Morphological adaptations of desert lizards

All species of limbless tetrapods can and often do progress forward by lateral undulations traveling caudally along the trunk [40]. Propulsion forces are exerted laterally and angled to the axis of travel. During terrestrial locomotion the weight of the organism acts normal to the ventral surface and imposes problems involving major changes in the supportive and muscular systems. Structural changes to these animals are generally considered to be twofold: modifications that facilitate motion in sand such as specializations of the locomotor apparatus involving body form (elongation, head shape, etc) and structure of the extremities (limb loss or reduction), and to protect sense organs and body openings [90].

Limb loss and body elongation of desert lizards

Many reptiles in the desert have evolved to have neither limbs nor limb girdles, while some have girdle remnants, short stumps or paddle-shaped limbs, or limbs with a reduced number of digits [90, 41]. Loss or reduction of limbs is generally correlated with elongation of the body. Reptiles with limbs reduced or absent always have a smaller body diameter for equivalent length from snout to caudal tip than do members of species in which the limbs are reduced only slightly or not at all. Also, the number of vertebrae is significantly higher in all species in which limbs are reduced or absent than in limbed forms [55].

The only mechanism that may have required a limit on the relative diameter of an animal is the ability to pass through crevices like a tunnel in rock (essentially incompressible substance), or within loose soil, sand, (material that can be compressed or displaced by the imposition of force). In such a case elongation would incur a selective advantage either by letting an animal pass through a greater percentage of crevices it encountered, or by permitting the passage through the crevice with a reduced investment of energy. Once elongation is initiated, being able to fold limbs to the sides might provide an advantage equivalent to diametric reduction. However, the overall selective balance would not be driven toward limb reduction until an alternative locomotor method were available - like lateral undulation that propel the organism by generating resistive forces when interacting with the media. A

necessary pre-condition to this transition however would be that the species be sufficiently elongate to undulate [41].

Head shape of desert lizards

Another defining characteristic of a true subarenaceous species like the *Chalcides sepoides* and *Scincus*, is found in the structure of its snout [90]. The lower jaw, considerably less in circumference, fits into the frame provided by the upper row of labials, so that the lower labials are at approximately the same level as the lower surface of the upper labials. Thus the lower jaw is concealed in profile view, counter-sunk into the upper, forming with it a continuous level surface (see Fig. 8) [90]. It has been hypothesized that this structure reduces the drag on the shovel shaped snout as the animal enters the material and protects the mouth from being forcibly opened when the animal locomotes through the sand. The smooth stream-lined head with angled upper labial scales that form a sharp lateral ridge allow the lizard to push its head into sand easily [7] (see Fig. 8).

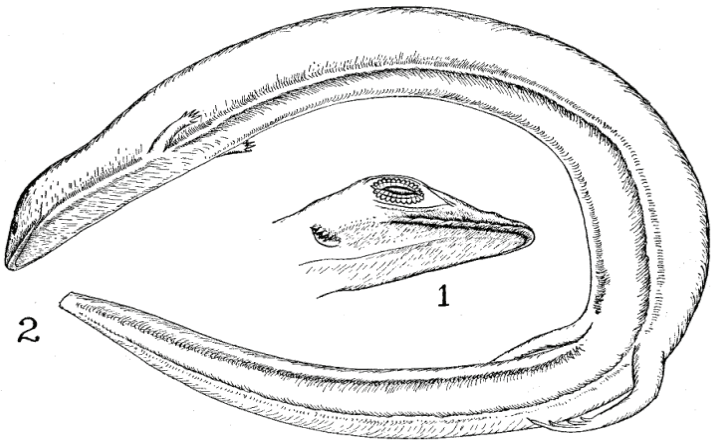

Figure 8: Head and body morphology of a sand-swimming lizard, the *Uma notata*. (1) Drawing of the head of *Uma notata*, showing the countersunk lower jaw, the peculiar eyelids and the scales overlapping the ear opening. (2) Drawing of *Chalcides sepoides* as representative of subarenaceous (see text for details) reptiles, showing the 'streamlined' head and body, the sharp snout, the countersunk lower jaw, and the slightly concave ventral surface. Figure reproduced from [90].

Arnold [7] hypothesized that when a lizard like the *Callisaurus* dives into dense substrate, its head acts like a reciprocating drill and, while not rotary, its action is similar to specialized bits, called multi-diameter cutters which are used for making large holes in dense materials (see Fig. 9). The structural adaptations of these subterranean lizards that live in firm soil differ distinctly from typical subarenaceous lizards. The former have blunt, rounded heads with very solidified skulls, that can withstand the pressure exerted on them by the firm medium, while the latter are noted to have sharp, keeled wedge-like heads which are suited for the loose sand only, which mechanically resembles a fluid medium [90] (see Fig. 8).

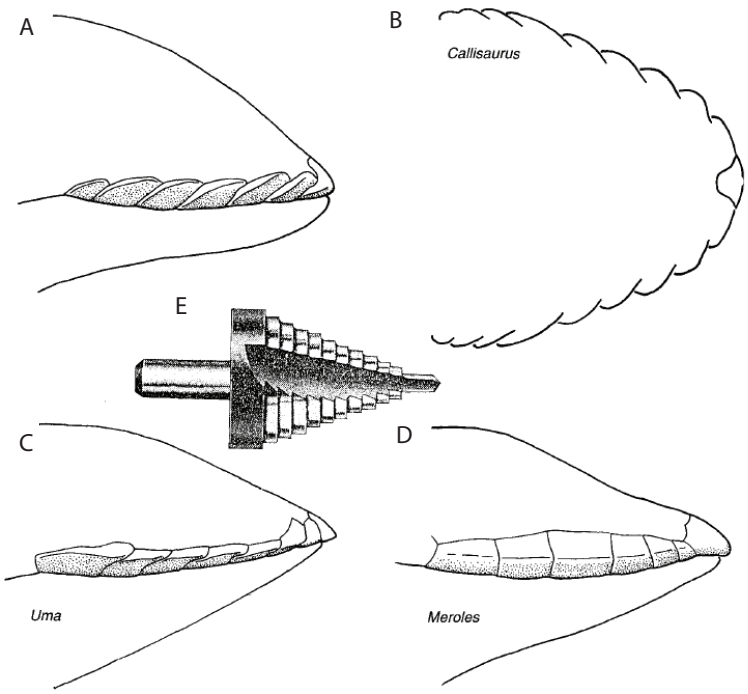

Figure 9: Outlines of snouts of rapidly burrowing lizards showing upper labial scales (A, C and D from side, B from above). (A, B) *Callisaurus draconoides*; (C) *Uma notata*; (D) *Meroles ctenodactylus*. (E) Shows commercial multi-diameter cutter analogous in action to the snout of burrowing *Callisaurus*. Figure reproduced from [7].

Locomotion using lateral undulations for desert lizards placed a premium on the avoidance of friction and most species appear to have their contact surfaces modified accordingly. In addition to a loss of limbs, reducing the skin friction appears to have forced most species to have their contact surfaces modified accordingly [41, 11]. In the *Uma notata* the scales

of its body are reduced to granules, giving a velvety effect. This lessens the friction in the sand as compared with the rough scaled forms potentially reducing the drag as the animal enters the medium [90].

Other adaptation of these sand swimmers include reduced ear openings, a sub-quadrangular cross–section of the body (more precisely, a flattened pentagon), and limbs with fringed digits and toes [10]. Most previous studies on these morphological adaptations have been descriptive and only few [10] have experimentally investigated the effect of these morphological adaptations on performance. A major constraint in investigating subsurface locomotion in sand is that the medium is opaque to visible light.

1.2.4 Techniques to study locomotion within opaque media

Due to the opaque nature of the complex substrate like soils, debris, and sand little is known about the behavior of animals that move within it. An effective means of observing animals in such substrates would allow to better define the niches of taxa coexisting in the apparent uniformity of sediment [34], as well as to measure the influence of environmental parameters such as temperature and substrate type on animal activity ([79] as an example), population density on the activity of individuals [58], and predators on prey burrowing behavior [51].

Most studies that describe the behavior of burrowing animals have relied on direct observation [90, 7]. A recent study by Dorgan et al. [31] utilized gelatin to visualize the motion of *N. virens* within muddy sediment (on the basis that the mechanical properties of the mediums were similar). Since gelatin is birefringent the authors were able to use polarized light to visualize the stress fields generated as the organism burrowed via crack propagation.

Radiography (x-ray) has been used to study the behavior of insects within media [59, 16]. Using radiographic x-rays to study larger size scale animals like lizards is a challenge as an increased amount of media is required for the animal to be able to perform its typical locomotor behavior. Reducing the size of the test container could lead to an alteration in the locomotion mode of the animal due to boundary effects. As an example, such an effect could have contributed to the disagreement in the mode of subsurface locomotion hypothesized

for sand-swimming lizards by field observations (see Fig. 5), and that reported in [10] where a small container with a reduced amount of material was placed in an nuclear magnetic resonance (NMR) system to test the animal.

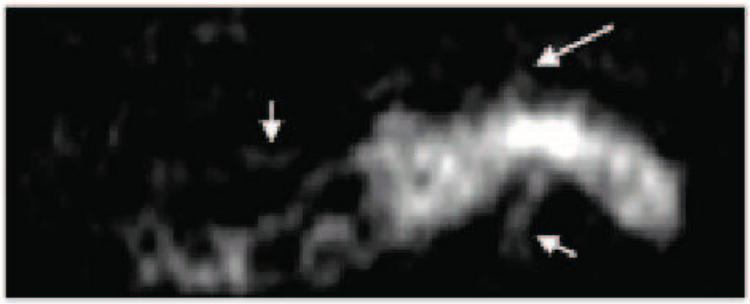

Figure 10: Nuclear Magnetic Resonance (NMR) image of the sandfish using its limbs during the burial process. The three visible limbs extended from the body are marked by arrows. Figure reproduced from [10].

Another technique commonly used to obtain real-time moving images is fluoroscopic imaging. A fluoroscope consists of an x-ray source and fluorescent screen between which the moving object of interest is placed. To obtain and record the images of this motion the screen is coupled to an x-ray image intensifier and video camera. After the x-rays from the source are emitted, they are attenuated by varying amounts due to the relative density differences between the animal and the medium, casting a shadow of the animal on the fluorescent screen. The images on the screen are produced as the unattenuated x rays interact with atoms in the screen through the photoelectric effect, giving their energy to the electrons. While much of the energy given to the electrons is dissipated as heat, a fraction of it is given off as visible light, producing the images which are captured by a camera [94].

1.3 Numerical simulation of bio-locomotion

The complexity in interaction with the environment in aquatic and aerial locomotion (swimming and flying) is well recognized [3]. Studying features like the power and energetics during these locomotion modes relies on analyzing the physics of the interaction using established theory like Navier - Stokes equations, and using visualization tools like Particle Image Velocimetry (PIV) to make observations and measurements of the associated flow fields. Compared with conceptual models, like the two dimensional waving plate theory by Lighthill for analyzing fish undulatory swimming [75], computational mechanical modeling of animal swimming and flying allows us to directly solve the Navier–Stokes equations that govern biological fluid dynamics [114].

By using numerical simulations to directly solve Navier–Stokes equations, one can visualize swimming and flying so as to provide detailed information of physical variables such as velocity and pressure at macro- and microscopic level, and hence give an overall understanding of the physical phenomena. An integrated computational framework involving morphological modeling, kinematic modeling, and computational fluid dynamics [77] provides us with an efficient method to deepen our understanding of biological mechanisms, and also serves as a powerful tool for designing man-made vehicles such as UAVs/UMVs.

Undulatory swimming in fluids has been investigated by developing computational models that couple the internal molecular motor mechanisms of organisms like nematodes and leeches with an external fluid. In these 3D simulations, the model organism (being self-propelled) follows a path determined by the forces acting upon it, as generated by its prescribed changing shape [23]. Recent neuro-mechanical simulations that combined numerical models of the spinal neural networks controlling locomotion with a mechanical model of the salamanders body in interaction with its environment, helped explain the ability of salamanders to switch between swimming and walking [62]. The study also suggested neural mechanisms for modulation of velocity, direction, and type of gait that are relevant for all tetrapods. The results of this simulation work were used to develop a robot (AmphiBot), that displayed the same locomotor behavior as the animal [24].

Numerical simulations of complex substrates (once validated against experiment), can

give us an understanding of the detailed physics of the granular medium, for example, force and flow fields from the grain perspective. The simulation is a flexible design tool with which parameters like grain-grain friction and animal kinematics can be easily varied to accurately predict performance. This would allow us to study the effect of locomotion parameters like body shape, friction, kinematics, etc. on performance (like cost of transport, power, force and velocity fields) during different locomotion modes like burial and maneuvering, which are difficult to vary/explore with an organism. Numerical models at various levels and complexities, can play a critical role in developing unified neuro-mechanical descriptions of locomotive behavior, and guide the modeling and understanding of other biological systems [92].

Advances in creating high performing flying and swimming devices [24, 66, 123] in aerial and aquatic domains, and wheeled/tracked vehicles on relatively structured terrestrial terrain have occurred mainly because the respective fields of aerodynamics, fluid dynamics, and terramechanics [12, 66] provide accurate models of locomotor-media interaction which are in turn used to design improved wings, fins, wheels, and legs. A major use of the numerical simulations is as a tool to design robots that move on and within complex flowing particulate environments (e.g. sand, soil, and leaf-litter) that can display both solid and fluid-like behavior in response to stress.

1.4 Bio-inspired limbless robots

Biological organisms have evolved to perform and survive in a world characterized by rapid changes, high uncertainty, indefinite richness, and limited availability of information. Concepts from biologically inspired robotics will eventually enable researchers to engineer machines for the real world that possess at least some of the desirable properties of biological organisms, such as adaptivity, robustness, versatility, and agility [96]. In addition, these robots can be designed to overcome the various anatomical and physiological limitations of the animal that inspired them to maximize performance.

There is a need for robots that can move within complex material like sand, rubble, and loose debris. For example such robots could help locate hazardous chemical leaks [61], function as self propelled inspection devices [84], and search for victims in disaster sites [86, 8, 83]. Limbless robots that use their bodies to move through material appear best suited to navigate these terrains as traditional wheeled [102, 112, 121, 4] and legged robots [74, 73, 105, 97, 56, 106, 67] are often impeded by the size or shape of their appendages which can result in entrapment or failure. Previous terrestrial limbless robots utilized serpentine locomotion to move on the surface of media. Of these, most were tested on rigid surfaces [53, 111, 27, 68, 24] with only a few having been developed for and tested in unstructured environments [19, 20, 33].

1.4.1 Advantages of limbless robot

Limbless undulatory locomotion provides a number of advantages over traditional wheeled [102, 112, 121, 4] or legged robots [74, 73, 105, 97, 56, 106, 67].

- Being limbless these robots are not impeded by the presence of appendages that could due to their size and shape get entrapped or fail. Being elongate with small cross–sections these robots an move through small holes and crevices and can even cross large gaps.

- Unlike limbed robots which are stable for only certain limb configurations, limbless terrestrial robots are inherently stable due to their low center of mass as their body

maintains contact with the substrate as it moves. The large area in contact with the ground also provides additional traction to the robot as it progresses forward. Limbed or wheeled robots have smaller contact areas making slippage more likely to occur.

- Since limbless robots have many repeated structures if one fails the robot can still continue to locomote, albeit at a higher cost of transport. Most limbed robots cannot move once any of their appendages have been compromised.

- The energetics of limbless and limbed locomotion is comparable. The major energetic cost in limbed motion comes from the oscillations of the center of mass and the acceleration or deceleration of limbs. For limbless locomotion these factors do not contribute to the energetic cost, instead the major energy loss is due to the frictional losses into the ground and lateral accelerations of the body that do not contribute to forward motion.

1.4.2 Limbless robots: background

The design of limbless undulatory robots that utilize serpentine locomotion to move on the surface of media have greatly benefited from the anatomical and locomotor studies of snakes [64, 89]. Most snake robots are made up of many simple repeated structures connected end to end to give it its elongated form. These repeated structures correspond to the vertebrae of the snake which in the real animal are made up of $100 - 400$ parts each allowing motion in the lateral and vertical directions, acting as compliant universal joints. Each vertebra allows rotation of $10 - 20°$. in the horizontal plane, and $2 - 3°$ in the vertical plane. There are four major snake locomotion gaits: (1) lateral undulatory, (2) concertina, (3) side-winding, and (4) rectilinear progression [64]. The majority of snake-inspired robot designs use either lateral undulation or rectilinear progression.

Snake-inspired robots were introduced in the 1970s by Shigeo Hirose [52] and since then most designs of limbless robots have followed the common theme of mimicking snake locomotion, but have differed greatly in physical configuration and purpose [57]. A survey study on snake inspired robot classified these designs as: (1) robots with passive wheels, (2) robots with active wheels, (3) robots with active treads, (4) robots based on undulation

using vertical waves and (5) robots based on undulation using linear expansion [57].

1.4.2.1 Limbless robots with passive wheels

The kinematics of these limbless robots may be described by a series of S-shaped, sinusoidal-like curves that the body forms as it undulates while passive wheels attached to each segment resist lateral movement of the robots segments [52]. Some snake robots to use this mechanism include Hirose's active cord mechanism [52], AmphiBot [24], and Gavin Millers robot family [88].

Active Cord Mechanism (ACM) design

The original ACM design (see Fig. 11 A) consisted of 20 segments and was capable of only 2D motion [52]. The main idea of the design was to mimic the anisotropy in the friction coefficients between the lateral and tangential directions in the snake induced by its scale structure that allowed it to progress forward. To achieve this small wheels on casters were placed at the bottom of each segment, which resulted in a very low friction coefficient in the forward direction and a high coefficient in the lateral direction. The links were connected using powered joints that allow rotation relative to one another, and locomotion was accomplished by propagating a traveling wave along the body of the robot. The 2 m long, 2 kg robot was only tested on smooth flat surfaces.

The most advanced of Hirose's designs introduced in 2005, the ACM-R5 (see Fig. 11 B), was an amphibious design. The joint between each segment of the robot consisted of a universal joint and bellows. To generate propulsive force by undulation both on ground and in water, the robot included paddles and passive wheels around the body of each segment (for the appropriate lateral resistance). The robot measured 175 cm in length and weighed 7.5 kg [52, 18]. The robot performed reasonably on flat surfaces and in the water,but remained mostly as a demonstration platform.

AmphiBot design

The AmphiBot design was aimed at building an amphibious snake-like robot that could both

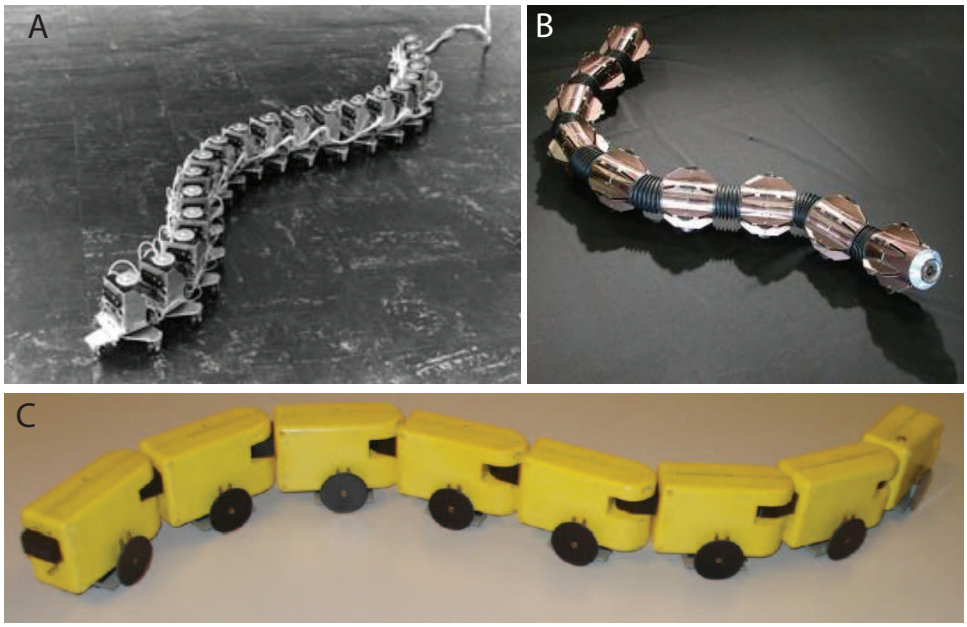

Figure 11: Photographs of limbless robots with passive wheels: (A) ACM I and (B) ACM-R5 designed by Hirose and (C) AmphiBot II designed by Ijspeert. (B) and (C) were designed to move both on land and in water.

crawl and swim for outdoor robotics tasks, taking inspiration from snakes and elongate fish such as lampreys (see Fig. 11). The robot design included seven actuated segments which are designed to have distributed actuation, power and control; therefore, each element carried its own dc motor, battery and micro-controller which allowed for an extra level of redundancy. Each segment was made to be slightly buoyant so that the robot would passively float at the surface of the water when inactive. The robot was designed to be tether-less, and was tested using a set of wheels when on surface terrains. The robot was used to demonstrate the use of central pattern generators (CPGs) as a powerful method for online trajectory generation for crawling and swimming in a real robot [24, 62].

1.4.2.2 Limbless robot with active wheels

Another group of limbless robots utilized active-driven wheels to provide propulsion for the robot (see Fig. 12). These robot designs still exhibited snakelike motion due to the multi-segment configuration. The main advantages of using powered wheels is the ability to simulate snake-like motion without a large number of segments. Powered wheels also generally are more able to deal with non-smooth terrain types. Although the introduction

of powered wheels introduced additional flexibility it also added complexity to the control in terms of co-ordination with the other actuated joints. Some robots that utilized this design for locomotion include Koryu-II [54] and ACM-R4 [122].

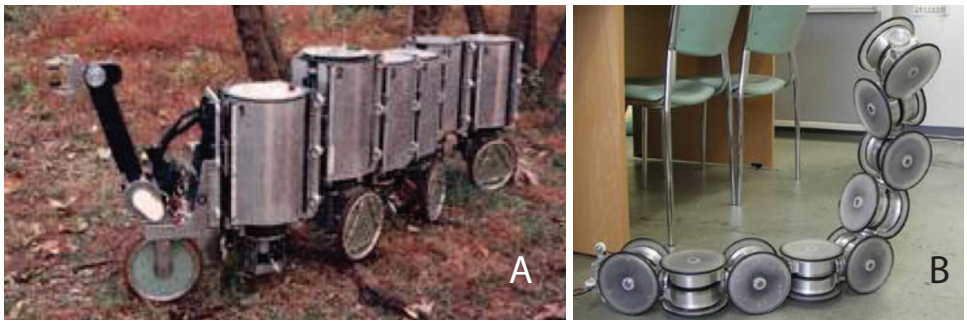

Figure 12: Photographs of limbless robots with active wheels (A) Koryu-II and (B) ACM-R4, both designed by Hirose [54, 122].

1.4.2.3 Limbless robots with active treads

Robots that are included in this classification were built specifically to navigate through small, tight openings within the debris and locate and assess the condition of possible survivors of disasters like earthquakes etc. The propulsion of the robot was achieved by an innovative means: using tank treads on the four sides of every segment (example the OmniTread robot (see Fig. 13)). The tank tread design maximized the ratio of surface area that was active in propulsion to the surface area that was not. To insure this the tank treads covered as much of the sides as possible such that any environmental feature that contacted the robot at a location not covered by treads would not impede the motion. Treads on each side also made the design indifferent to falling over. These robots utilized gait powered treads or crawlers to increase stability and traverse rough terrain. Other robots using this mechanism included the OmniTread family of robots [45], Koryu-I [52], and the JL-I [118].

1.4.2.4 Limbless robots using vertical undulations

The robot's locomotor mode may be described as a creeping motion where a segment of the robot advances an adjacent segment forward while anchoring itself to the terrain. In turn, the advanced segment repeats the process for a segment adjacent to it until the entire robot has advanced forward a distance equal to the displacement of the first segment in the

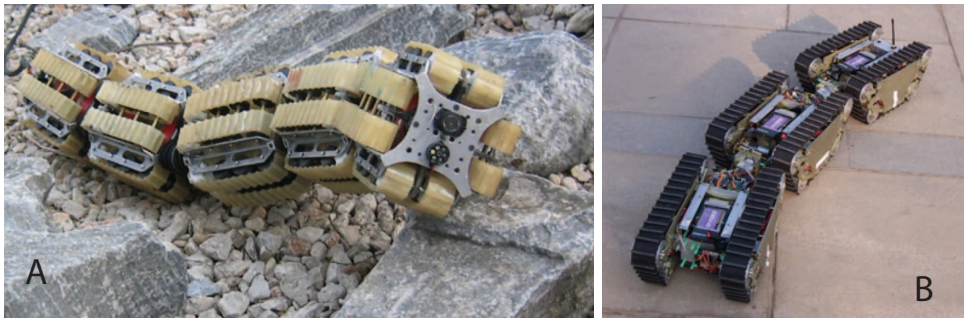

Figure 13: Photographs of limbless robots with active treads: (A) OmniTread OT-8 and (B) JL-I were designed by Hirose to move on rough terrain for search and rescue applications.

sequence. Some examples include Kotays inchworm robot (inspired by the peristaltic contraction of inchworms) [70], Dowlings snake robot [33], and CMUs modular snake robots [20] (see Fig. 14).

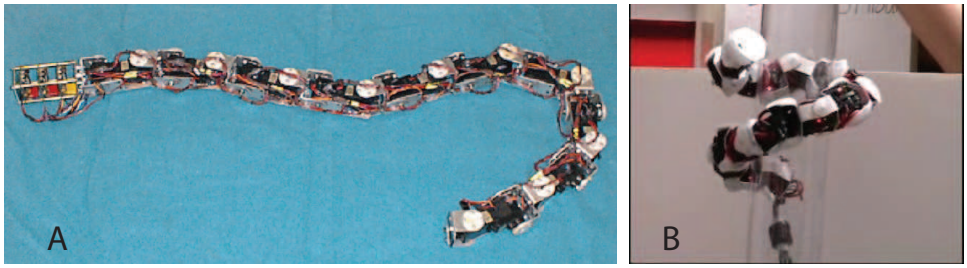

Figure 14: Photographs of limbless robots that move based on undulations using vertical waves: (A) Dowling's snake robot and (B) CMU modular robot.

1.4.2.5 Limbless robots based on undulation using linear expansion

Forward motion of the robot may also be achieved by linear expansion and contraction of the robot body to form a gait similar to those used by larger sized snakes like anacondas. During this rectilinear motion lateral bending of the body and lateral resistances do not contribute to the motion instead relative contractions and expansions along the length of the robot (driven by anisotropic friction) allow the robot to propel itself forward. Examples include Slim Slime robot [93], and Yeos planar inchworm robot [17] (see Fig. 15).

1.4.3 Effect of robot shape on performance

Major advances in creating high performance flying and swimming devices have been made by studying the interaction between airfoils like wings, blade, sails, and keels, and the

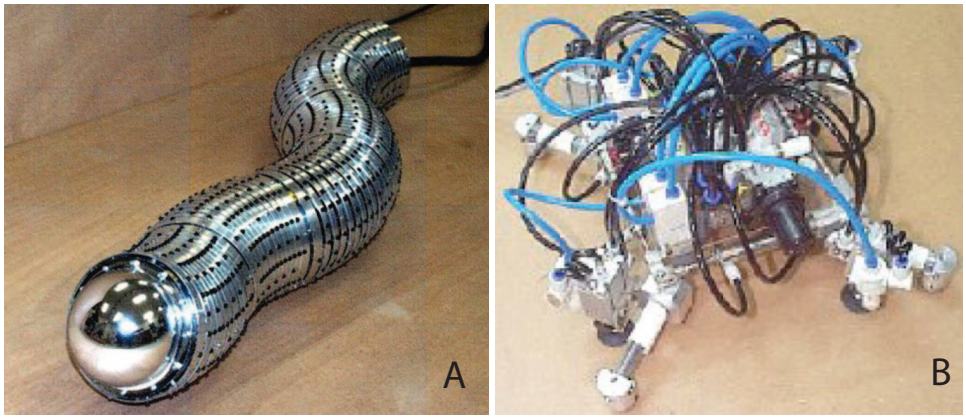

Figure 15: Photographs of limbless robots which move based on undulations using linear expansion: (A) Slim slime robot and (B) Yeo's planar inchworm.

surrounding fluid (air or water) [66, 28]. Specifically, an understanding of the effects of shape and attack angle on lift have helped design devices that can modulate their vertical position in water and air while minimizing drag forces.

In the biological world swimming and flying organisms control flow to manipulate lift and drag to enhance performance (e.g. increase speed and stability). [38, 37]. Control can be passively realized through the anatomy of the animal (morphology and structural features dictating flow), examples include protuberances on whale flippers and riblets on shark skin. The control can also be active; fish alter tail camber, area, and angle of attack during the tail beat to vary performance [38], while insects and birds generate lift during forward flight and hovering [104].

Understanding how forces are generated due to the shape of the robot as it moves within complex substrates can help provide principles for the creation of robots that can begin to follow arbitrary trajectories within complex substrates like sand, and also lend support to hypotheses that the morphological adaptation of desert dwelling organisms aid in their subsurface locomotion.

1.4.4 Applications of sand-swimming limbless robots

Inspired by the technology used to build serpentine robots that can move on the surface of media, a limbless robot that can move within complex material like sand, rubble, and loose debris in the same way as a desert dwelling lizard does could find application in a number

of areas.

- The undulatory locomotion ability coupled with a reduced cross-sectional area would allow such a robot to enter dangerous areas like those following earthquakes, explosions, cave-ins [86, 8, 83] to search for and possibly rescue survivors. The speed and effectiveness of such operation is generally stymied by the unstable nature of the material and the narrow access routes available into the bulk, both problems that a limbless robot could contend with.

- The lunar and martian terrains are made up of soft sand and rocks distributed over dunes and craters that make navigating them with limbed robots a challenge. The stable configuration and large contact area of limbless robots make it particularly advantageous for use in these environments as even if contact between the robot and the medium at some points are lost self-support between secure points enables continued operation [33].

- Subterfuge and reconnaissance offer some novel applications of limbless robots. An immediate and critical application is the detection of improvised explosive devices (IED) placed within desert sand.

- Medical applications as an endoscopic access to the digestive tract for early detection of diseases. There is a need for devices which are able to navigate in tortuous, slippery and difficult to access cavities of the human body while causing minimal discomfort and pain [85]

1.5 Summary

In this dissertation I utilized x-ray imaging techniques to study the ability of a desert dwelling lizard to locomote within sand. I investigated the effect of varying media preparation and properties (like particle size) on the locomotor ability of the animal. I used a numerical simulation to evaluate the effect of varying animals kinematics on performance and identified the kinematic conditions that maximize performance. I then developed a robot with similar locomotor ability to the animal to complement the simulation approach and validated its predictions in a real world environment. I also tested the effect of shape (inspired by the animal morphology) on the performance of the bio-inspired robot. This complementary modeling approach allowed me to develop and test mechanical hypothesis of interaction between the locomotor and its surroundings.

The study of how organisms interact with their environments can help answer major questions in locomotion biology such as, what kind of morphological structures and kinematics of actuation are needed to produce locomotion in a particular substrate. Guided by these fundamental principles, we can create mechanical models to probe biological hypotheses beyond the limitations posed by the organism and also help design bio-inspired robotic devices that can maneuver effectively within complex environments.

CHAPTER II

BIOLOGICAL SAND-SWIMMING EXPERIMENTS

Animal burrowing and movement within granular media is relevant to desert organisms like scorpions, snakes, and lizards that move within sand to escape heat and predators and hunt for prey [6, 87]. Desert sand [which covers 6 to 10% of land surface [35]] is an example of a granular material, a collection of dissipative particles that interact through contact forces and in bulk can display solid and fluid-like features [63] when disturbed. A key parameter that controls the response of granular media to intrusion is the volume fraction ϕ, the ratio of material volume to total occupied volume. In dry granular media in natural environments, ϕ depends on the history of the sand (for example, perturbations by wind or animal burying and digging), and can vary between 0.57 and 0.64 [29]. The response of granular media to intrusion depends on ϕ: closely packed material at high ϕ must expand to flow, whereas loosely packed material at low ϕ consolidates [91]. The effects of ϕ on drag are largely unexplored, although we have recently found that vertical penetration resistance nearly doubles as ϕ increases by just 0.08 [74].

To investigate how rheological features of the material influence the locomotor mode and performance of an organism moving within sand, we used high-speed x-ray imaging to study a small (10 cm) desert-dwelling lizard, the sandfish, that inhabits the Saharan desert of Africa and moves within granular media of different ϕ*. We also tested the ability of the sandfish to swim within larger sized particles (3 mm) to reduce the computational time required to simulate the medium for the numerical sandfish simulation (Chapter III)†.

*Results of this work were published in the journal, *Science*. Maladen R.D, Ding Y, Li C, and Goldman D.I, *Undulatory Swimming in Sand: Subsurface Locomotion of the Sandfish Lizard* [82].

†This work is part of a paper in review. Maladen R.D, Ding Y, Umbanhowar P.B, Kamor A, and Goldman D.I, *Mechanical models of sandfish locomotion reveal principles of high performance subsurface sand-swimming*, Journal of the Royal Society Interface

2.1 Experimental materials and methods

2.1.1 Granular media preparation using a fluidized bed

We tested the animal in a 10 cm deep layer of granular material (0.27 ± 0.04 mm diameter spherical glass particles similar in size to desert sand [9], density $2.4\,\mathrm{g/cm^3}$) held in a fluidized bed ($21.5 \times 21.5 \times 18\,\mathrm{cm^3}$). We used the bed to prepare the granular material into loose ($\phi = 0.58$) and close ($\phi = 0.62$) volume fractions. The fluidized bed is a device which has a horizontal porous plastic (Porex) flow distributor (thickness 0.64 cm, average pore size $90\,\mu$m) on which the glass particles rest. By blowing air upward through the distributor with LPM leaf blowers (Toro) (their power is controlled using a variac), the entire bulk of granular media is fluidized. Below a critical flow rate (the onset of fluidization), grains are stationary; above it, the material is fluidized and grains flow. To generate loosely packed states (LP, $\phi = 0.58$) the flow is increased to above the fluidization onset and then slowly decreased to zero. To generate closely packed states the air flow is repeatedly pulsed. Increasing the number of pulses increases ϕ; typically we deliver over 200 pulses to achieve the closely packed state (CP, $\phi = 0.62$).

2.1.2 Visualization through granular media using x-ray imaging

To obtain dorso-ventral plane (x-y) images of the sandfish swimming subsurface the fluidized device was placed between the cathode (image intensifier) and anode (x-ray source) of a c-arm x-ray unit oriented vertically as shown in Figs. 16 and 18. The x-ray unit used was a Radiological Imaging Systems, OEC 9000 system. For the data presented in this work the energy setting of our system was varied in the range of $85 - 100$ kV at 20 mA. A high speed digital camera (Photron, set to 250 fps) was placed below the image intensifier to stream images of the animal swimming to a computer located outside the x-ray enclosure and to be saved as a video file.

2.1.3 Animals subjects

Sandfish lizards (*Scincus scincus*) were obtained from a commercial supplier (LLL Reptile, CA, USA) and were housed in a dedicated animal care facility, and kept in a 12 hour

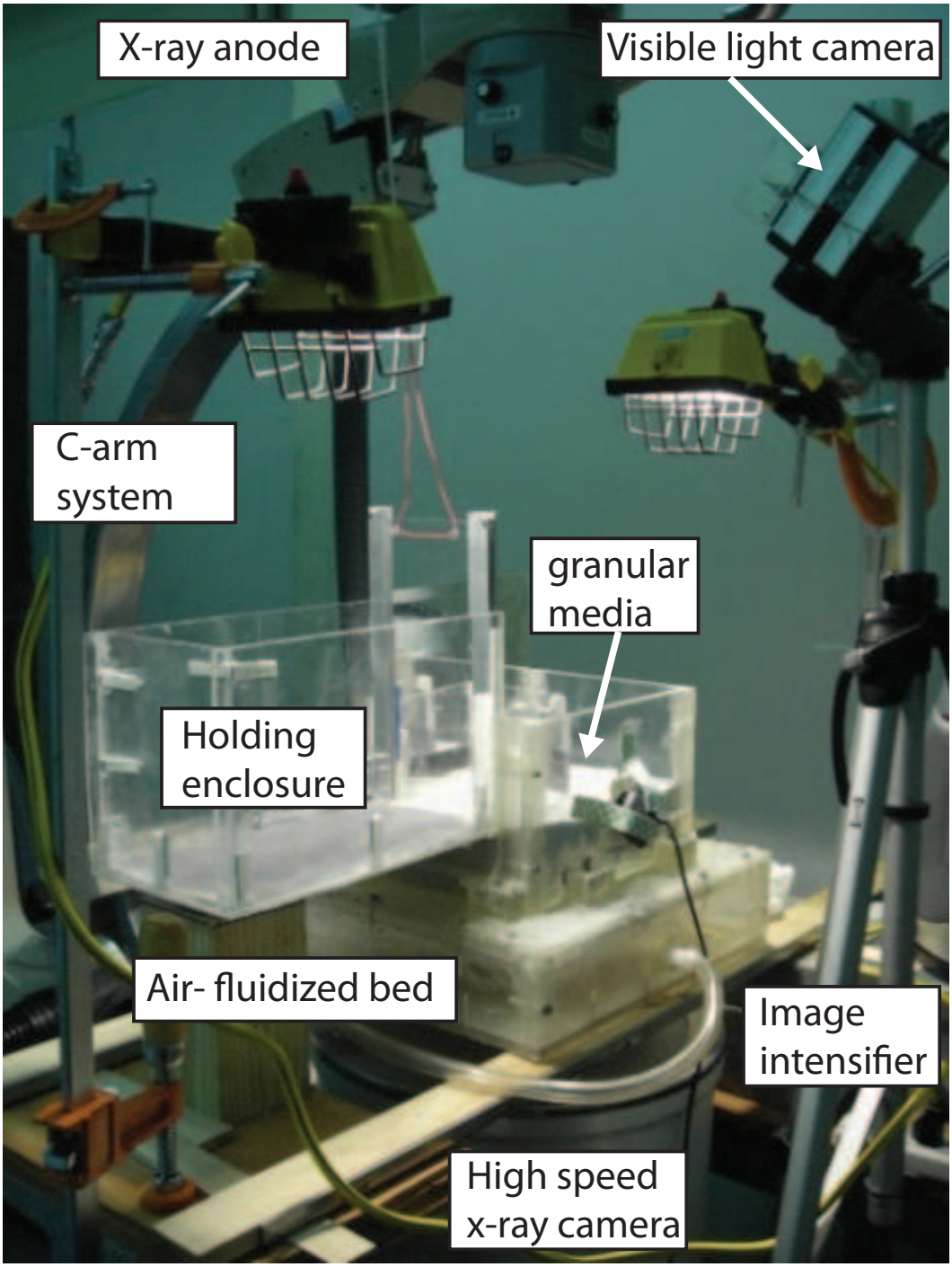

Figure 16: Experimental setup: a fluidized bed was placed between the x-ray source and image intensifier of a c-arm x-ray system. The initial state of the granular media (0.3 mm or 3 mm spherical glass particles) used to fill the fluidized bed was set using air pulses. Air flow was turned off before the experiment. Once the material was prepared the sandfish was released from the holding enclosure by raising a mechanical gate. Simultaneous x-ray and visible light video (250 fps) were recorded as the animal moved on and then into the granular medium.

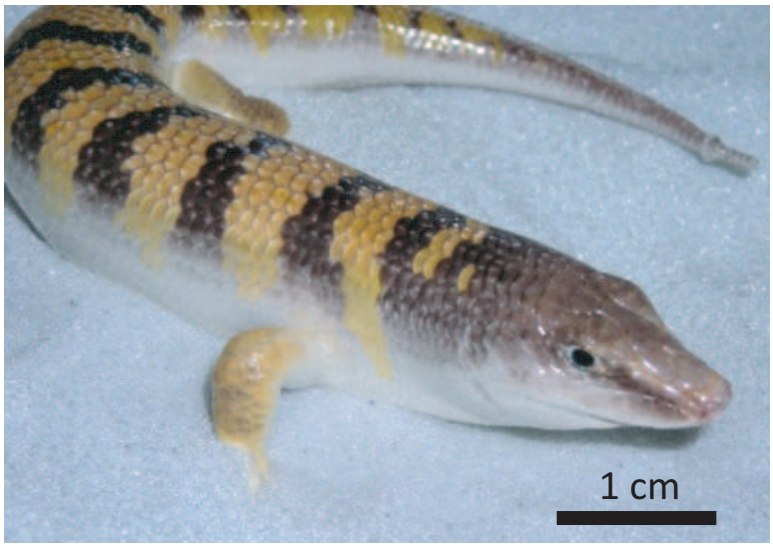

Figure 17: The sandfish lizard on 0.3 mm glass particles.

day/night light cycle. No animal was tested for more than 10 runs in a single day, and was rested for at least 4 days before being tested again. The duration of exposure to x-rays was ≈ 10 s for each run. The average snout vent length (SVL), which is denoted as body-length L was 8.3 ± 3.3 cm, about 75% of the snout-tip to tail-tip length. The average mass was 16.2 ± 4 g. Experiments were conducted in an environment with temperature controlled to between $30 - 35°$C.

2.1.4 Experimental protocol

The initial state of the granular material in the fluidized bed was set and the sandfish placed in a holding enclosure that opened onto the fluidized bed. After the x-ray beam was turned on, the gate of the enclosure was rapidly raised to release the animal so that it could run onto the surface of the granular media. We used a 'virtual wall' placed 15 cm from the enclosure gate above the media to encourage the animal to dive into the same location in the bed. A virtual wall is thin blacked out piece of plexi-glass that extends only to the surface of the media. The animal consistently took a few steps before diving into the material. The sandfish appeared dark in the above ground x-ray images since the radiation must travel through the sand and the animal, while below ground it appeared lighter since sand had been displaced horizontally by the body of the organism. Once the animal stopped moving

the x-rays were stopped and the x-ray and visible light imaging cameras post-triggered to obtain images of the run. Runs for which the sandfish did not swim straight, swam near the wall, or for less than a single undulation were not saved.

2.1.5 Video Analysis

For the different media preparations and particle sizes that were tested the x-ray and visible light videos were synchronized to determine when the sandfish was moving subsurface. The above surface analysis was done using the visible light video. The temporal frequency and forward velocity of the animal were measured from the synchronized portion of the x-ray video. Displacement was calibrated using a grid. X-ray visible natural body markers (the snout and lungs) as well as the silhouette of the animal were used to estimate the mid-line of the animal. The mid-line was tracked using a custom written MATLAB code. Only runs for which the sandfish completed at least 1.5 cycles of undulation subsurface were considered for analysis.

2.2 Results

2.2.1 Burial of the sandfish into granular media

Once the gate to the enclosure with the sandfish was raised the animal ran onto the material using its limbs with a diagonal gait, typical of most lizard [36] but with little body undulation. Visible light video revealed that as the sandfish began to enter the medium it inclined its head at a downward angle to the horizontal (in xz plane) and relative to its long axis (in the xy plane), and used its limbs in synchrony with high amplitude undulations (less than one period) to bury into the material (Fig. 19). The sandfish took 672 ± 239 ms to complete its entire burial process, independent of medium preparation (Students t test, $p > 0.05$). As the animal moved subsurface there was nearly no perturbation of the material at the surface.

Analysis of the visible light and x-ray imaging of the transition from above ground locomotion to subsurface sand-swimming revealed distinct differences in the mode of locomotion. Above surface the animal used its limbs to propel itself forward with little or no body undulations while subsurface the animal progressed forward using body undulations

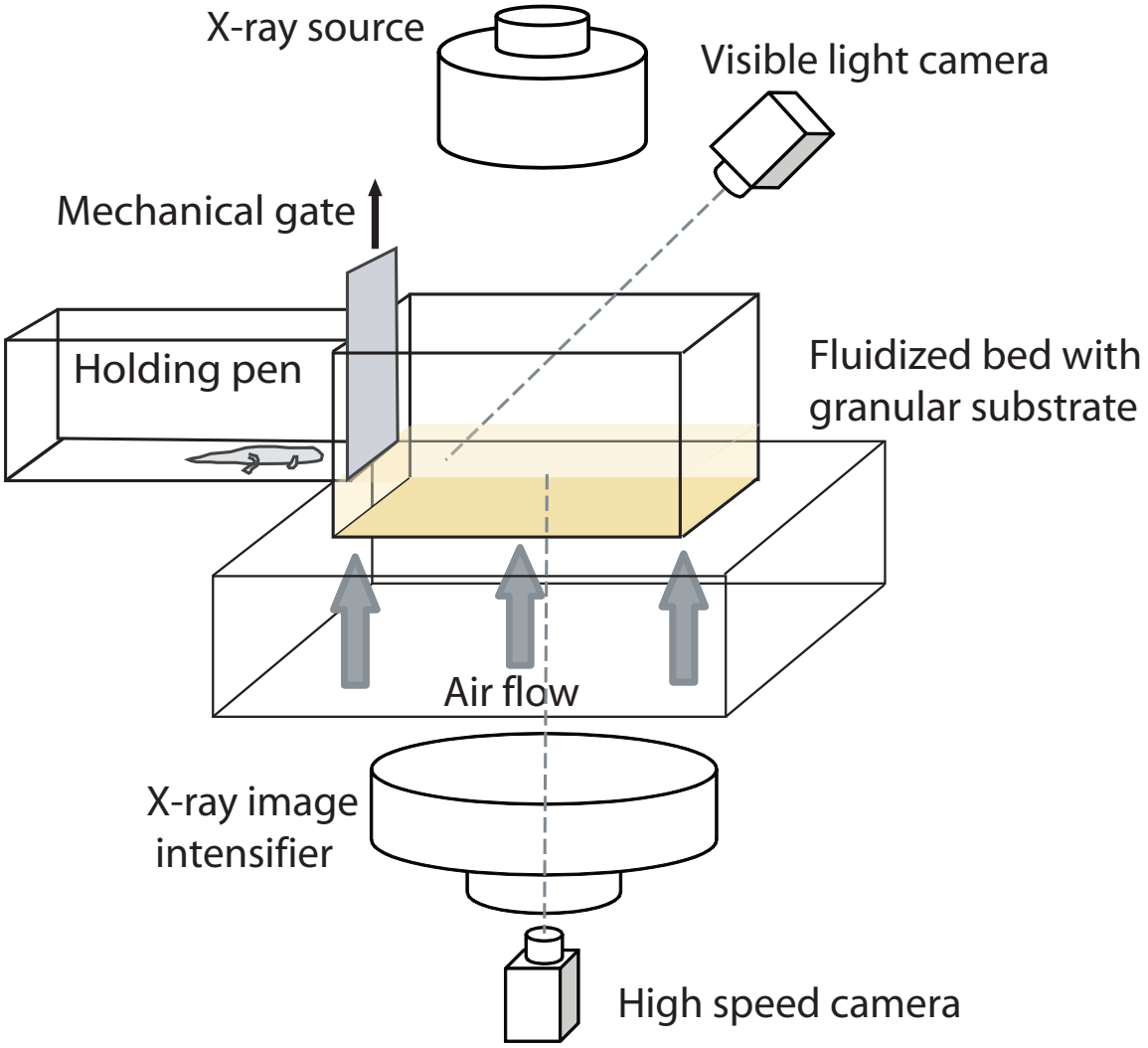

Figure 18: Schematic of the experimental setup used in the biological experiment. The fluidized bed was placed between the source and image intensifier of a c-arm x-ray system. The initial state of the granular media (0.3 mm or 3 mm spherical glass particles) used to fill the fluidized bed was set using air pulses. Air flow was turned off before the experiment. Once the material was prepared the sandfish was released from the holding enclosure by raising the mechanical gate. Simultaneous x-ray and visible light video (250 fps) were recorded as the animal moves on and then below the surface. Drawings are not to scale.

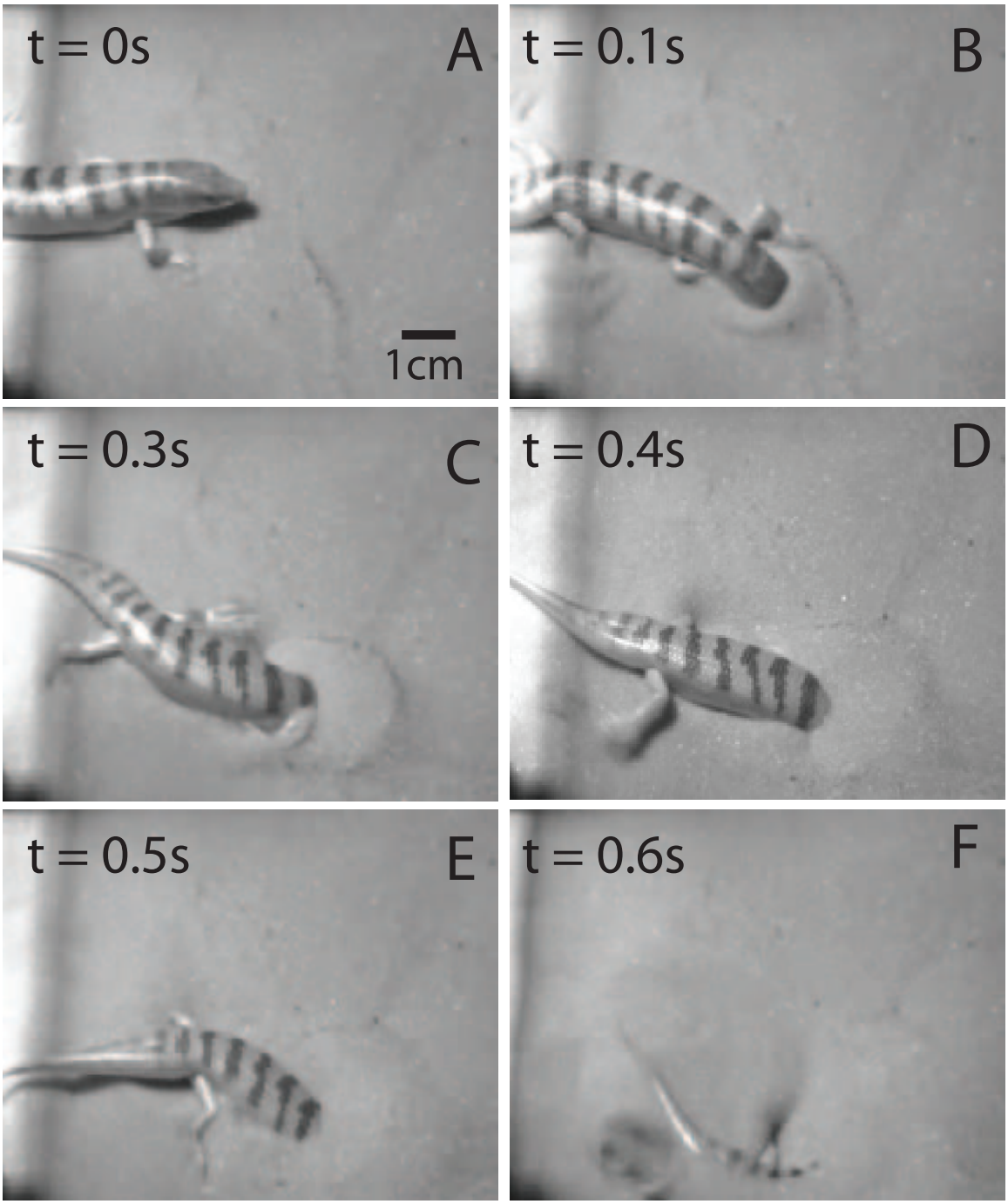

Figure 19: (A-F) Visible light images of the sandfish as it used high amplitude body undulations synchronized with its limbs to bury into the medium. The glass particle size was 0.3 mm.

without limb use (discussed in detail in the Section 2.3.3). These transitions involve moving from the sand-air interface (uniform pressure and free movement of particles) into sand bulk (pressure gradient and constrained movement of particles), which are likely to present the animal with biomechanical challenges.

We found that the animal did not stop using its limbs all at once, instead it followed a stereotypical pattern of limb dis-use along with high amplitude undulations, which were consistent for both media preparations (see Fig. 20). Within 70% of the total time required for burial (time taken to entirely disappear subsurface), the sandfish stopped using all its limbs.

We hypothesize that during the initial burial the animal enters the media with high amplitude undulations that results in a torque imbalance which causes the sandfish to experience a yawing motion (the animal orientation changes). The animal continues to use its limbs to counter this yaw and provide both stability and thrust. Once the net torque the body generates reduces the sandfish uses only body undulations to propel itself forward (details in next section). The testing of this hypothesis and further analysis are not a part of this dissertation.

2.2.2 Subsurface locomotion of the sandfish

Once subsurface, the dorso-ventral x-ray video imaging revealed that the animal no longer used limbs for propulsion. Instead the animal placed its limbs against its sides and executed an undulatory motion with large amplitude axial oscillation, using its body to propel itself at speeds up to ~ 2 body-length/s. This observation agreed with the hypothesis of how lizards like the sandfish swim within sand [7].

To characterize the undulations of the sandfish (Fig. 22 as it moved subsurface we fit the tracked mid-line of the animal with a traveling wave sinusoid that propagated along the body from head to tail.

$$y = A \sin \frac{2\pi}{\lambda}(x + v_w t) \tag{1}$$

with y the displacement from the mid-line of a straight animal, A the amplitude, λ the

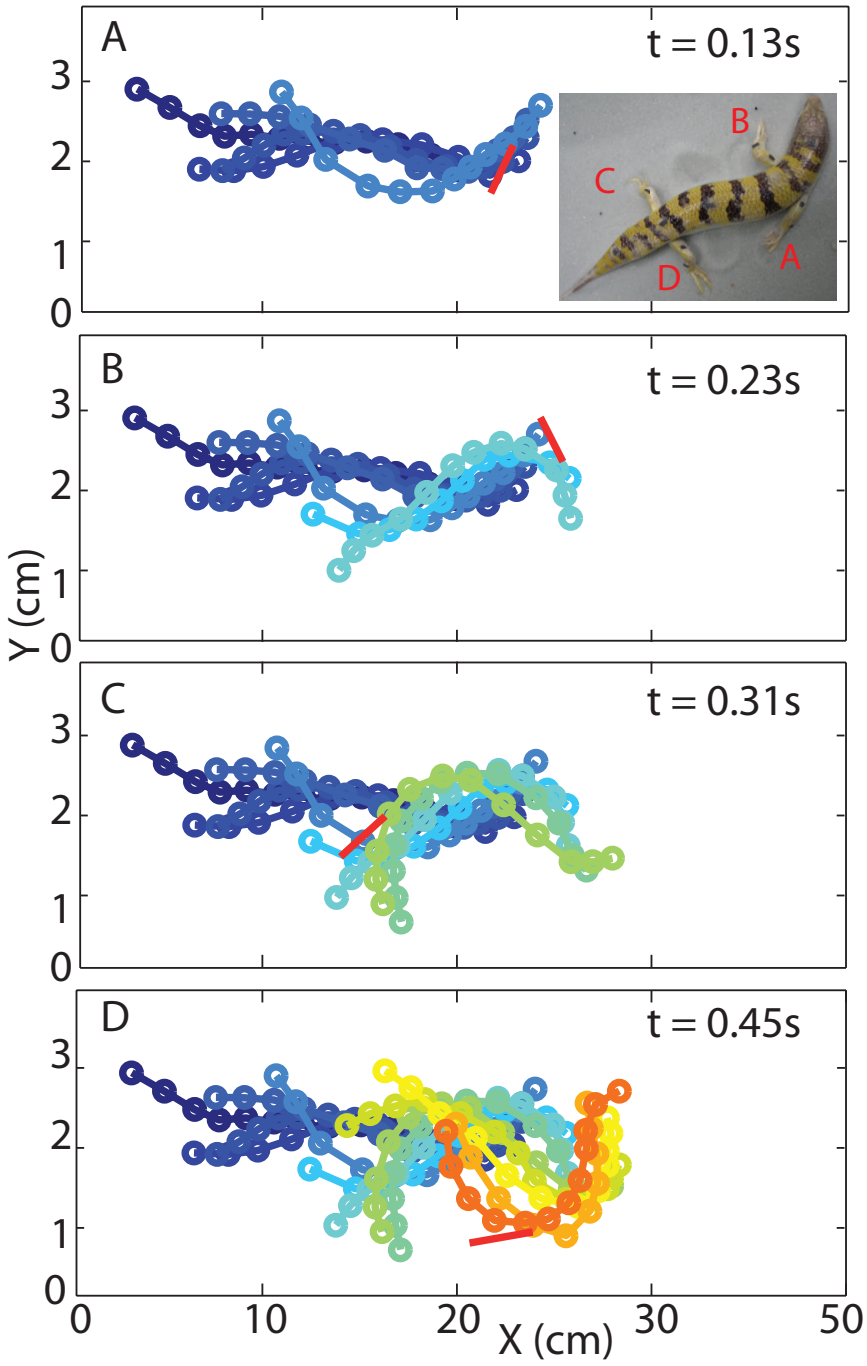

Figure 20: Representative tracked mid-line kinematics and limb use of the sandfish as it buried into the granular medium. (A-D) The mid-line kinematics of the sandfish until the time instant when the sandfish stopped using each individual limb, respectively. The inset in (A) shows an image of the sandfish its limbs marked in the order they were ceased to be used (labels correspond to the subplots). In each subplot the limb is indicated by a red line. The total time taken to bury into 0.3 mm glass particles was 0.58 s. The medium was prepared into a closely packed state.

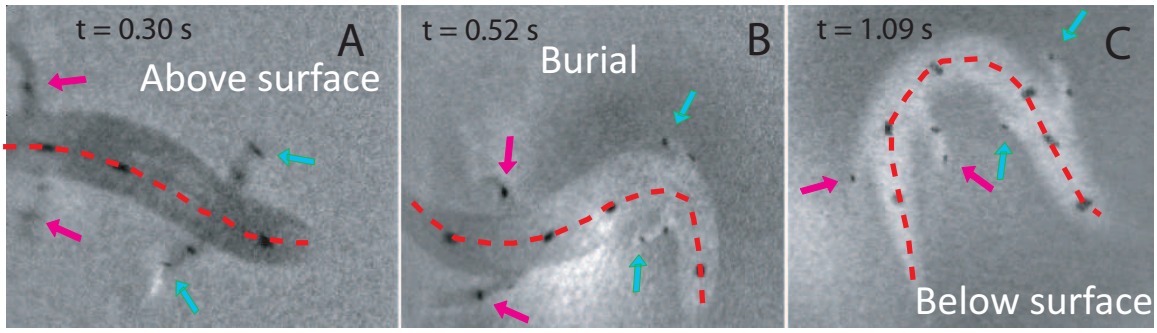

Figure 21: Representative x-ray images of the sandfish as it (A) moved with a diagonal gait on the surface, (B) as it buried into the media with high amplitude oscillations and synchronous limb use, and (C) as it swam subsurface with its limbs at its sides. The green and magenta arrows indicate the location of the opaque markers on the fore and hind limbs of the animal respectively. The red dashed curve corresponds to the mid-line of the animal. The glass particle size was 0.3 mm.

wavelength, f the wave frequency, $v_w = f\lambda$ the wave speed, t the time, and x the distance along a line joining the end points of the animal and parallel to the direction of motion. The x and y coordinates were set in the laboratory frame.

For all runs the digitized undulation profile of the animal were fit with a single period sinusoidal traveling wave at a fixed phase (Fig. 23). For runs with greater than 2.5 undulations subsurface the profile was fit for multiple phases to evaluate the variation in traveling wave parameters within a run. For all runs the fits had an $R^2 > 0.9$.

The large-amplitude undulations of the sandfish over its entire body were unlike the kinematics of other undulatory swimming organisms on the sandfish-sized scale [such as eels [14]], which tend to increase in amplitude posteriorly. The undulations of the sandfish do resemble those of eels moving on land [14] as well as small (< 1 mm) swimmers (e.g. spermatozoa and nematodes) in fluids at low Reynolds (Re) number, in which material inertia plays no role [48, 69]. We speculate that the kinematics are similar because the flow fields generated by the organism in granular media dissipate rapidly due to multiple dissipative particle-particle collisions, making the granular regime non-inertial and thus similar to low Re number flows.

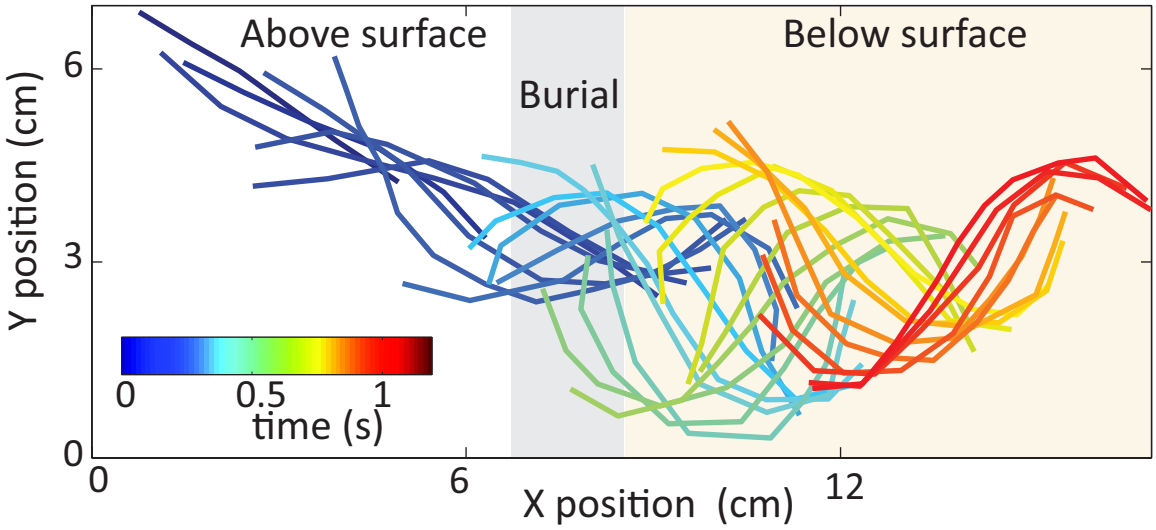

Figure 22: The lines represent the tracked mid-line of the sandfish as it ran on the surface using a diagonal gait with little back bending, buried with significant back bending, and then swam within the media with large amplitude back bending. The color bar represents time. The particle size was 0.3 mm.

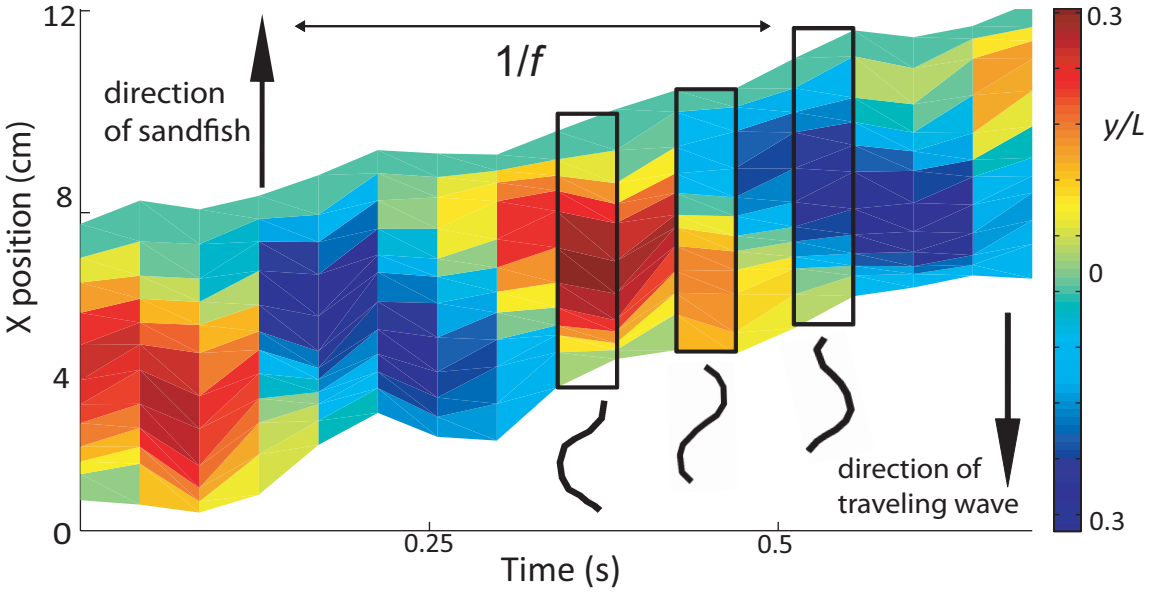

Figure 23: Traveling wave moving down the body of the sandfish opposite to the direction of the sandfish forward motion (sampled every 0.04 s). For each time instant, the instantaneous lateral displacement of a tracked section of the sandfish is represented in color. The black stick figures show the tracked mid-line of the sandfish.

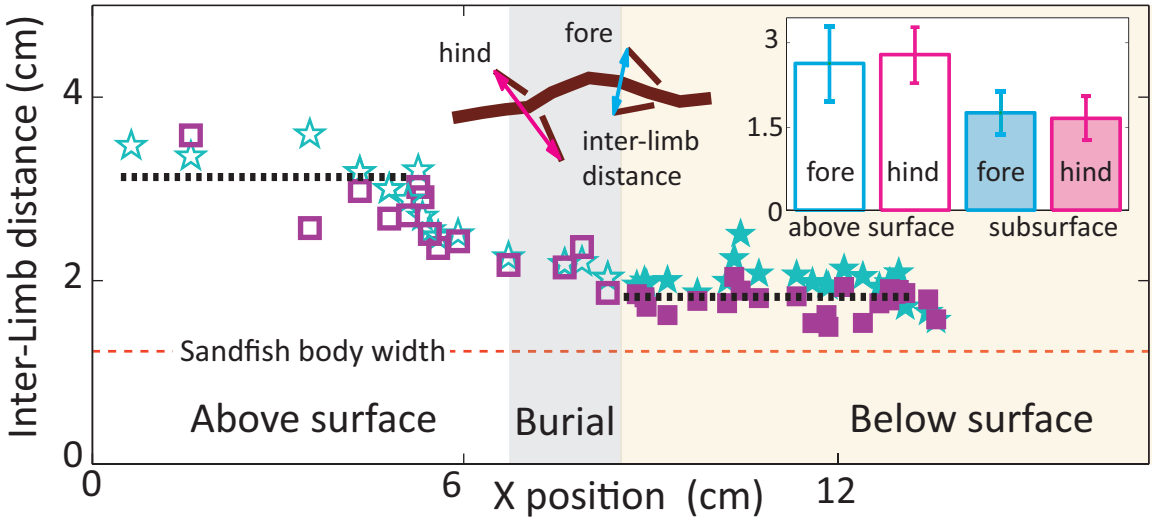

Figure 24: Sandfish limb use as it moved on, buried into, and swam within granular media. Above surface (open symbols) and subsurface (filled symbols) inter-limb distance of the fore (cyan star) and hind (magenta square) limbs plotted vs. the x coordinate of the center of mass. The dashed lines represent the average inter-limb distance (N = 10). Inset: bar graph shows the inter-limb distance (mean ± SD) for the fore and hind limbs both above and below the surface. The glass particle size was 0.3 mm.

2.2.3 Sandfish limb use during subsurface locomotion

We collected representative runs with opaque markers bonded to the body mid-line and limbs of the sandfish (see Fig. 21). The total mass of the markers was 0.04 g, much less than the 16 g animals. The distance between pairs of limbs (fore and hind) allowed us to determine the nature of limb use subsurface and contrast it with the diagonal gait used in surface locomotion (see Fig. 24). As the animal ran across the surface, this inter-limb distance oscillated around 2.75 ± 0.59 cm indicative of the sprawl of the limbs during the diagonal gait [3, 6]. As it began to bury, the inter-limb distance decreased significantly (Student's t-test, $p < 0.01$) until it became a constant (1.72 ± 0.53 cm) close to body width (1.23 ± 0.51 cm) as limbs were placed close to the side of the body. This result shows conclusively that the animal did not use its limbs to propel itself forward as it moved subsurface.

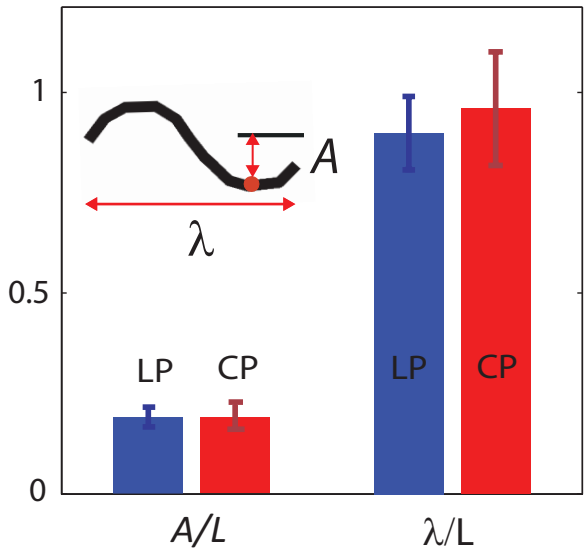

Figure 25: Spatial characteristics of the sandfish kinematics within loosely and closely packed 0.3 mm granular media. Representative points along the tracked mid-line (inset) were fit to a sinusoid with amplitude A and wavelength λ for loosely (LP, blue) and closely (CP, red) packed media (main figure). The values reported are normalized to body-length without the tail (SVL).

2.2.4 Effect of media preparation on sandfish kinematics

The parameters of the posteriorly traveling single period sinusoidal wave (Eqn. 1) were used to evaluate the effect of media preparation (packing) on the spatial and temporal characteristics of the sandfish kinematics. For the 0.3 mm glass particles during a swim, there was no change in either A ($p = 0.12$) or λ ($p = 0.66$), and neither A nor λ varied significantly for the different ϕ ($p > 0.05$ comparing each treatment using a repeated measures one way ANOVA), see Fig. 25.

The temporal characteristics of the traveling wave revealed that for both media preparations the sandfish increased its forward swimming speed by increasing its oscillation frequency f (see Fig. 26) (Student's t-test, $p < 0.01$). Also, the slope of the v_x vs. f relationship was independent of media preparation (Student's t-test, p$>$ 0.05) i.e. for a given frequency of oscillation the sandfish swam equally fast in loosely and closely packed media. Interestingly, the range of f (and v_x) that the animal accessed was greater in closely packed than in loosely packed material.

We found however that v_x was not simply the product of f and λ, but instead the slope

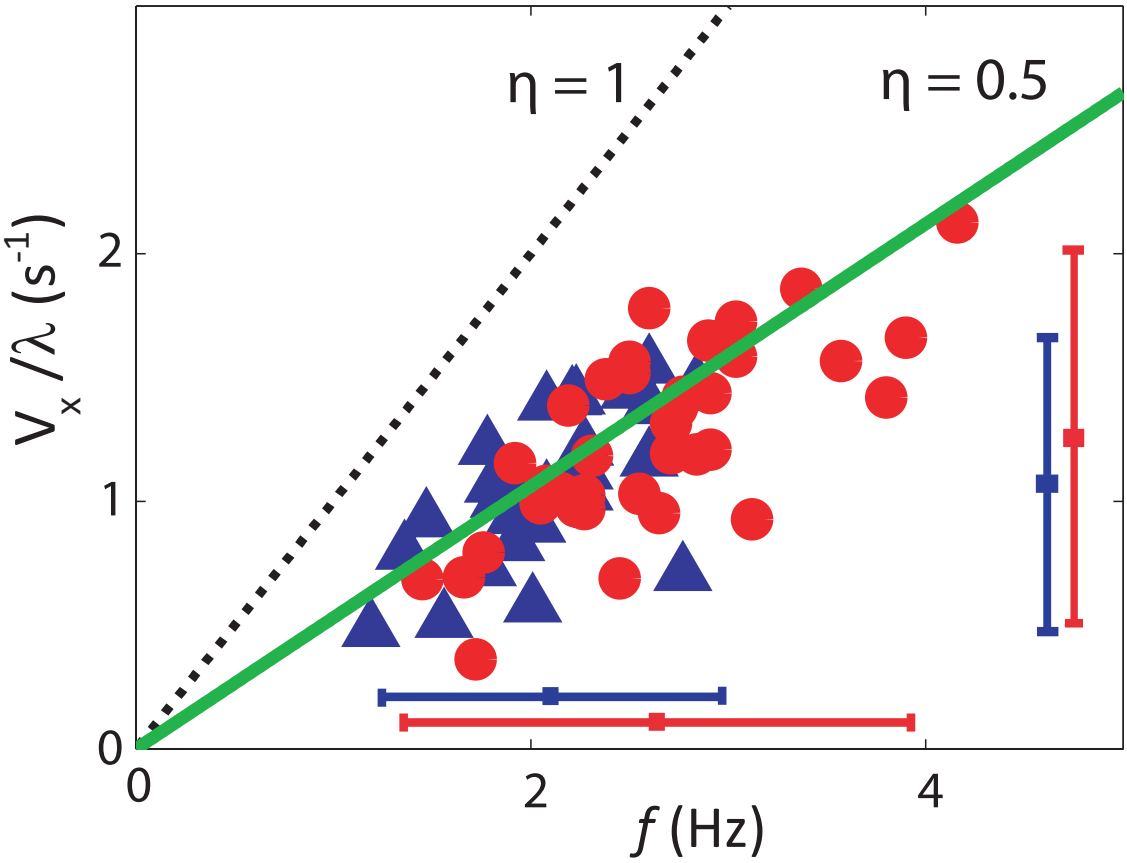

Figure 26: Temporal characteristics of the sandfish kinematics as it swam within loosely and closely packed granular media. Red circles (close packed, N= 24), and blue triangles (loose packed, N= 22) show dependence of swimming velocity on wave frequency. Slope of green line is wave efficiency η of animal (see text and values in Fig. 27), dashed black line represents $\eta = 1$. The horizontal and vertical blue and red bars (mean $\pm$ SD) represent the range of frequencies and forward velocities accessed in loose packed (2.10 ± 0.75 Hz, 0.98 ± 0.27 bl/s) and close packed (2.63 ± 1.13 Hz, 1.28 ± 0.37 bl/s) respectively. The average frequency and average speed were greater in close packed than in loose packed (Students t-test, $p < 0.01$). The glass particle size was 0.3 mm. N = 46 trials were recorded.

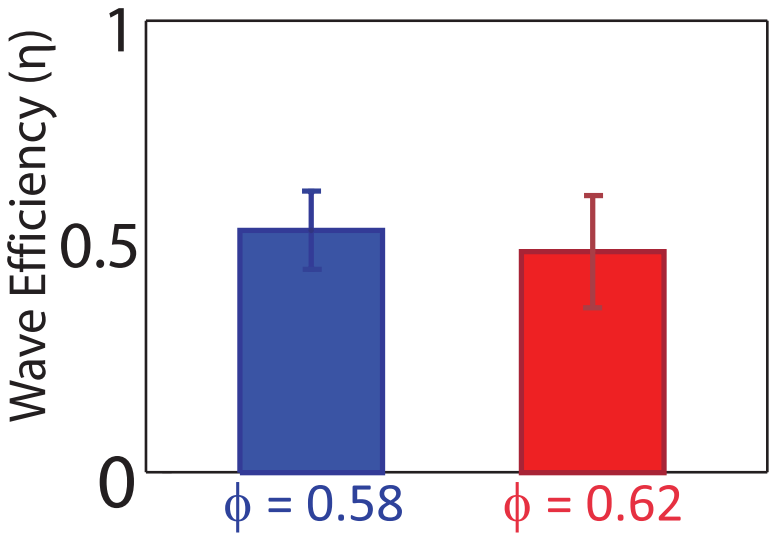

Figure 27: Wave efficiency (slope of the velocity frequency relation) of the sandfish as it swam within loosely (blue) and closely (red) packed 0.3 mm granular media.

was reduced by a constant factor η so that $v_x = \eta f \lambda$ with $\eta = 0.53 \pm 0.04$ (see Fig. 26). Since $v_w = f\lambda$, this implies that the average forward speed is a fraction of the wave speed. Thus the animal was not moving in a tube, which can be seen in Fig. 22, since successive undulations did not trace a continuous path. Instead, tracer particles placed in the bulk revealed that there was backward displacement of material as the animal moved forward. Slipping while progressing is common to undulatory swimmers in deformable media across length scales (e.g. eels and spermatozoa in fluids [3], see Chapter I, Section 1.2.3 for details) and is characterized by the wave efficiency (η) [48], defined as the ratio between the forward speed of the animal (v_x) and the velocity of the wave traveling down its body (v_w), i.e. $\eta = v_x/v_w$. Since λ for the sandfish was independent of f in our experiments, η was the slope of the v_x/λ vs. f curve (see Fig. 26 and 27).

Typical wave efficiencies of organisms while moving in fluids at low Re (like nematodes) are 0.25 [47], nearly a factor of two smaller than the sandfish, while organisms undulating (creeping) along the solid surface of an agar-air interface can have η close to unity ($\eta \sim 0.8 - 0.9$ [48]) because deformations in the surface allow movement that is effectively in a tube. It is interesting to note that η for the sandfish in granular media is intermediate to that for fluids and solids, and is independent of ϕ, even though materials with different ϕ

have quite different penetration resistances [74].

In [82], we presented a Resistive Force Theory * (not part of this dissertation) which provided insight into why η did not change significantly for different media preparations. This result was especially remarkable because drag forces between closely and loosely packed material differ by $\sim 80\%$. The model indicated that η was essentially constant because thrust and drag forces scaled by the same ratio of 2.1 within both closely and loosely packed material, and it was this ratio that determined η. The model also implied that η was greater than in low-Re fluids because of the greater thrust to drag force ratio in the frictional granular media.

We also used the RFT to test the hypothesis that the animal swims in a so-called 'frictional fluid' [107], such that flowing grain-grain and grain-animal friction determines the thrust and drag forces. Such a frictional fluid superficially resembles low Re swimming in that there is no inertia, but the mechanism for drag is frictional, rather than viscous. Movement in a frictional fluid differs from non-inertial crawling on a surface in which anisotropic friction [originating from, for example, deforming the surface and pushing off as does nematode on agar [48] or using overlapping belly scales or changes in weight distribution as a snake does [89]] generates a net propulsive force without a net flow of material.

2.2.5 Effect of particle size on sandfish kinematics

To reduce the computational time required (by nearly 8 times) to simulate the medium used in our numerical sandfish simulation (Chapter III) we tested the ability of the sandfish to swim in larger sized 3 mm spherical glass particles prepared into loosely and closely packed states.

High speed x-ray imaging experiments revealed that as in the smaller particles, the sandfish (5 animals; mass = 16.9 ± 4 g; body-length (bl) L = 8.8 ± 3.3 cm) swam subsurface in the 3.2 ± 0.2 mm particles with comparable performance.

The sandfish took significantly longer (1.2 ± 0.6 s) to complete the burial process in 3 mm particles as compared to 0.3 mm particle. Once subsurface the animal placed its limbs

*Developed by Yang Ding a PhD Physics student in the Goldman group

Figure 28: The sandfish lizard on 3 mm glass particles.

along its sides and advanced forward by executing high amplitude body undulations. We quantified the subsurface motion by tracking the mid-line of the animal.

As in [82], the undulatory motion of the animal mid-line was well fit by a posteriorly traveling single-period sinusoidal wave (Eqn. 1, $R^2 > 0.9$). The spatial characteristics of the wave, A and λ, did not vary significantly within a run or between runs and their ratio was conserved at approximately $A/\lambda = 0.2$. A (average 0.18 $\pm$ 0.03 bl, P = 0.26) and λ (average 0.72 $\pm$ 0.1 bl, P = 0.13) was not significantly different for loosely and closely packed media preparations. The sandfish maintained a single period wave along its body as it swam subsurface. As within 0.3 mm particles [82], the animal increased its forward velocity by increasing its undulation frequency (Fig. 29).

In the 3 mm particles, $\eta = 0.54 \pm 0.13$ (slope of the v_x/λ vs. f curve in Fig. 29) was not significantly different for the different media preparations tested (P = 0.25). The η measured for the sandfish in 3 mm particles was similar to that measured for the 0.3 mm particles [82]. For the sandfish, η was independent of both particle size and media preparation (see Fig. 30).

2.2.6 Sagittal plane view of the sandfish kinematics

To test whether the sandfish was undulating in a two dimensional horizontal plane we rotated the c-arm x-ray system by 90° to image the sagittal kinematics of the sandfish. Data were collected with 0.3 mm glass particles as the granular medium.

Side view x-ray imaging of the sandfish subsurface showed that the animal undulated in a plane at $\sim 22.2 \pm 3.7°$ with respect to the horizontal. Once the animal achieved this angle

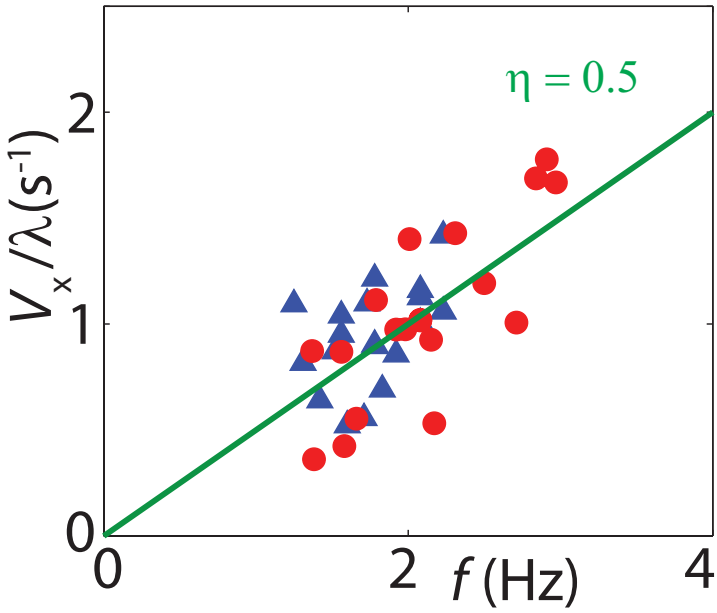

Figure 29: Temporal characteristics of the sandfish kinematics as it swam within 3 mm glass particles. The red circles and blue triangles correspond to the closely and loosely packed media. The green line corresponds to $\eta = 0.5$.

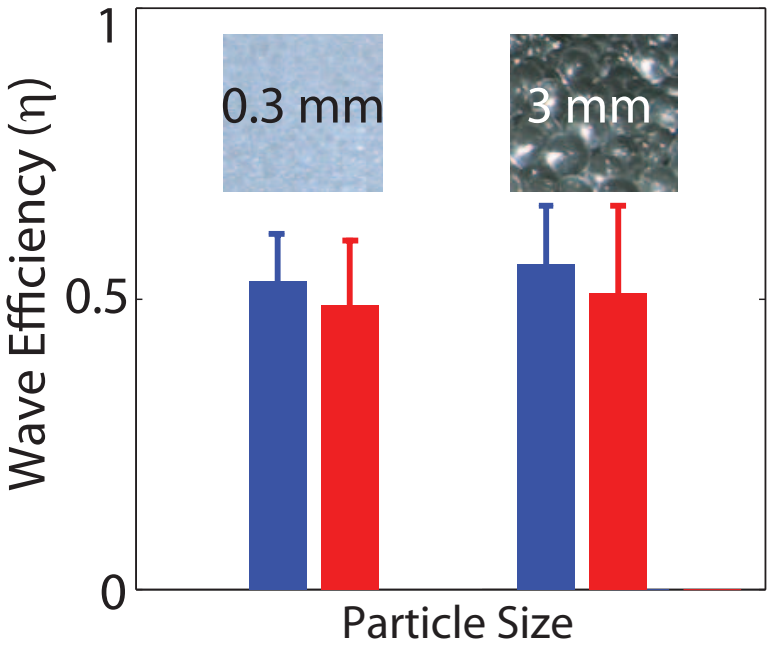

Figure 30: Comparison between the wave efficiency of the sandfish as it swam in 0.3 mm and 3 mm glass particles prepared into loosely (blue) and closely (red) packed states. Images of the particles are shown as insets.

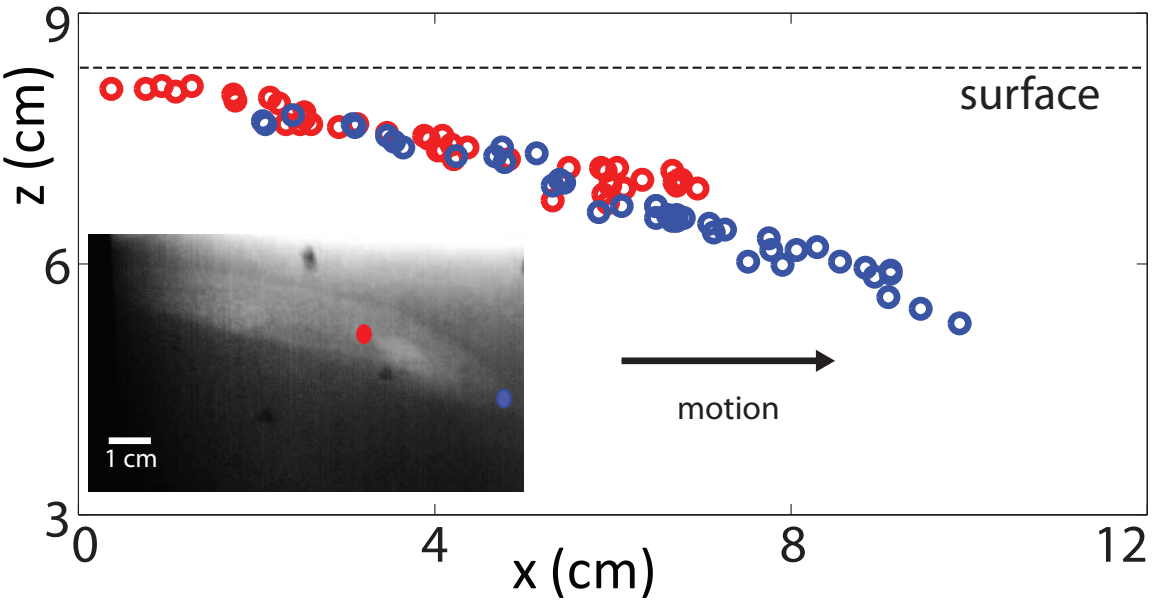

Figure 31: Sagittal plane view of the sandfish trajectory as it swam subsurface obtained using x-ray imaging. The blue and red circles correspond to the position of the animal's snout and 40% of its body-length measured from its snout. Inset shows a side view x-ray image of the sandfish as it swam within 0.3 mm glass particles.

its continued to move forward by oscillating in this plane and buried itself consistently to a depth of 2.1 ± 0.5 cm (surface to top of mid-point of the back), independent of volume fraction (Student's t-test, $p > 0.05$).

2.2.7 Measurement of friction between the sandfish skin and the granular medium

To estimate the friction of the sandfish skin against the glass particles (0.3 and 3 mm) we used the technique described in [60]. The sandfish was anesthetized using 5% isofluorane provided by 1 Lpm O_2 in a 1-L chamber. The sandfish was then arranged with its ventral surface placed on an inclined plane which was homogeneously covered with a mono-layer of either 0.3 or 3 mm glass particles. The edge of the inclined plane was then lifted by hand until an inclination ϕ was reached at which the sandfish began sliding, and the static friction coefficient $\mu = tan(\phi)$ was calculated. Trials in which the sandfish rolled instead of slid were not analyzed; in all, 10 friction measurements were made. The sandfish-particle friction measured for 0.3 mm and 3 mm glass particles were 0.20 ± 0.01 and 0.27 ± 0.01.

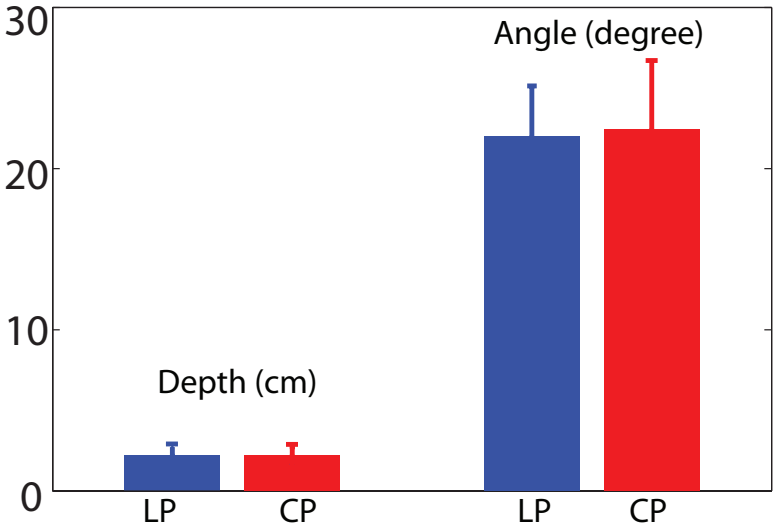

Figure 32: Burial depth and angle of entry of the sandfish as it swam within loosely (LP, blue) and closely (CP, red) packed granular media. The data were obtained by x-ray imaging the sagittal view of the sandfish trajectory subsurface within 0.3 mm glass particles.

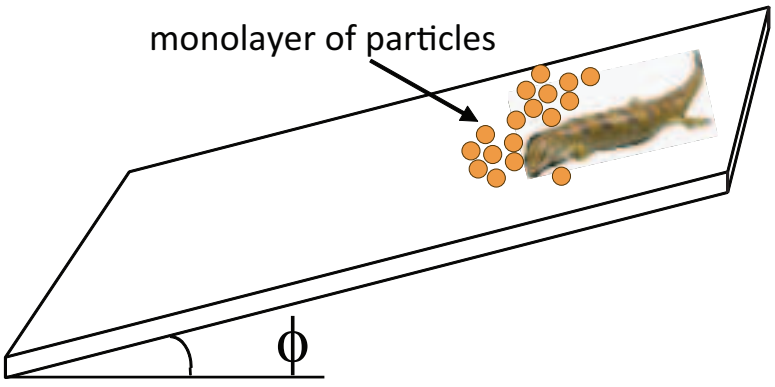

Figure 33: Measurement of friction between the sandfish skin, and 0.3 mm and 3 mm glass particles. The experimental apparatus, an inclined plane, was used to measure the static friction coefficient (μ) of the ventral surface of an anesthetized sandfish.

2.3 Conclusion

We used high speed x-ray imaging to reveal that once subsurface the sandfish propelled itself within granular media by using body undulations without limb use. The undulatory kinematics of the sandfish were well fit with a sinusoidal traveling wave that propagated posteriorly along its body. We found that the wave efficiency, the ratio of its average forward speed to wave speed, of the animal was approximately 0.5, independent of the media preparation (loosely and closely packed). We demonstrated that the performance of the animal within a granular medium was intermediate to that of other organisms within low Re viscous fluids and on frictional solid surfaces. We also showed that the ability of the sandfish to undulate to propel forward existed over a range of particle size, and its wave efficiency was independent of particle size.

Our results demonstrated that burrowing and swimming in complex media can have similar complexity to movement in air or water, and that organisms can exploit the solid and fluid-like properties of these media to move effectively within them.

CHAPTER III

NUMERICAL SIMULATION OF SAND-SWIMMING

Our previous study of a sand-swimming lizard, the sandfish, *Scincus scincus* (described in Chapter II), revealed that the animal swam within granular media at speeds up to 0.4 body-lengths/cycle by propagating a traveling wave posteriorly along its body without limb use. We developed an empirical resistive force theory (not part of this dissertation) that predicted the performance of the animal within granular media (i.e. wave efficiency to within 20%) [82]. The RFT predictions are however based on several assumptions: the forces experienced by the sandfish are velocity independent, the average thrust and drag forces are good approximations of these forces at slow swimming speeds. These assumptions make understanding the particle level medium dynamics and identifying the effect of parameter variation difficult (and risky). A more accurate and flexible approach for such an analysis is to use Discrete Element Methods (DEM) [101]. Once a validated model of the medium is developed, it is possible to avoid having to empirically establish force laws (that describe thrust and drag) each time the property of the media is varied (an RFT requirement), by varying the media property directly in simulation. Also, variables related to flow and grain-level physics can be understood, making it possible to develop better theoretical models.

We developed a numerical simulation that combines a model of the animal with the validated granular medium model. We used this tool to investigate the effects of varying parameters A, λ, and ξ, variables which we have no direct control over in the biological experiment. First we describe the development of the simulation approach and compare its predictions of η to the animal experiment. We then vary kinematic parameters to systematically demonstrate an optimality condition for undulatory swimming in granular media*.

*The work presented in this chapter is part of a paper in review. Maladen R.D, Ding Y, Umbanhowar P.B, Kamor A, and Goldman D.I, *Mechanical models of sandfish locomotion reveal principles of high performance subsurface sand-swimming*, Journal of the Royal Society Interface

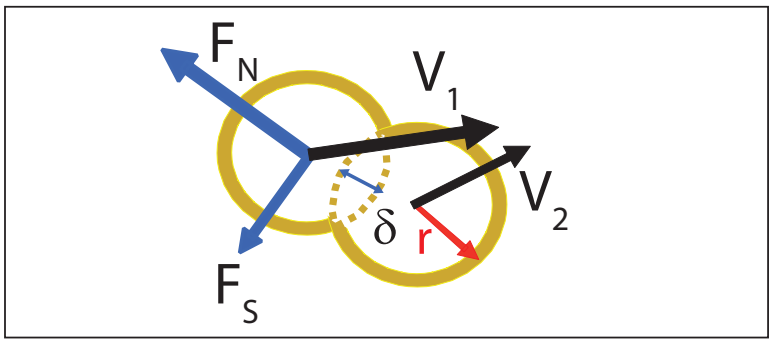

Figure 34: Forces on two representative contacting particles whose interaction forces are given by Eqn. 2. F_N and F_S correspond to the normal and tangential forces respectively. δ, r, v_1, and v_2 correspond to the virtual overlap between interacting particles, and the radius and velocities of the particles respectively.

3.1 Simulating the granular media

The granular medium was simulated using a 3D soft sphere DEM code [101] *. Using a DEM model allowed us to directly model each grain-grain interaction to produce models of bulk granular flow. The grain-grain model includes a normal elastic restoring force, a normal dissipation (mimicking energy loss during collision), which depends on collision velocity, and tangential dissipative frictional forces. It has been shown that when the microscopic physics of the particle-particle interaction is captured, the bulk medium properties (even structures at grain level), agree remarkably [15]. To compute particle-particle and particle-object interaction forces we calculated the normal force [72], F_n, and the tangential Coulomb friction force, F_s, (see Fig. 34) acting at each contact with

$$\begin{aligned} F_n &= k\delta^{3/2} - G_n v_n \delta^{1/2} \\ F_s &= \mu_{pp} F_n, \end{aligned} \tag{2}$$

where δ is the virtual overlap between interacting particles, v_n is the normal component of relative velocity, and k, G_n, and μ_{pp} represent the hardness, viscoelastic constant, and the particle–particle friction coefficient respectively (see Table 1 for specific values).

*Developed by Yang Ding a PhD Physics student in the Goldman group

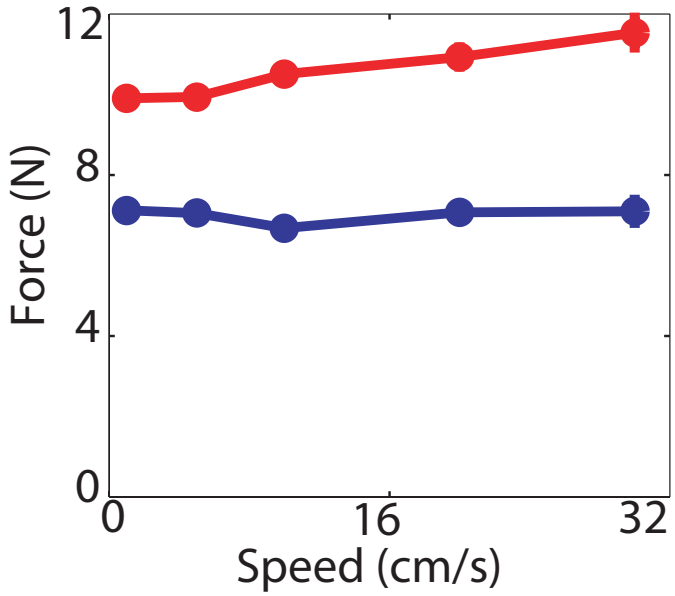

Figure 35: Forces measured by dragging a rod through granular media were independent of speed ($< 40\,\mathrm{cm/s}$) for both loosely (blue) and closely (red) packed states. 3 runs were collected for each speed. The deviation in force measured was comparable to the symbol size. The rod was dragged at a fixed depth of 7.62 cm within 0.3 mm glass particles.

3.1.1 Validating the simulated granular media

The simulated medium (3 mm glass beads, density 2.5 g/cm^3) was validated by comparing the forces on a cylindrical stainless steel rod (diameter = 1.6 cm, length = 4 cm and rod-particle static friction coefficient $\mu_{bp} = 0.15$) dragged through it with those measured from experiment (see Fig. 36). Previous studies had showed that drag in granular media was independent of speed [1, 120]. To test if this effect persisted in the regime relevant to the sandfish, we dragged the rod oriented perpendicular to velocity at 1, 5, 10, 20, and 30 cm/s (which covers the sandfishs range of speeds) at a fixed depth of 7.62 cm and found that over an order of magnitude change in speed, force only changed by 10% in 0.3 mm glass particles (see Fig. 35, [82]).

The drag tests to validate the simulated media were performed at a constant speed of 5 cm/s with the object's vertical mid-point at depth $d = 7.6$ cm and its long axis parallel to the motion direction (see Fig. 36 inset). In experiment, the cylindrical rod was attached to a robotic arm (CRS Robotics) via a thin but stiff supporting rod which moved the intruder at constant depth and velocity while a 6 d.o.f. force sensor (ATI industrial) mounted to

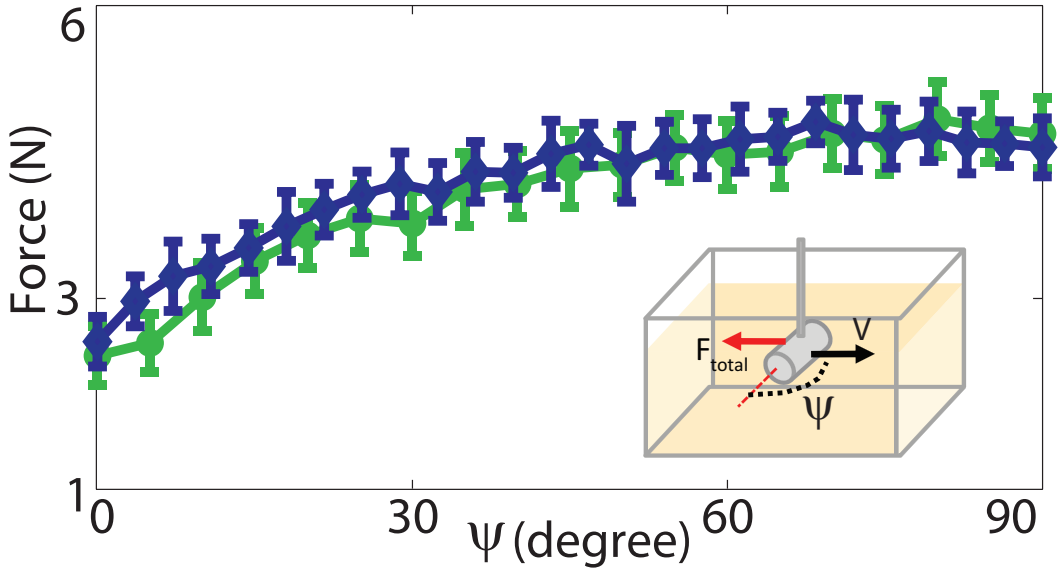

Figure 36: Simulated granular media was validated by comparing the forces on a rod dragged through it with those measured from experiment. Total force on a stainless steel rod (sides and ends) (diameter = 15.8 mm, length = 40 mm, and rod-particle static friction coefficient $\mu_{bp} = 0.15$) immersed to a depth of 7.62 cm was measured as a function of the angle (ψ) between the velocity direction and its orientation in experiment (green) and simulation (blue) in a loosely packed medium. The inset shows the experimental setup.

the robotic arm measured the drag force. The force on the supporting rod was measured separately and subtracted from the total force on the rod with the object attached to obtain the force on the object alone. The test was repeated three times for each object. The particle-particle restitution and friction coefficients were experimentally measured while the hardness was selected such that particle overlap (δ) is $< 0.4\,\%$ the particle radius (see Table 1). The container holding the particles was $35 \times 15 \times 9\,\mathrm{cm}^3$ in extent. The deviation between experimentally measured and simulated drag force as a function of angle was less than 10%.

3.2 Simulating the sandfish

The multi-segment numerical model of the simulated sandfish was developed using the commercial software package Working Model 2D (Design Simulation Technologies). The multi-body solver integrates the equations of motion of the coupled links such that it can reproduce the motion of the animal. The model was divided into 50 motor actuated segments along its length (see Fig. 37).

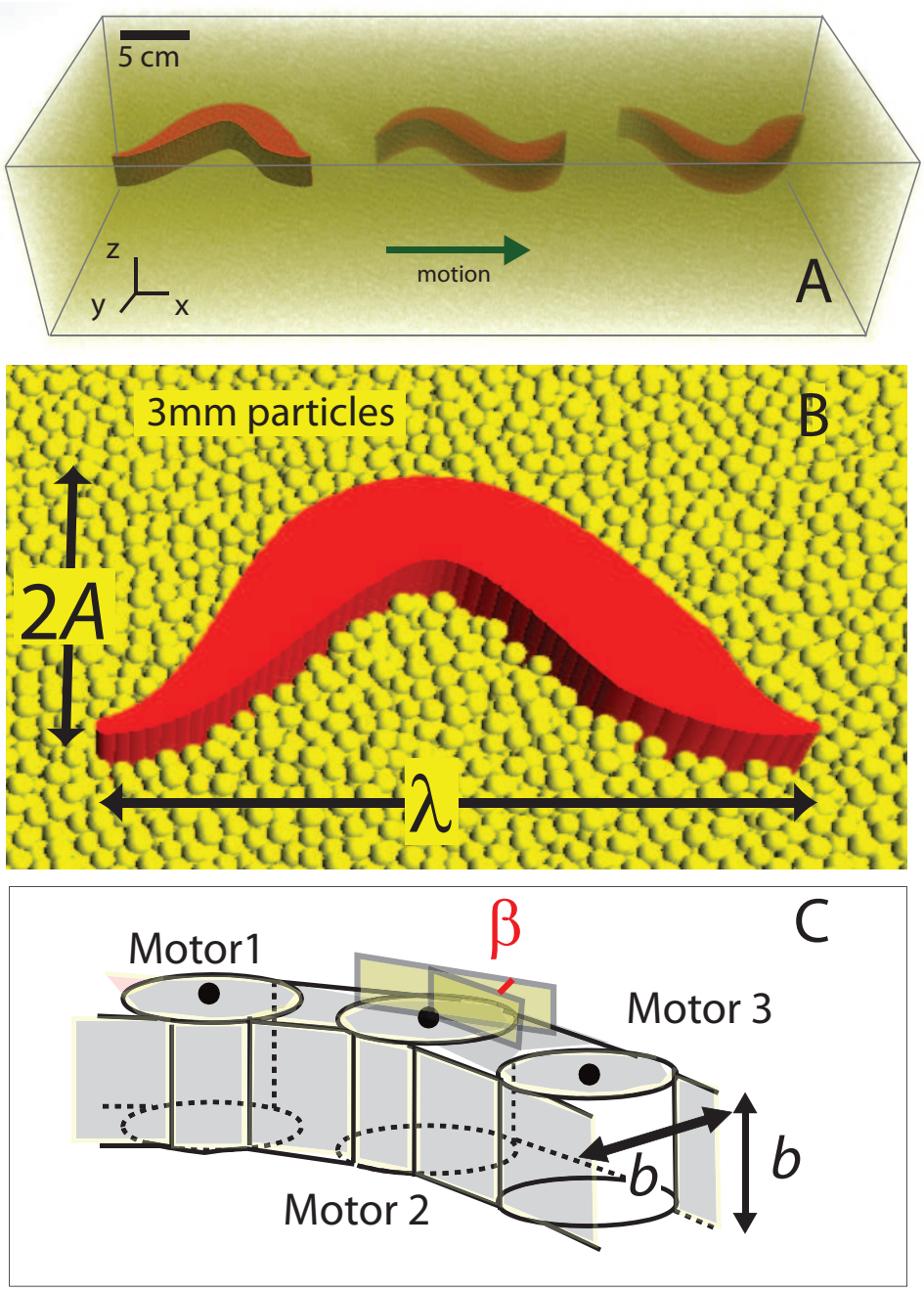

Figure 37: (A) 3D view of the simulated 50 segment sandfish at 3 different instants as it swims within a container of experimentally validated 3 mm glass particles. The particles are rendered semi-transparent for visualization. (B) Close up view of the numerically simulated sandfish that swims like the animal in 3 mm glass particles. A and λ correspond to the amplitude and wavelength of the simulated sandfish. Particles above the sandfish model are rendered transparent. (B) Inter-motor connections of a section of the simulated sandfish. b indicates both the width (the maximum along the model) and height of the segments in the non-tapered section of the animal model. The angle between adjacent motors was modulated using Eqn. 3.

Table 1: Experimentally measured and simulated parameters of the 3 mm glass particles.

	Experiment	Simulation
Hardness (k)	5.7×10^9 kg s^{-2} m$^{-1/2}$	2×10^6 kg s^{-2} m$^{-1/2}$
Restitution coefficient	$0.88 - 0.98$, 0.92 ± 0.03	0.96
G_n		15 kg m$^{-1/2}$ s^{-1}
$\mu_{particle-particle}$	0.10	0.10
$\mu_{particle-body}$	0.27	0.27
Density	2.47 g cm^{-3}	2.47 g cm^{-3}

Each motor angle was constrained so that an approximate sinusoidal wave travels posteriorly from head to tail (Fig. 37). The angle (β) between segments i and $i+1$ was varied as

$$\begin{aligned}\beta(i,t) = \tan^{-1}\left[\frac{2\pi A}{\lambda}\cos\left(\frac{2\pi}{\lambda}x_{i+1} + 2\pi f t\right)\right] \\ - \tan^{-1}\left[\frac{2\pi A}{\lambda}\cos\left(\frac{2\pi}{\lambda}x_{i} + 2\pi f t\right)\right].\end{aligned} \tag{3}$$

We performed simulations for a model that closely matched the animal, tapered in the coronal plane (Fig.3 a) by varying its width uniformly from the snout tip to 1/6 bl, and from 3/5 bl to the tail tip. To test the effect of head drag on performance we also tested a simulated animal with a cross–section approximated as a square tube. Both models tested did not incorporate limbs since the sandfish placed its limbs along its sides during subsurface swimming. We tested a simulated animal with segments of appropriate length (limbs) placed at locations along the body obtained from animal measurements. We found that with the segments extended perpendicular to the body segment (to which they were attached) η decreased by nearly 15% due to the increased drag force. No tapering in height of the body along its length was considered as doing so resulted in the model rising due to drag induced granular lift. This lift resulted from the vertical component of the normal force on an inclined surface dragged through a granular medium and is discussed in [30] and in Chapter IV, Section 4.7.2. Model properties such as animal dimensions and density were taken from biological measurements (refer to Table 2 for values). The segment height and maximum segment width, both were denoted by b for the model. The particle - sandfish

Table 2: Parameters of the sandfish measured in experiment and used in simulation.

	Experiment	Simulation
Amplitude/Wavelength	0.25 ± 0.05	0.22
Length (Snout to tail tip)	12.8 ± 0.3 cm	12 cm
Weight	16.2 ± 4 g	16 g
Max. diameter	1.63 ± 0.11 cm	1.6 cm

body friction $\mu_{pb} = 0.27$ was determined by measuring the angle at which an anesthetized sandfish slid snout-first down a mono-layer of 3 mm glass particles glued to a flat plate (See Chapter II, Section 2.2.7).

The multi-segment model of the animal was combined with the previously described experimentally validated discrete element model of the granular medium such that Working Model integrated the equations of motion of the coupled links that represented the animal and discrete element model calculated the resultant force from both the particle-particle and body-particle interactions. At each time step the net force due to particles on each segment were passed to Working Model and velocity and position information of the model segments transferred back to the discrete element model. The animal model kinematics were constrained to prevent rotation of the axis of the traveling wave out of its horizontal plane of motion (roll).

3.3 Results

3.3.1 Temporal characteristics of the numerical sandfish kinematics

Based on the measurements in the biological experiments of the sandfish as it swam within 3 mm glass particles (see Chapter II, Section 2.2.5) we fixed $A/\lambda = 0.2$ and number of periods $\xi = 1$, and tested the effect of varying oscillation frequency f on forward speed v_x. The forward velocity of the simulated sandfish increased linearly with oscillation frequency as in the animal experiments and as predicted by the RFT [81]. The slope of this relationship, which is the wave efficiency η, was 0.57, close to $\eta = 0.54$ observed for the animal.

The sandfish modeled as a square cross-section tube (flat head) moved with a lower wave efficiency of $\eta = 0.45$. The difference in η between the flat and tapered head sandfish

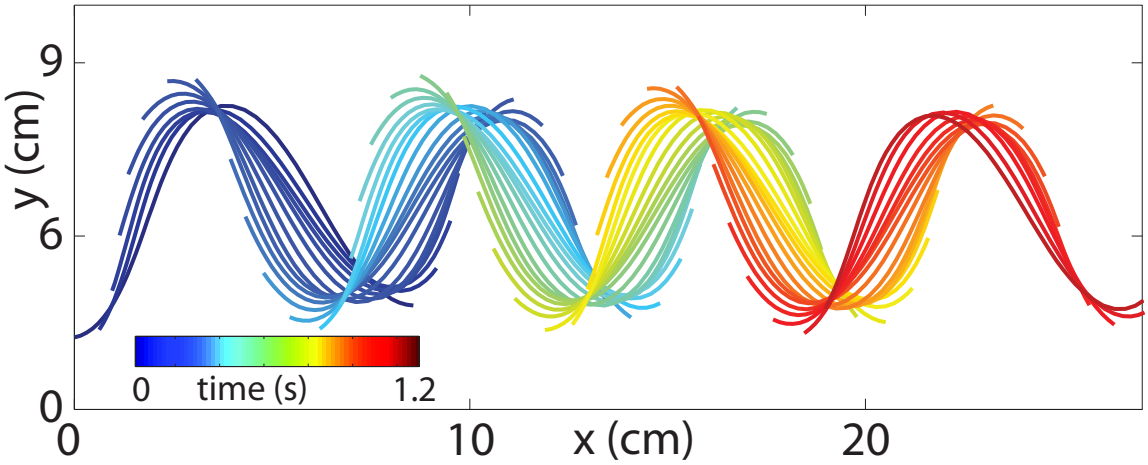

Figure 38: Mid-line kinematics of the numerical sandfish as it swam within a validated 3 mm granular media model. The oscillation frequency of the simulated sandfish was 2.5 Hz. The color bar represents time.

models tested can be attributed to the difference in the associated head drag.

3.3.2 Spatial characteristics of the numerical sandfish kinematics

To this point, we limited our investigation of sand-swimming to parameters used by rapidly escaping sandfish, i.e. a sinusoidal traveling wave with fixed kinematics ($A/\lambda = 0.2$ and $\xi = 1$). We now use the numerical simulation to investigate how sand-swimming depends on variation of the spatial form of the sinusoidal wave. This allows us to advance an argument for why the animal utilized only a limited range of A, λ, and ξ.

Since the sandfish has a constant body-length, as we vary A, λ also varies. We varied A/λ for a single period wave along the body of the simulated sandfish and measured the corresponding η. For a given oscillation frequency, η increased quadratically for small A/λ, increased rapidly for intermediate A/λ, and varied slowly for large A/λ. As the amplitude of the simulated sandfish increased the projection of a segment along its body perpendicular to its direction of forward motion increased which increased the associated thrust and explains the increase in η as a function of A/λ.

For slender swimmers in low Re fluids [47] the normal and tangential forces on an segment are simply proportional to their respective velocity components with coefficients

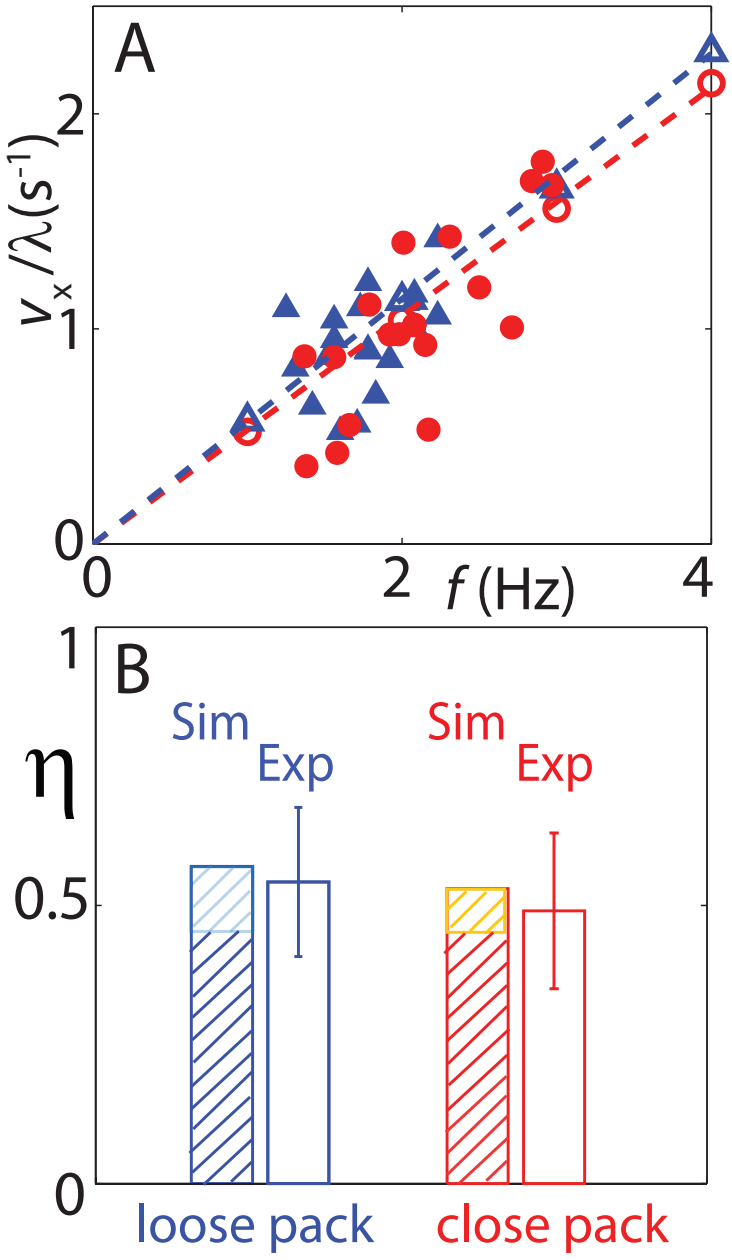

Figure 39: (A) Average forward speed vs. undulation frequency as the sandfish swam within 3 mm glass particles. Solid symbols refer to biological measurements, and the dashed lines with open symbols correspond to simulation predictions, respectively. (B) Wave efficiency η, the ratio of the forward swimming speed to the wave speed as determined from the slope of v_x/λ vs. f relationship measured from (A) for biological data and numerical simulation. For the simulation, the lower and higher limits of the η deviation (cyan and orange thatch) correspond to flat and tapered head shapes, respectively. Blue and red colors in (A) and (B) correspond to loosely and closely packed media preparations, respectively.

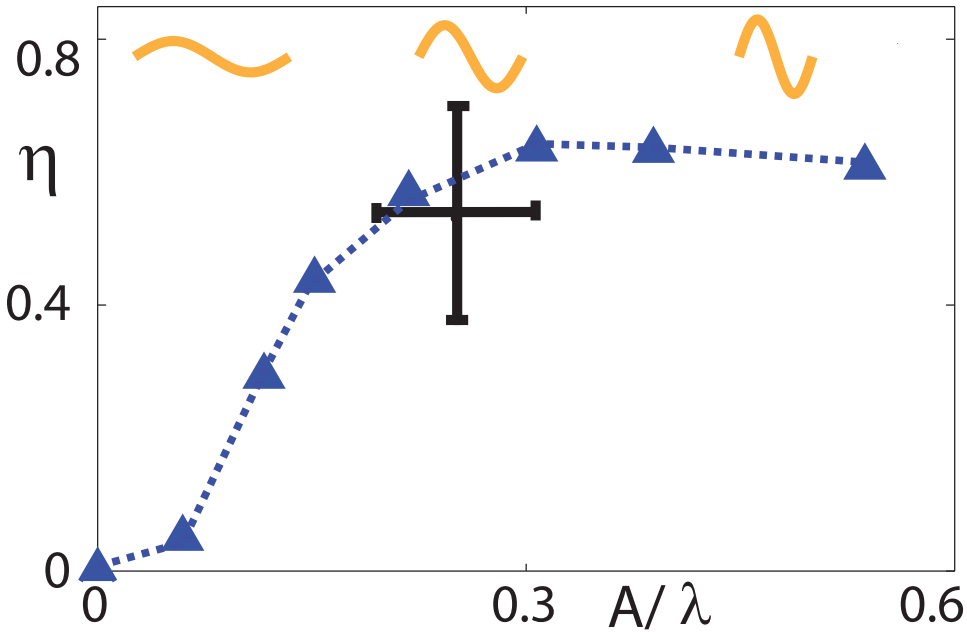

Figure 40: Effect of varying the spatial characteristics of the numerical sandfish kinematics on swimming performance within validated 3 mm glass particles. Wave efficiency η vs. amplitude to wavelength ratio A/λ for the numerical model with a tapered body (dashed and triangles, $\xi = 1$, and $f = 4$ Hz). The black cross corresponds to the animal experiment. Spatial forms are depicted by orange curves.

in the ratio 2 : 1. Although we used a similar RFT approach for swimming in granular media to that used for low Re swimmers, the force laws were modified since the granular thrust and drag forces have a complex relation with the orientation of a segment along the undulator's body and its velocity direction. Also, the granular medium provides the undulator with greater thrust due to its finite yield stress which results in the magnitude of η being generally larger than, and its slope (as a function of A/λ) different from low Re swimmers.

3.4 Testing the kinematic conditions that maximize sand-swimming speed

The numerical simulation agreed with the RFT prediction that the animal can increase η by increasing A/λ (see Fig. 40), but we found that the animal did not operate at the highest A/λ. Maladen et al. [82] showed using the RFT model that operating at a large A/λ came at a cost; since the animal is of finite length, the distance it could travel per cycle decreased with increasing A/λ. We can see this by expressing body-lengths traveled per cycle as

$$v_x = \eta f \lambda v_x / fL = \eta \lambda / L. \tag{4}$$

While η increases with increasing A/λ, λ decreases and thus a maximum in forward progress per cycle can be expected Fig. 41. These competing effects represent a granular media effects (η), and a geometric effect (for a fixed body-length undulator when A is varied λ automatically gets prescribed). Qualitatively, for non-inertial swimmers, the maximum distance that maybe progressed by the organism per cycle is its wavelength so increasing A/λ decreases λ which results in a lesser maximum distance than can be progressed per cycle. However, the higher A/λ increases η which results in a greater percentage of the wavelength (or maximum distance) being progressed per cycle.

The numerical sandfish simulation (and as predicted by RFT [82]) displayed a maximum in the forward progress per cycle at $A/\lambda \approx 0.2$ ($\xi = 1$, see Fig. 43). Like the plot of η vs A/λ, the deviation between speed predicted by the RFT and numerical simulation was small for small A/λ and increased once inter-segment interaction became important. The biological data resides at the peak of the curve, indicating that the animals were maximizing their sand-swimming speed. This result agreed with the biological hypothesis that sandfish burial is an escape response [7].

To test the effect of number of wave periods on performance, we fixed $A/\lambda = 0.2$ and varied $0.6 < \xi < 1.6$. We found that the simulated sandfish progressed forward fastest for approximately a single period along its body (Fig. 44). The animal, as mentioned before, operated close to the maximum speed predicted by the models for the same kinematic parameters (Fig. 44).

We can understand the dependence of speed on ξ. For non-integer ξ the sandfish model experienced an unbalanced torque that resulted in a periodic yawing motion (with an amplitude of more than 40° for $\xi = 0.5$) which caused A to become effectively smaller and which resulted in lower η and lower v_x. For $\xi > 1$, decreased v_x resulted from a lower η due to the decrease in A required to keep A/λ fixed.

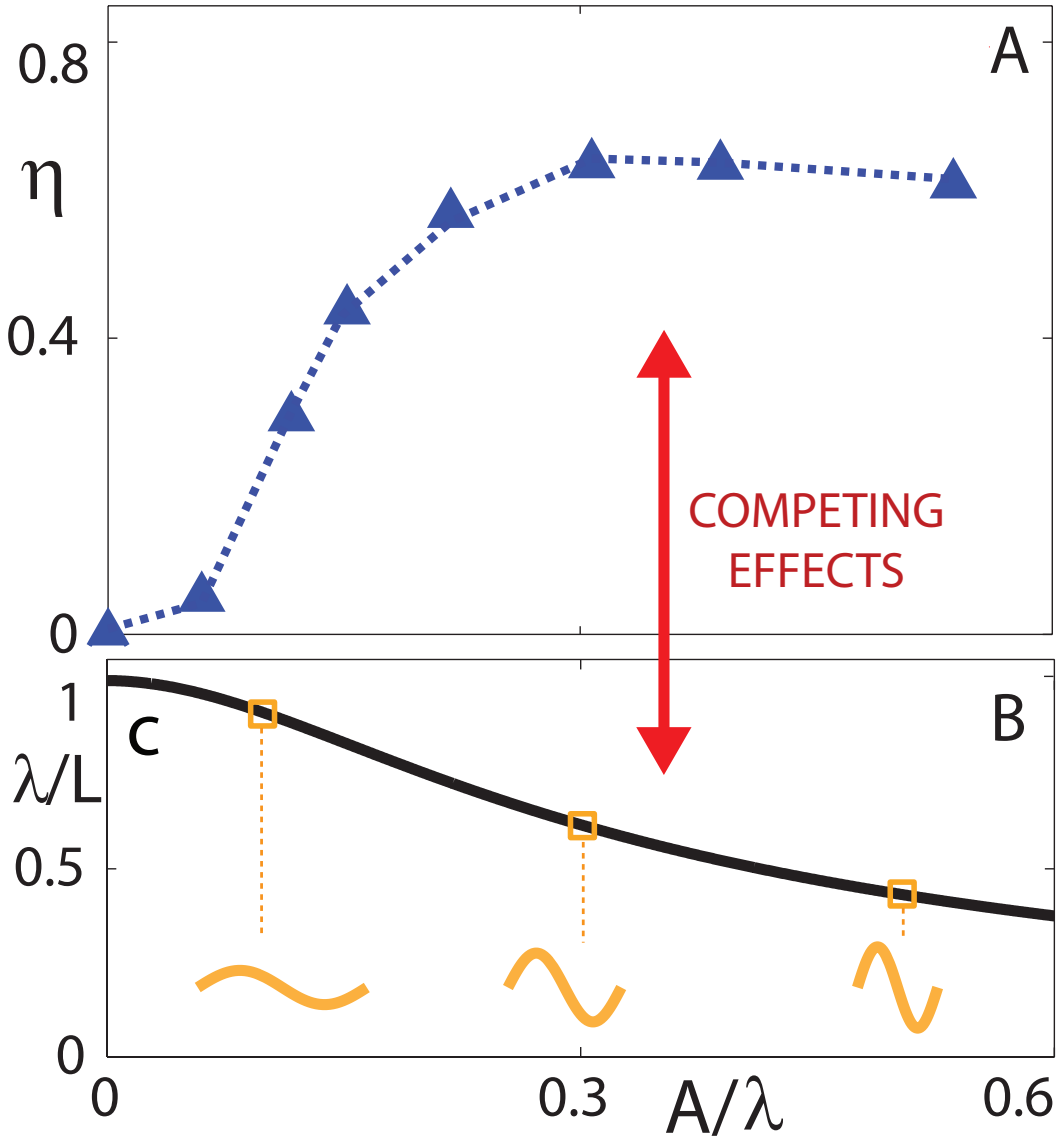

Figure 41: Competition between η and λ with varying A revealed that optimal kinematics which maximize forward sand-swimming speed can be expected. (A) Wave efficiency η vs. amplitude to wavelength ratio A/λ for the numerical model with a tapered body (dashed line and triangles, $\xi = 1$, and $f = 4$ Hz). (B) For a fixed length undulator, the wavelength decreases with increasing amplitude. Spatial forms are depicted by orange curves.

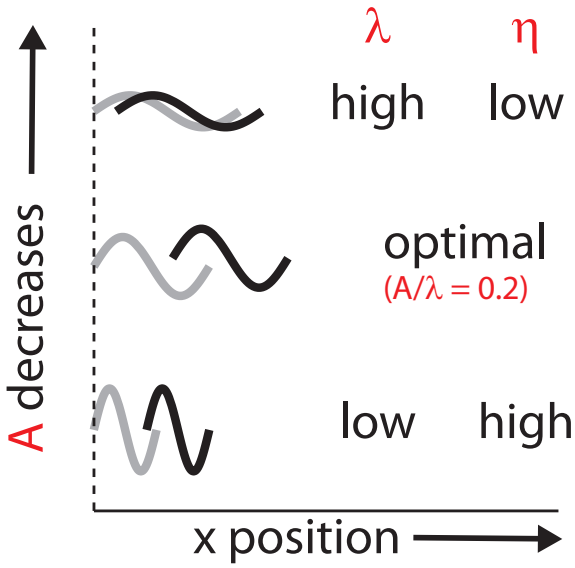

Figure 42: Cartoon describing the functional effect of the competition between η and λ with varying A while keeping $\xi = 1$. As A increases the corresponding η increases while λ decreases. The gray and black curves correspond to the initial and final positions of the undulator after a single cycle of undulation.

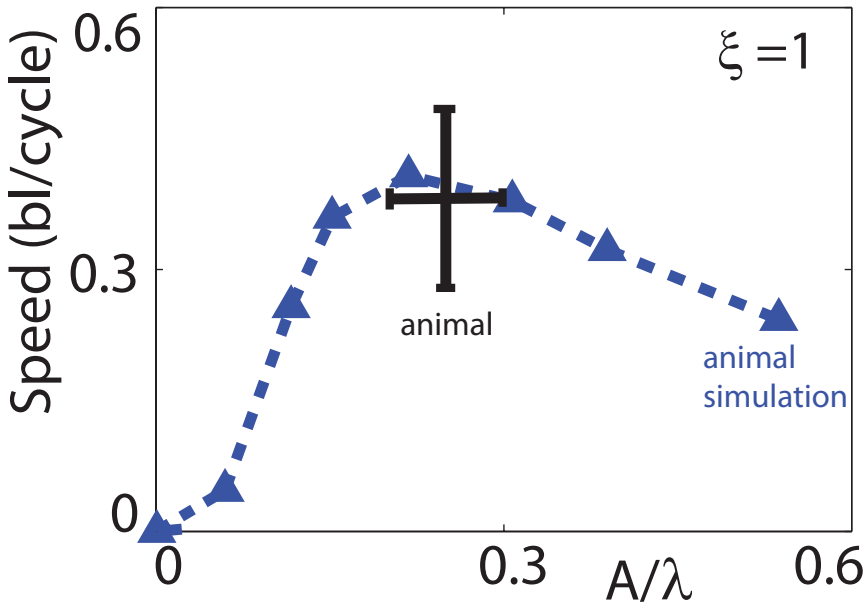

Figure 43: Speed (body-lengths/cycle) vs. A/λ relationship identifies the simulated sandfish kinematics that maximized forward swimming speed. Forward speed per cycle was measured using sandfish simulation for different ratios of A and λ for a single period wave and $f = 2$ Hz (blue dashed curve with triangles). Using a third order polynomial fit to calculate the peak of the sandfish simulation curve identifies the maximum speed $= 0.41 \pm 0.01$ bl/cycle at $A/\lambda = 0.23 \pm 0.01$. Black cross corresponds to measurements from animal experiment.

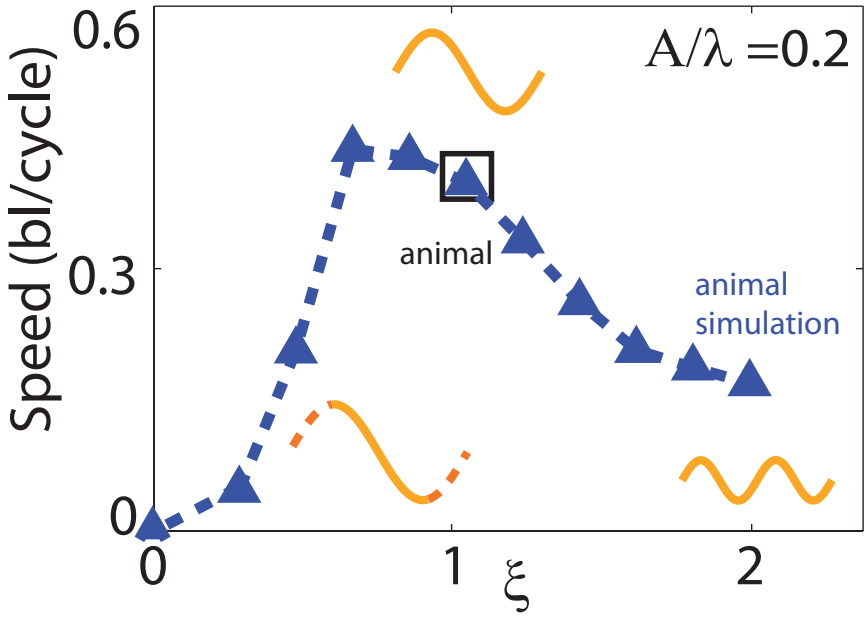

Figure 44: Speed (body-lengths/cycle) vs. ξ relationship identified the simulated sandfish kinematics that maximized forward swimming speed for $A/\lambda = 0.2$. Forward speed per cycle was measured using sandfish simulation for different ξ with $A/\lambda = 0.2$ and $f = 2$ Hz (blue dashed curve with triangles). Black open box corresponds to the single period wave observed in animal experiment. Spatial forms are depicted by orange curves.

3.5 Effect of friction on sand-swimming performance

The performance of a sand-swimmer is dependent on the thrust and drag forces generated by the body. Both these forces are sensitive to particle-particle friction (μ_{pp}) and body-particle friction (μ_{bp}) [82]. We used our numerical sandfish simulation to investigate the effect of varying each of these frictions (while keeping the other fixed) on forward sand-swimming speed. We found that as expected speed of the simulated sandfish decreased with increasing μ_{bp}, but surprisingly, increased with increasing μ_{pp} (see Fig. 45). When both μ_{bp} and μ_{pp} are simultaneously high or low there would be no net effect on the forward speed of the undulator as it swims subsurface.

3.6 Conclusion

Motivated by biological experiments of sandfish locomotion we developed a numerical simulation approach to study undulatory sand-swimming. We used this model to test the predictions of our previously developed empirical resistive force model and demonstrated that

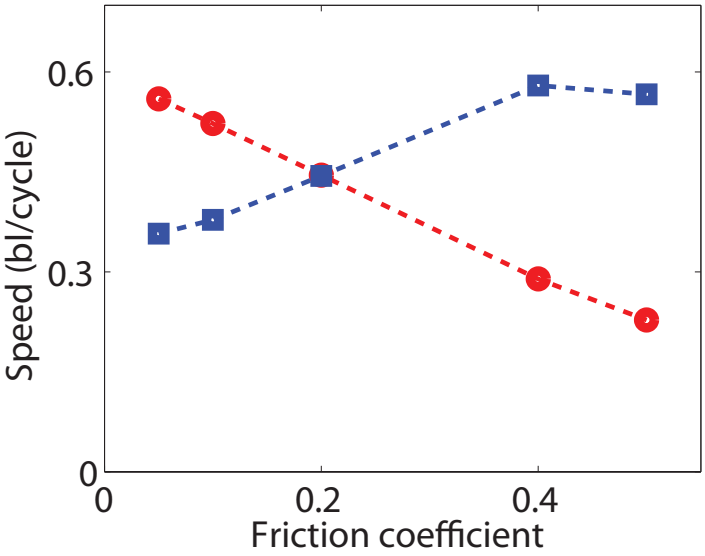

Figure 45: Forward speed of simulated sandfish in 3 mm glass particles was measured as body-particle friction ($\mu_{pp} = 0.1$, red trace) and particle-particle friction ($\mu_{bp} = 0.27$, blue trace) were varied.

limbless undulatory locomotion with η comparable to that of the animal can be achieved within granular media by utilizing the wave kinematics of the animal. We determined how η depends on the spatial characteristics of the undulator and showed that the competing effects of wave efficiency and wavelength determined forward speed, and that an optimal $A/\lambda \approx 0.2$ and $\xi \approx 1$ maximized forward swimming speed. Remarkably, the sandfish uses these optimal kinematics to swim rapidly within granular media [*]. The numerical simulation (once validated against experiment) gives us an understanding of the detailed physics of the granular medium, for example, force and flow fields from the grain perspective [†]. The simulation is a flexible design tool with which parameters like grain-grain friction and animal kinematics can be easily varied to accurately predict performance.

[*]These results are part of a paper in review at the Journal of the Royal Society Interface, *Mechanical models of sandfish locomotion reveal principles of high performance subsurface sand-swimming*, Maladen R.D, Ding Y, Umbanhowar P.B, Kamor A, and Goldman D.I.

[†]These results are part of a manuscript in preparation for the journal Physical Review E, *Mechanics of sand-swimming*, Ding Y, Maladen R.D, and Goldman D.I.

CHAPTER IV

SAND SWIMMING ROBOT

Motivated by biological experiments revealing rapid sand-swimming by the sandfish lizard, and to validate the predictions of the RFT [82] and the numerical sandfish simulation (Chapter III), we developed an undulatory sand-swimming robot. In this chapter we describe the design of this device and show that like the animal, the robot can swim subsurface limblessly using an open loop (traveling wave sinusoid) control scheme. We show that the robot can increase its forward speed by increasing its oscillation frequency, but it moves forward with a lower η than the animal. We develop and utilize a numerical simulation of the robot to provide a potential explanation for the differences between the performance of the physical robot and the biological sandfish. The physical robot is an essential complement to the theoretical and numerical modeling approaches as physical laws that govern the interaction with the granular medium do not need to be simulated [*†]. In the last section, we vary the head shape of the robot to test the biological hypothesis that the shovel shaped head of the animal allows it to bury rapidly into sand[‡]. The design tools (physical and simulated robot) developed here can lead to an improved understanding of how organisms exploit the solid and fluid-like properties of granular media to move effectively within it. Results of this work will also guide the creation of robots that can locomote effectively within complex environments.

---

*The design of the robot had been published in the proceedings of the peer-reviewed conference - Robotic: Science and Systems. Maladen RD, Ding Y, Umbanhowar PB, Kamor A, and Goldman DI, *Biophysically inspired design of a sand-swimming robot*, Winner of the best paper award.

†These results are part of an article in review. Maladen RD, Ding Y, Umbanhowar PB, Kamor A, and Goldman DI, *Mechanical models of sandfish locomotion reveal principles of high performance subsurface sand-swimming*, Journal of the Royal Society Interface

‡This result is a conference article presently in peer review. Maladen RD, Umbanhowar PB, Ding Y, Masse A, and Goldman DI, *Lift control in a sand-swimming robot*, IEEE Conference on Robotics and Automation (2011).

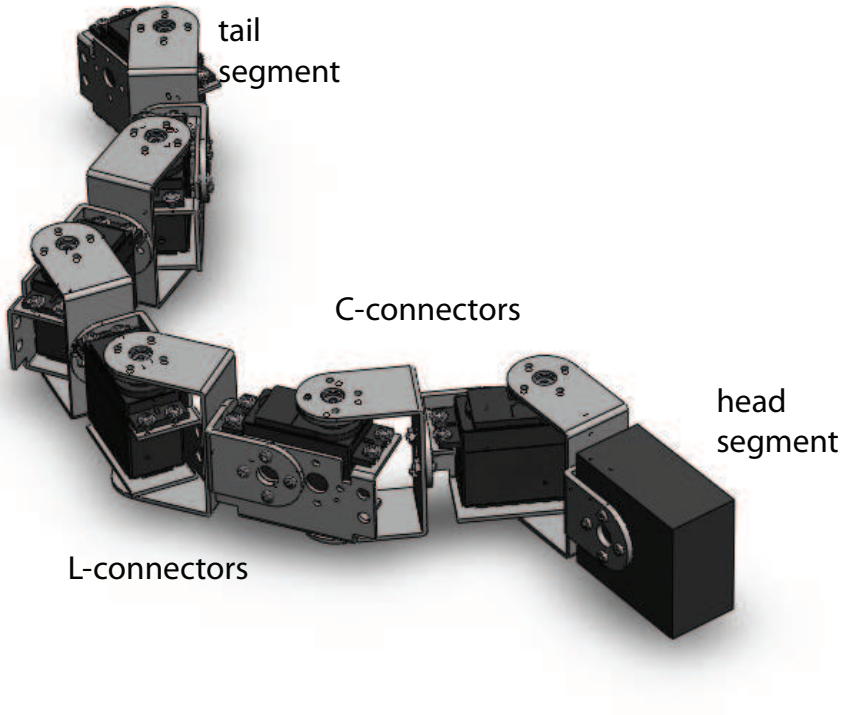

Figure 46: 3D view of the 7 segment sand-swimming robot rendered using SolidWorks. The robot was made up of 6 motors and one passive head segment. Adjacent segments were connected via L- and C- shaped aluminum brackets.

4.1 Design of the sand-swimming robot

The basic mechanical design of our device was adapted from previously developed snake robots [33]. The robot consisted of repeated modules (motors) each with a single joint that permit angular excursions in a plane and were connected via identical links. In our design, each module housed a servomotor attached to an aluminum bracket and connected to adjacent motors via aluminum connectors. For convenience and to maintain a reasonable size, our device employed 6 standard size servomotors and a dummy segment (the head) with the same weight and form factor as the motor segments for a total of 7 segments (see Fig. 46*). For motor specifications see Table 3.)

*Image courtesy of Andrew Masse, under-graduate working in the Goldman group

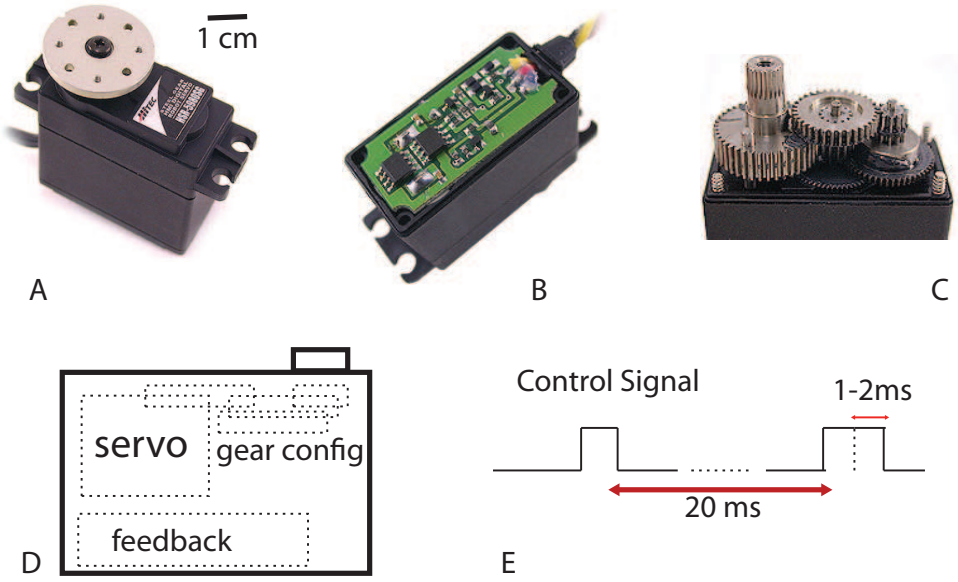

Figure 47: Photographs and schematic of the servomotor, and control signal used for actuating the sand-swimming robot. (A) Hitec 5980SG motor used with images of its (B) internal position feedback circuit, and (C) gear configuration. (D) Side view schematic of the essential components of the servomotor and (E) the control signal whose pulse widths corresponded to the angular position of the motor.

4.1.1 Robot motor selection

For the actuation of the sand-swimming robot technologies like shape memory alloys, piezoelectric devices, magnetostriction devices, etc. were unsuitable due to either the high torque requirement to move within granular media, or the substantial development required beyond the scope of this work. We used commercially available over the counter small electromagnetic DC servomotors similar to those used in most scale models of radio controlled (R/C) planes and cars. These devices are precise, lightweight and cost effective as compared to other comparable DC motors.

R/C servos provide closed-loop position control of angular position. As shown in Fig. 47, the control signal that is sent to a servomotor is a pulse that is repeated every 20 ms. The width of the pulse determines the angular position of the servo. Varying the pulse-width from 1 ms to 2 ms sweeps the angular position of the actuator from one extreme to the other. Typical angular excursions of servos are about 60°, though many servos (including what we used) can mechanically provide 180° of motion.

Dimensions	$0.48 \times 0.028 \times 0.054$ m^3
Mass	0.83 kg
Motor	HSR-5980SG
Motor Torque	2.94 N m
Number of Motors	6
Total Segments	7

Table 3: Physical robot characteristics

Table 4: Parameters of the 6 mm plastic particles used in experiment and simulation

	Experiment	Simulation
Hardness (k)	1.7×10^8 kg s^{-2} m$^{-1/2}$	2×10^5 kg s^{-2} m$^{-1/2}$
Restitution coefficient	0.96	0.95
G_n		5 kg m$^{-1/2}$ s^{-1}
$\mu_{particle-particle}$	0.073	0.080
$\mu_{particle-body}$	0.27	0.27
Density	1.03 ± 0.04 g cm^{-3}	1.03 g cm^{-3}

To reduce the motor torque requirements, we used 6 mm plastic particles (density= 1 g/cm^3) as our granular medium (see Table 4 for details). Since the torque requirements for moving within granular material are very different from moving within fluids or on the surface of a substrate we estimated the drag force subsurface by dragging an object with the same form factor as a standard size servo motor through 6 mm plastic medium at 0.25 m/s. The measured force at a depth of 4 cm was 3.2 N. Since the maximum torque would occur at the middle motor (0.23 m to either end) we estimated that the maximum possible total force along an effective segment extending from the middle servo to either the tail or the head (length 0.23 m) was 18 N with a corresponding maximum torque of 2.0 Nm. We selected a servomotor (see Fig. 47 a) whose torque ratings exceeded these torque estimates, the details of which are summarized in Table 3.

As per our design we assembled the motor to form the 7 segment robot. The wire bundle that routed the power and control signals to each motor was run atop each module over the length of the device and strain relieved at the last (tail) segment (see Fig. 48).

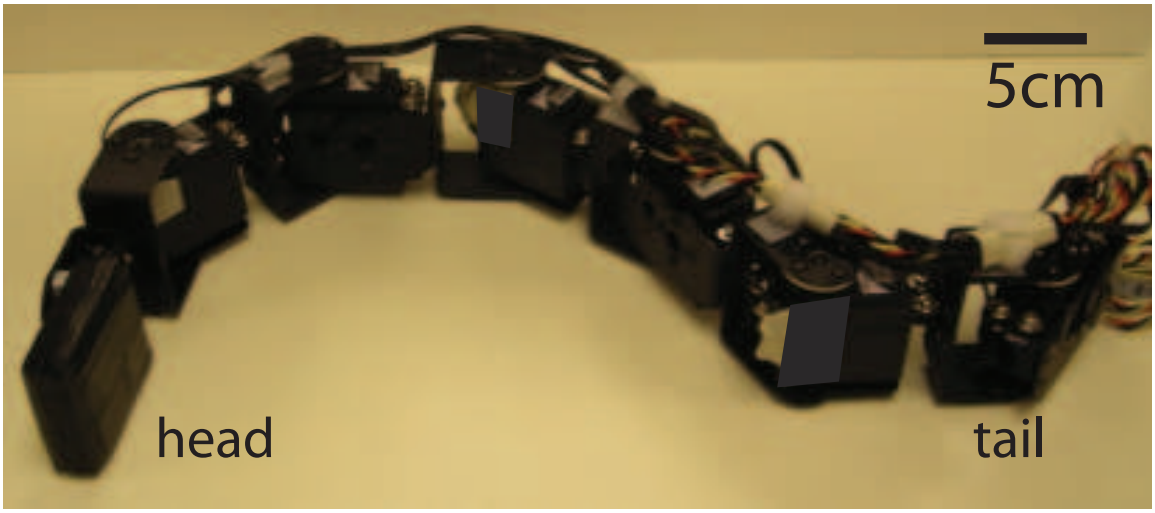

Figure 48: Photograph of the sand-swimming robot without its casing (skin). The photograph shows the 6 servomotors and the passive head segment that form the robot connected via aluminum brackets with the power and control signal wires running along the top of the device.

4.1.2 Robot casing (skin)

To prevent particles from intruding between motor segments and jamming the device as it undulated (see 48), we encased the robot in a double-layer skin. A low friction LYCRA spandex sleeve with a single seam (located at the top of the device) was slid over a snugly fitting elastic latex sleeve that prevented particles from getting between the motors during phases of the motion when the LYCRA sleeve was loose. The outer layer reduced the wear on the thin inner layer, allowing for > 100 subsurface trials without replacement of the inner layer. The robot was tested on average with a $4-5$ minutes rest between consecutive runs to avoid melting the inner later layer due to excessive motor heat. The control and power wire bundle was run along the top of the motors under the inner latex sleeve (see Fig. 49).

4.1.3 Robot electronics

The servomotors were powered in parallel from a 7.4 V, 30 A supply. The pulse width based control signal used to modulate the angle between adjacent motors was generated in LabVIEW. Initial testing of the robot revealed that the kinematics prescribed by the sinusoidal traveling wave (see Eqn. 3) were accurate only for low amplitudes. For larger

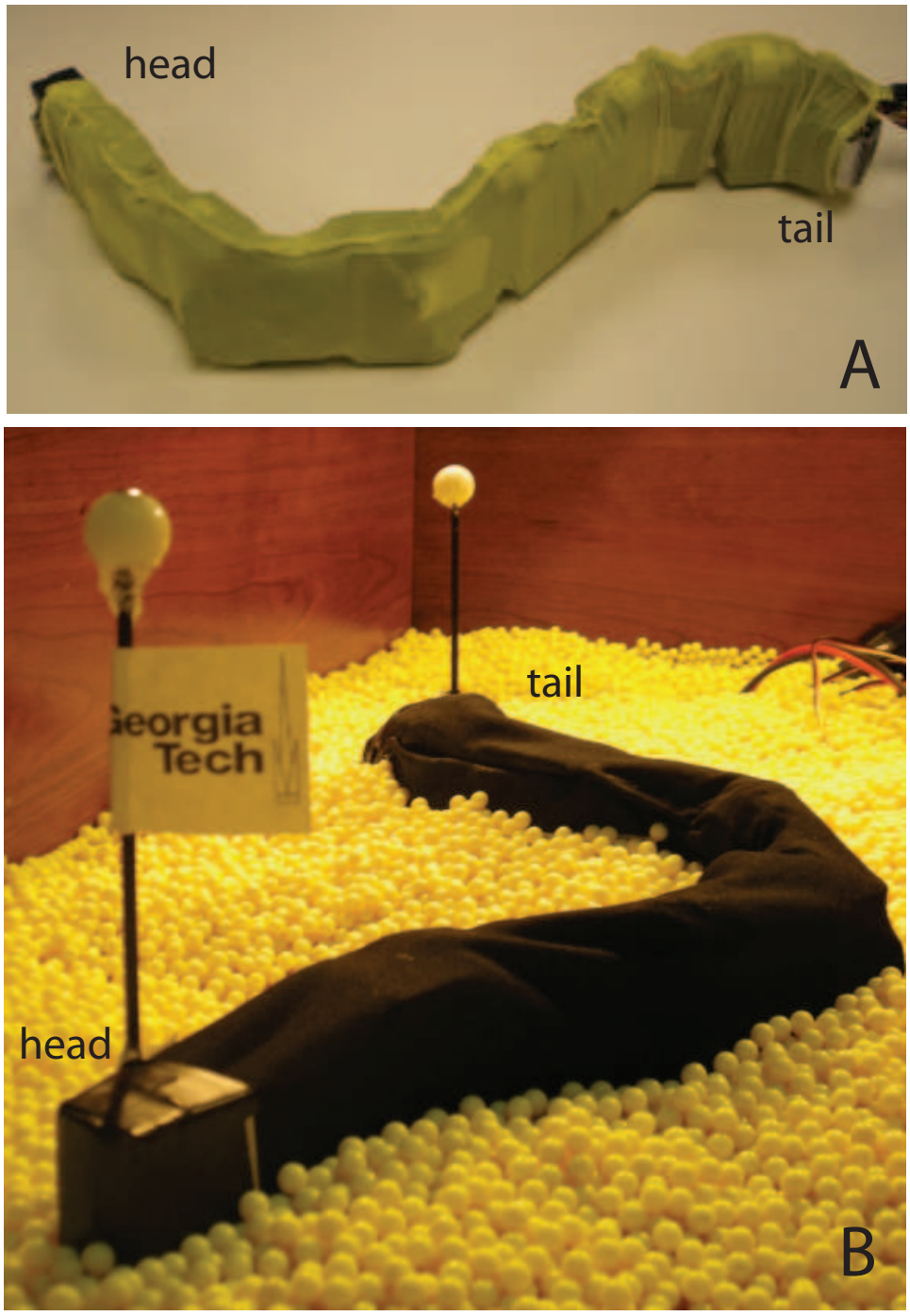

Figure 49: Photographs of the sand-swimming robot with its inner and outer casing (skin). The robot had a double layered skin: (A) tight fitting ultra thin latex inner layer, and (B) Lycra spandex outer layer. The balls on narrows masts on the head and tail segments allowed for subsurface motion tracking.

amplitudes due to the segment length associated with a finite number of segments (total length divided into 7 segments) the angles that the motor were required to achieve to maintain the sinusoidal traveling wave trajectory exceeded the mechanical excursion limits of the motor. To obtain a larger range of amplitudes we implemented an open loop controller which constrained the angle between adjacent segments using

$$\beta(i,t) = \beta_0 \xi \sin(2\pi\xi i/N - 2\pi f t), \tag{5}$$

where $\beta(i,t)$ is the motor angle of the i^{th} motor at time t, β_0 is the angular amplitude, ξ is the number of wavelengths along the body (period), and N is the number of motors.

The angular position of each motor of the sand-swimming robot was controlled with pulses of varying width that were generated in LabVIEW. Since each motor required a pulse every 20 ms and the maximum width of a pulse was 2 ms, we generated pulses for the 5 other motors in the interim period between two consecutive pulses to a motor (shown in Fig. 50). The multiplexed signal containing appropriate pulse widths for all the 6 motors was output from an analog output on a PCI-card (NI-6230). The signal was routed to the clock input of a decade counter (CD4017BC) which functioned as a demultiplexer and distributed a control signal pulse to each motor every 20 ms. Fig. 51 has a detailed schematic of the circuit used to condition the control signal generated by LabVIEW before it was routed to the motors.

Component	Specifications
IC1	CD4017 Decade Counter/Divider
IC2 and IC3	LM324 Quad general purpose amplifier
Resistance (R)	1 kohms
Capacitance (C)	$0.1\,\mu F$
Zener diode (D)	
Motors (M_i)	Control signal to the i^{th} motor
Voltage (V_{cc})	7.4 Vdc
AO	Analog Output from LabVIEW

Table 5: Components of the circuit used to condition the servomotor control signal.

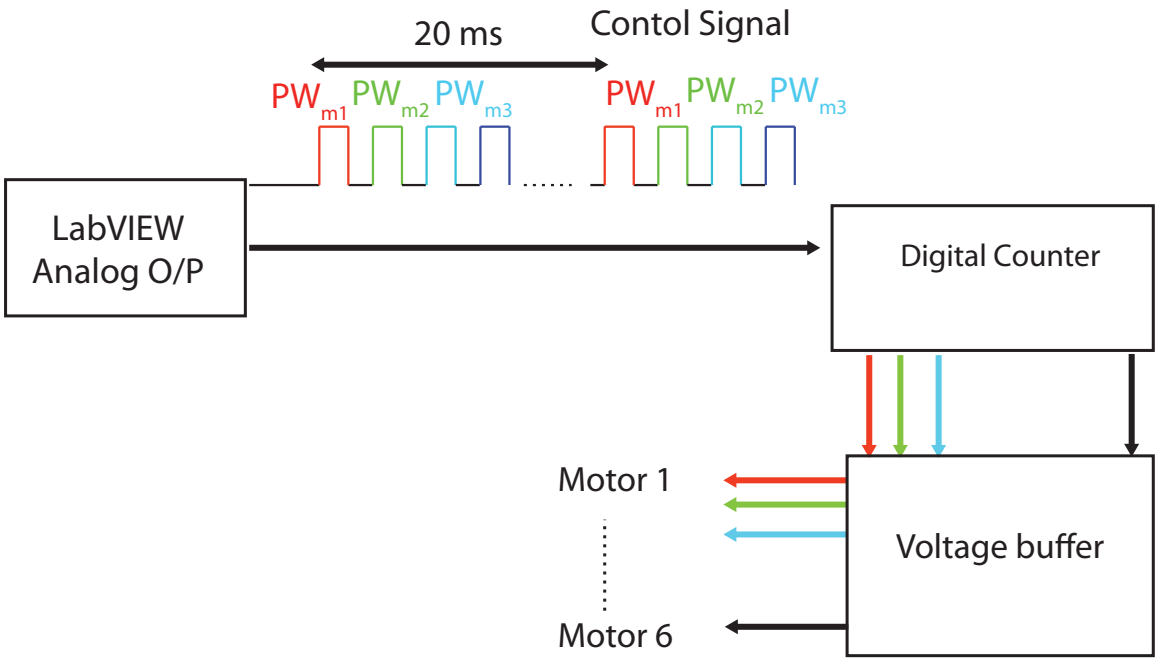

Figure 50: Schematic for the generation and conditioning of the servomotor control signal. For details see Section 4.1.3

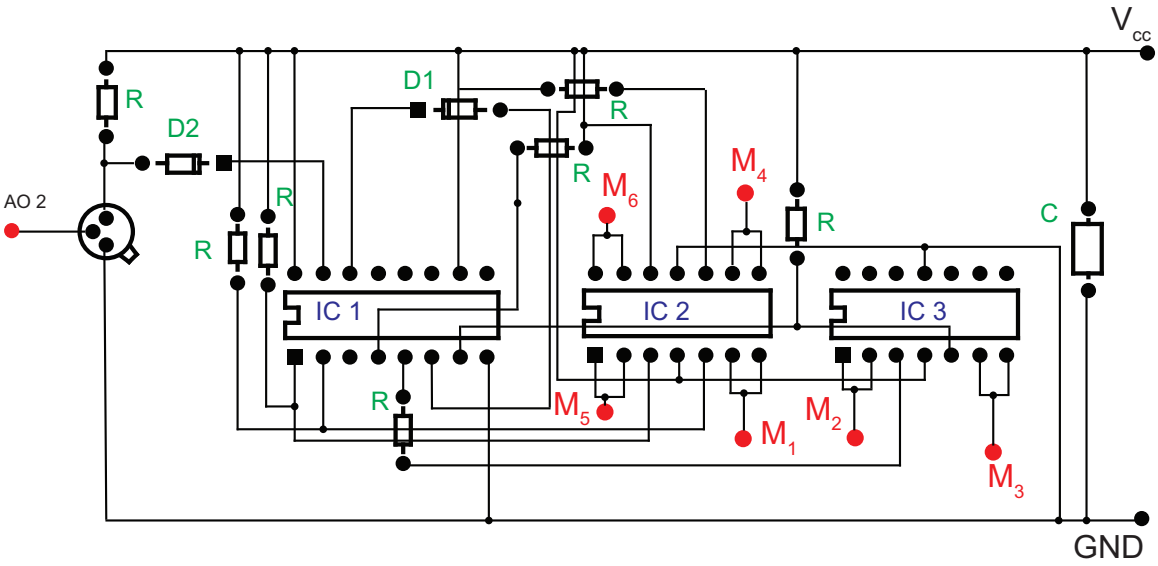

Figure 51: Schematic of the circuit used to condition the servomotor control signal. For detailed specification of the components and labels see Table 5

4.2 Experimental methods

The granular medium in which the robot was tested was composed of approximately 350,000 plastic particles with diameter 6 mm and density 1 g/cm^3. The 23 particle deep bed of

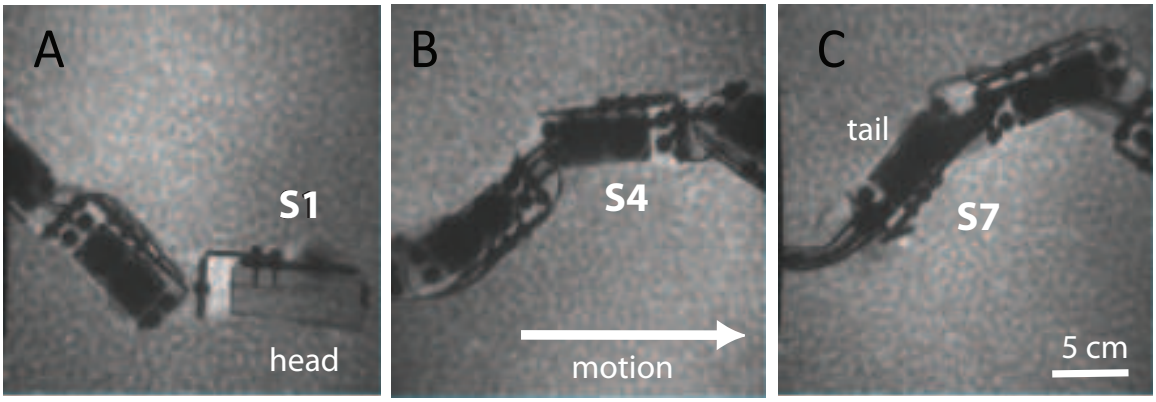

Figure 52: X-ray imaging of the subsurface kinematics of the sand-swimming robot. (A-C) Sequential x-ray images of the robot as it swims in 6 mm plastic particles. Segments from head to tail are denoted as S1 to S7.

particles was held in a 180×67 particle diameter container. The particles were mixed by hand to prevent them from crystallizing and prepared into an as-poured state [91] with a volume fraction of 0.62 ± 0.01. Overhead video (100 fps) was collected for each condition tested. To facilitate subsurface tracking the first and last module were fixed with a mast with a visible marker. For each test the top of the robot was submerged 4 cm below the surface and the surface leveled. Due to the servomotor velocity limits the maximum oscillation frequency tested was 1 Hz. For each frequency, $1 - 2$ cycles of motion were collected.

We experimentally verified that the motors were able to achieve the prescribed joint excursions by using x-ray imaging to study the kinematics of the robot subsurface. We obtained x-ray images for a representative condition ($f = 0.25$ Hz, $A/\lambda = 0.2$), see Fig. 52.

4.3 Results

4.3.1 Temporal characteristics of the physical robot

To calibrate the device we placed it on a rigid surface and used video to track the position of the segments from which we determined the mapping between the maximum relative segment angle β_0 (Eqn. 5) and A/λ. Within the granular material, the forward velocity of the device monotonically increased with increasing oscillation frequency (Fig. 53) for a single period wave with $A/\lambda = 0.2$. The slope of this relationship (η) was 0.34 ± 0.02. We also found that the robot progressed with nearly the same wave efficiency ($\eta = 0.35$) within

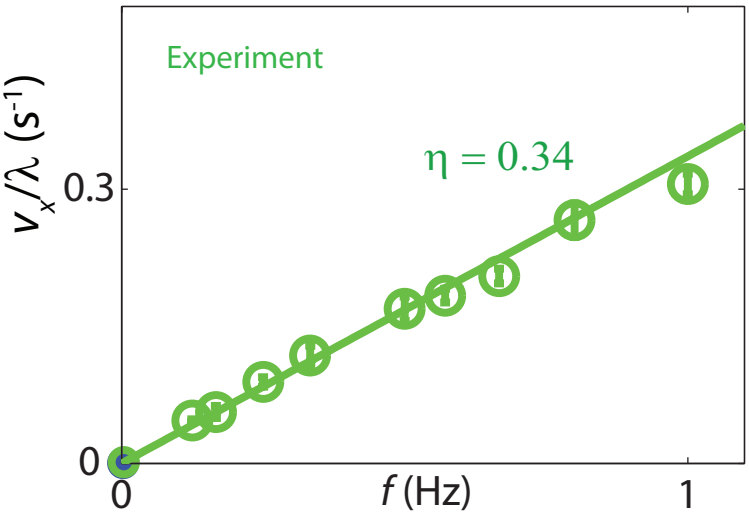

Figure 53: The forward velocity of the physical robot as it swims within granular media with different oscillation frequencies (green circles) ($A/\lambda = 0.2$, single period wave). The slope of the solid green fit line gives wave efficiency $\eta = 0.34$. 3 runs were collected for each frequency tested.

poppy seeds. η predicted within poppy seeds and 6 mm plastic particles are nearly the same because for both media μ_{bp} and μ_{pp} (which determine η, see Section 3.5 for details) both increase and decrease, respectively resulting in no effect on subsurface performance.

Like the sandfish lizard, the RFT, and numerical simulation, the forward velocity of the robot monotonically increased with frequency (Fig. 53) for $A/\lambda = 0.2$ and a single period wave. However, η was 0.34 ± 0.02, significantly below that measured for the animal in experiment and predicted by the RFT and animal simulation.

We speculated that the η of the robot was less than that of the sandfish (in biological experiment, RFT, and numerical simulation) because the finite number of segments did not allow the robot to achieve a smooth sinusoidal profile. To investigate segment number effects, rather than increasing the number of motors (which would be challenging experimentally as doing so would require an increased numbers of smaller motors with high torque requirements to maintain the same fixed length as the 7 segment robot) we adapted the numerical sandfish simulation (Chapter III) into a numerical robot simulation that matched the physical device and granular medium in physical dimension, mass, and density.

4.4 Numerical robot simulation

To develop a numerical simulation of a sand-swimming robot, we adapted our numerical simulation of the 12 cm long sandfish (described in Chapter III, Section 3.2) to the same size scale as the physical robot with a finite number of discrete, rigid segments and tested if it could swim within a validated model of the same granular medium as used in robot experiment.

4.4.1 Simulating and validating the granular medium

The robot simulation coupled a numerical model of the robot to a model of the granular medium. We simulated the granular material using the same 3D soft sphere Discrete Element Methods techniques [101] discussed in Chapter III, Section 3.1. The robot-particle and particle-particle interaction forces were calculated at each contact using Eqn. 2.

We simulated the same particles as used in the robot experiment (6 mm plastic particles) which helped decrease the computational time. The dimensions of the simulated test container were also kept same as experiment. To validate the simulated medium and obtain the values of friction μ_{pp}, hardness k, and viscoelastic constant G_n (see Table 4), we dropped an aluminum ball (diameter 6.35 cm and mass 385 g) into the plastic particles with varying impact velocity ($0.5-3$ m/s) in both experiment and simulation and set grain interaction parameters to best match the measured and simulated penetration force during the impact collision as a function of time (Fig. 54) [43] *. With parameters determined from impact at $v = 1.4$ m/s, the force profile fit well at other impact velocities. In additional experiments, we directly measured μ_{pp} and the coefficient of restitution (calculated from fitted k and G_n) for the plastic particles and found them to be within 5% and 10% of the fitted values respectively.

4.4.2 Simulating the robot

To model the sand-swimming device we used the same commercial multi-body simulator software package Working Model 2D (Design Simulation Technologies) which was used to

*Experimental data courtesy of Mateo Garcia, under-graduate working in the Goldman group

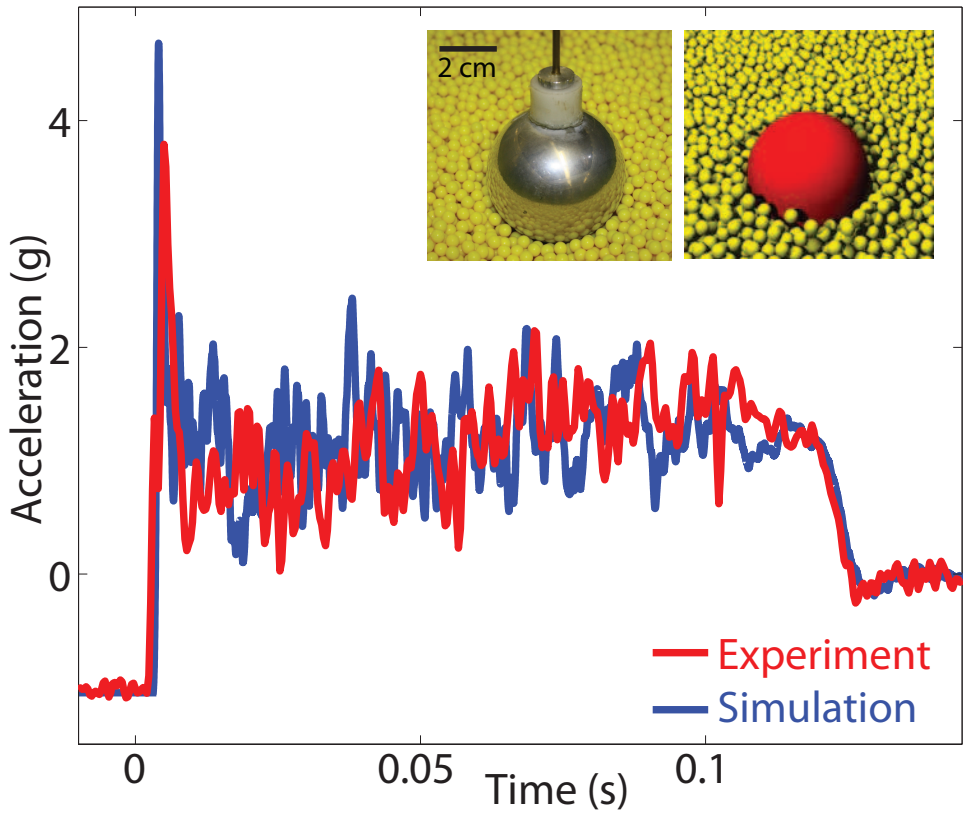

Figure 54: Validation of the 3D Discrete Element Method simulation for the granular medium (6 mm plastic particles) using measured acceleration of a sphere during impact after free-fall. Acceleration vs. time in simulation (blue) and experiment (red) agree well. The impact velocity for this representative run is 1.4 m/s. Acceleration is given in units of g, the acceleration due to gravity. (Left inset) Aluminum ball instrumented with accelerometer resting on 6 mm plastic particles. (Right inset) Ball and particles in simulation.

simulate the sandfish in Chapter III, Section 3.2. Modeling the device in a 2D simulation environment was sufficient to capture the dynamics since the sand-swimming robot moved roughly in a horizontal plane at fixed depth in this study. The simulated robot had the same dimensions as the corresponding physical device. Since the sandfish did not use its limbs to move subsurface and the physical robot had shown that body undulations were sufficient for propulsion [82], the simulated robot did not include limbs. The simulated robot consisted of 49 cuboid segments interconnected and actuated by virtual motors (vertical cylinders) of the same height (Fig. 55). Depending on the number of segments (N) to be employed, every $48/N$ motor was driven with an open loop signal to generate a sinusoidal wave traveling posteriorly from head to tail while the remaining motors were immobilized to form a straight segment of length 48 / N cm. The angle between adjacent segments was constrained using Eqn. 5

The multi-body simulator integrated the equations of motion of the coupled links and the DEM calculated the resultant force from both the particle-particle and body-particle interactions. For each time step, the net force from particles on each segment was passed to multi-body simulator, and velocity and position information transferred back to DEM. Rotation about the axis of the traveling wave (roll and pitch) was not modeled.

4.4.3 Temporal characteristics of the simulated robot

The simulated 7 segment robot moved forward within 6 mm plastic particles (see Fig. 56).

The temporal characteristic of the simulated robot quantitatively matched the robot experimental results (Fig. 57). The forward speed of the robot increased linearly with oscillation frequency. The wave efficiency was $\eta = 0.36 \pm 0.02$, less than that of the sandfish lizard.

4.4.4 Effect of number of segments on robot performance

Increasing N (for a fixed length device) in the robot simulation caused the robot to advance more rapidly and with greater wave efficiency until $N \approx 15$ above which η remained constant at 0.54 (approximately that of the animal) (Fig. 58). The biological sandfish (independent of particle size and media preparation) (see Chapter II), the numerical sandfish in 3 mm

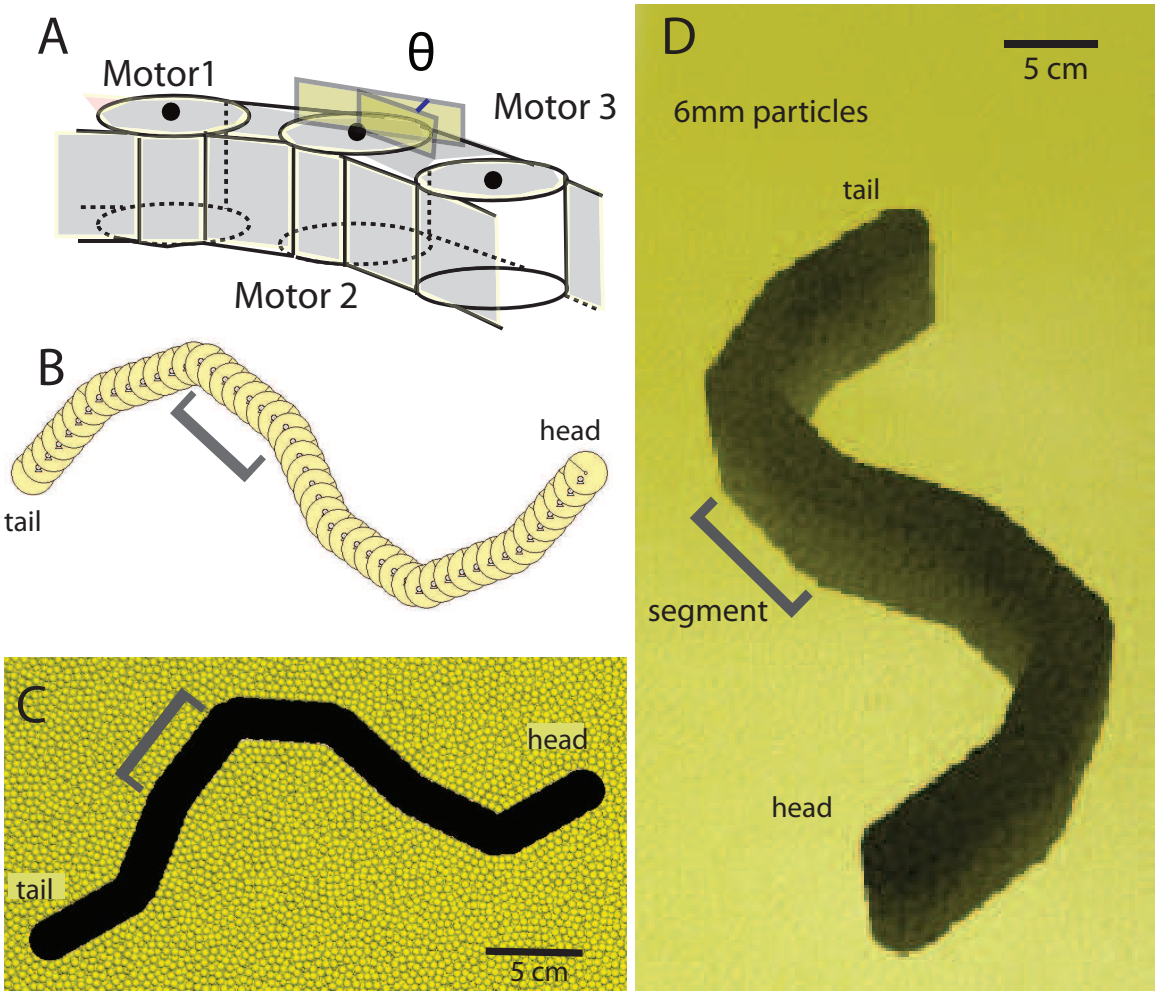

Figure 55: Design of the simulated sand-swimming robot. (A, B) Side and top view of the robot modeled with 49 inter-connected motor segments and one head segment. The angle between adjacent motors (β_i) was modulated using Eqn. 5 to reproduce sinusoidal traveling wave kinematics along the body of the simulated 7 segment robot. (C) Top view of the device submerged in 6 mm particles with the particles above the robot rendered transparent. (D) 3D rendering of the simulated sand-swimming robot in 6 mm plastic particles. The particles have been rendered semi-transparent for visualization. The gray brackets ([ ) indicate a single robot segment.

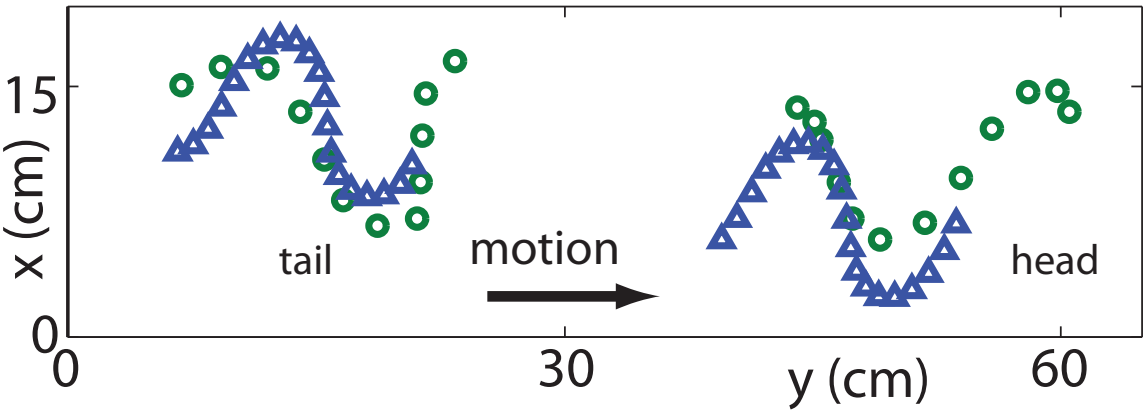

Figure 56: Position of the head and tail segments of the physical (green circles) (determined by tracking the corresponding masts) and simulated (blue triangles) robot as it swims within 6 mm plastic particles.

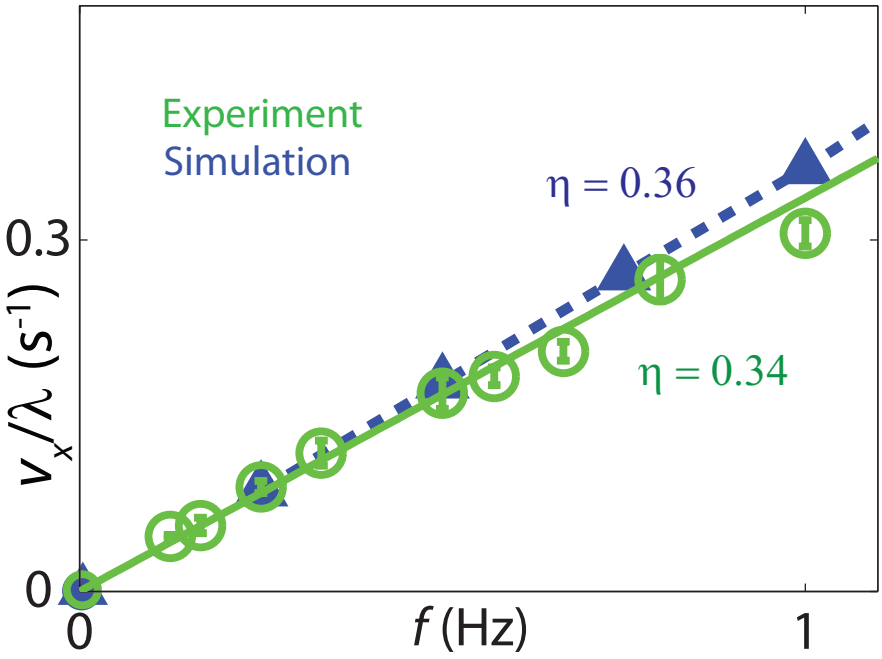

Figure 57: Forward velocity vs. oscillation frequency relationship for the robot in experiment (green circles) and simulation (blue triangles) ($A/\lambda = 0.2$ and $\xi = 1$). The slope of the dashed (simulation) and solid (experiment) fit lines gives wave efficiency η of 0.36 and 0.34, respectively.

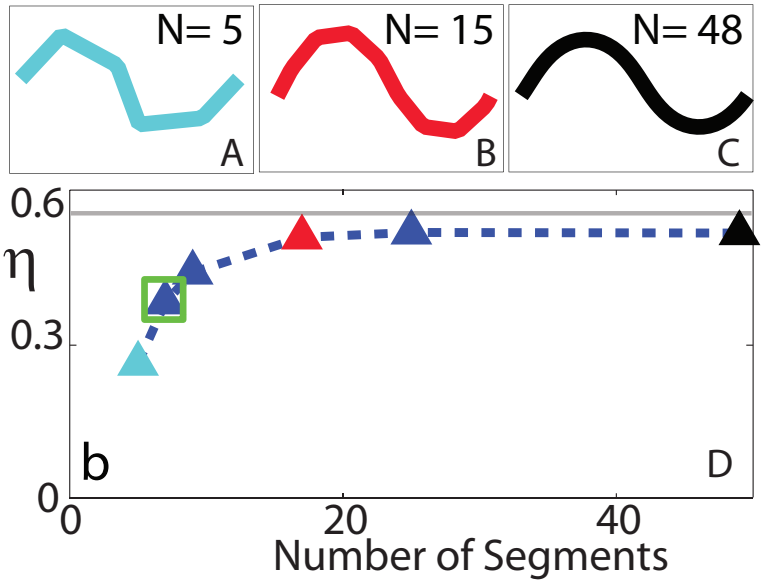

Figure 58: Effect of number of segments on the wave efficiency η for a fixed length robot in simulation (blue dashed curve)($f = 1$ Hz and $A/\lambda = 0.2$). The red, black, and cyan triangles correspond to 5 (A), 15 (B), and 48 (C) segment robots respectively. The green square corresponds to the number of segments used in the physical robot, and the gray line indicates η predicted by the RFT solved for a continuous body profile (see [80] for details).

particles (Chapter III), and robot simulation in 6 mm particles, all predicted wave efficiency η of close to 0.5 which suggests that subsurface locomotion in granular media is largely independent of media properties like particle size, density, and friction.

We postulated that the increase in η with increasing N was due to a smoother body profile which facilitated media flow and led to decreased drag and/or a decreased variation in the spatial form (A/λ) from the prescribed sinusoidal target (as much as 30% for $A/\lambda = 0.2$ for $N = 7$, measured using video of the robot undulating on a flat surface). This result suggests that near maximal performance occurs when the spatial form of the robot reproduces a sinusoidal traveling wave with minimal deviation.

4.5 Spatial characteristics of the physical and simulated sand-swimming robot

In Chapter III, we showed that the numerical sandfish simulation predicted the spatial form that maximized the forward speed of a sand swimmer corresponded to the parameters used by rapidly escaping sandfish, i.e. a sinusoidal traveling wave with fixed kinematics ($A/\lambda = 0.2$ and $\xi = 1$). We used both the physical and simulated robot to test the validity

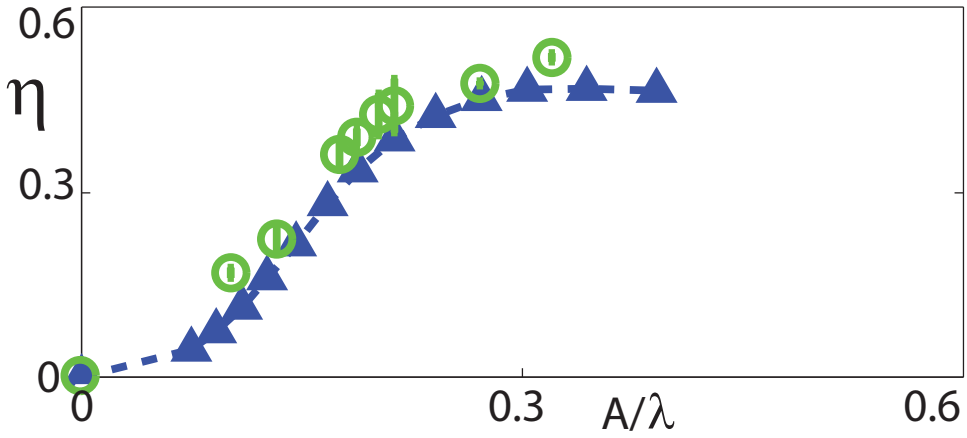

Figure 59: Effect of varying A/λ on the wave efficiency η of the physical (green circles) and simulated (blue triangles) robot ($\xi = 1$ and $f = 0.5$ Hz) as it swims within 6 mm particles.

of the prediction in a real world environment.

4.5.1 Testing for the kinematic conditions that maximize sand-swimming speed

We systematically varied A/λ for $f = 0.5$ Hz and measured the wave efficiency of the robot as it swam subsurface. For all A/λ tested, there was good agreement between η measured in experiment and in the numerical robot simulation. Although η corresponding to an $A/\lambda = 0.2$ was lower than what was measured in the biological experiment, numerical sandfish simulation, and RFT (reason explained in previous section), the shape of the η vs. A/λ relationship remained qualitatively the same. The shape of this relationship has been discussed in Chapter III, Section 3.4.

The numerical sandfish simulation predicts that the animal can increase η by increasing A/λ (see Fig. 40), but we find that the animal does not operate at high A/λ. Maladen et al. [82] showed using the RFT predictions (qualitatively the same as the animal simulation) that operating at large A/λ (Fig. 43) comes at a cost; since the animal is of finite length, the distance it travels per cycle decreases with increasing A/λ. We can see this by expressing body-lengths traveled per cycle as $v_x/fL = \eta\lambda/L$ using $v_x = \eta f\lambda$. While η increases with increasing A/λ, λ decreases and thus a maximum in forward progress per cycle can be expected.

Fig. 60 shows that as predicted by the numerical sandfish simulation (see Fig 43) the

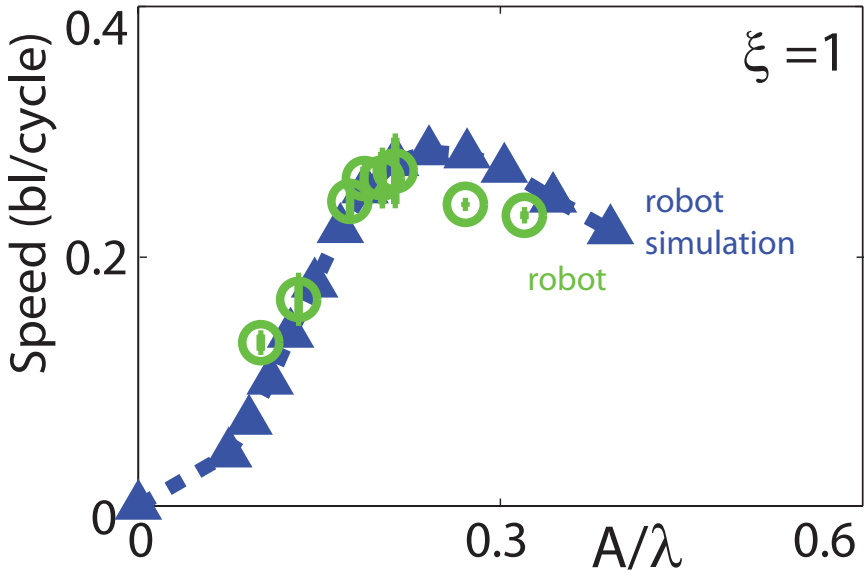

Figure 60: Effect of varying A/λ on the swimming speed of the physical and simulated robot. Forward speed for the robot in experiment (green circles) and simulation (dashed blue curve with triangles) corresponding to varying A/λ (with $\xi = 1$ and $f = 0.5$ Hz). Fitting the robot simulation curve with a third order polynomial identified the maximum speed $= 0.28 \pm 0.01$ bl/cycle at $A/\lambda = 0.24 \pm 0.01$.

physical and simulated robot displayed a maximum forward progress per cycle at $A/\lambda \approx 0.2$. The biological data resides at the peak of the curve, indicating that the animal was maximizing its sand-swimming speed, which agrees with the hypothesis that sandfish burial is an escape response [7].

To test the effect of number of wave periods on performance, we fixed $A/\lambda = 0.2$ and varied $0.6 < \xi < 1.6$. We found that the physical and simulated robot progressed forward fastest for approximately a single period along its body (Fig. 61).

We can understand the dependence of speed on ξ. For non-integer ξ the robot experiences an unbalanced torque that results in a periodic yawing motion which causes A to become effectively smaller and which results in lower η and lower v_x. For $\xi > 1$, decreased v_x results from a lower η due to the decrease in A required to keep A/λ fixed. Testing was possible over only a limited range for the physical robot because for $\xi < 0.6$ the side walls of the test container interfere with the motion due to the large amplitude of undulation of the robot, and for $\xi > 1.3$ the maximum angle required to maintain $A/\lambda = 0.2$ exceeds the

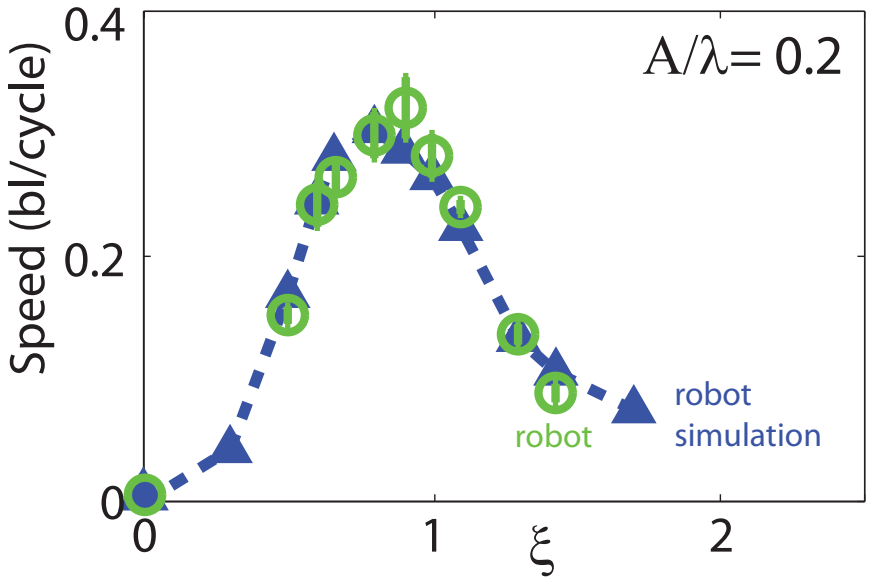

Figure 61: Effect of varying ξ on the swimming speed of the physical (green circles) and simulated (dashed blue curve with triangles) robot ($A/\lambda = 0.2$) as it swims within 6 mm particles.

range of motion of the servomotors.

4.6 Summary

In the previous sections of this chapter, inspired by biological experiments that revealed the rapid sand-swimming ability of the sandfish lizard, we built an undulatory sand-swimming robot with a finite number of segments (7) that can advance within granular media using a open loop (traveling wave sinusoid) control scheme. We then developed a numerical robot simulation to provide a potential explanation why the performance of the physical device was lower than the animal (by nearly 30%). We used both the physical and simulated robot to validate the biological observations and predictions from the RFT [82] and numerical sandfish simulations (Chapter III) that body undulations were sufficient to propel the robot forward. The robot (both physical and simulated) also agreed with the RFT and sandfish simulation prediction that the kinematics that maximized their forward speed were the same as those used by the animal ($A/\lambda = 0.2$ and $\xi = 1$).

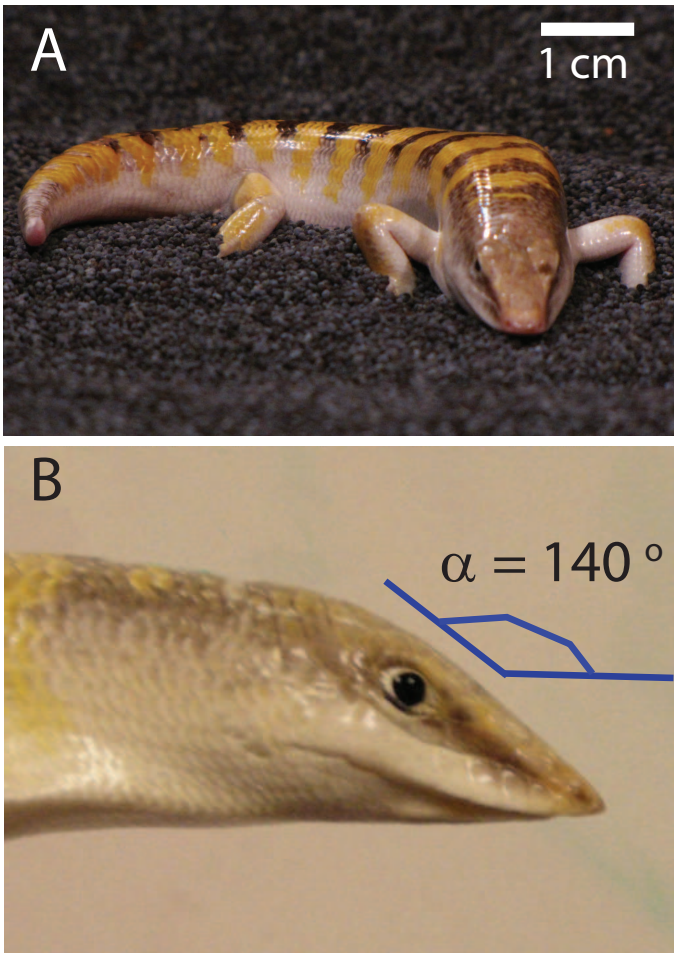

Figure 62: (A) Front and (B) sagittal view of the sandfish head shape. α indicates the angle of the leading surface of the sandfish snout with the horizontal.

4.7 Lift control for the sand-swimming robot

Specific morphological adaptations like having a shovel shaped head, reduced limbs, and an elongate body have been hypothesized to aid the sand-swimming ability of desert dwelling lizards like the sandfish (for details see Chapter I, Section 1.2.2). The work presented in this section was inspired by the head shape of the sandfish lizard (Fig. 62). Guided by object drag experiments we demonstrate that the lift forces in granular media depend on the intruder shape and then study the effect of these shapes on the vertical trajectory of the robot. To overcome the inconvenience of varying the shape of the robot head to vary lift, we also test head shapes that approximate one head tilted at various angles to modulate lift as the robot undulates within granular media.

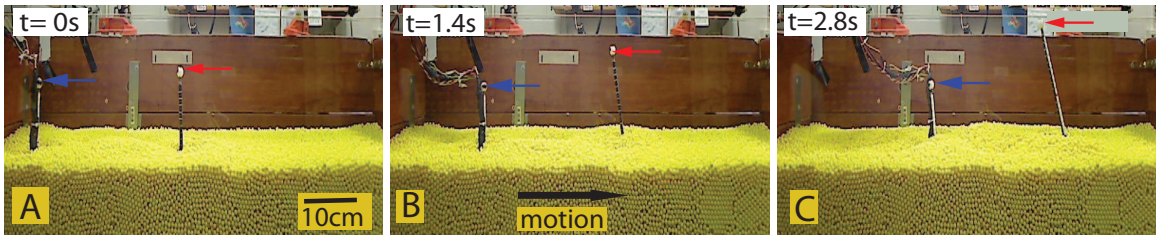

Figure 63: Sagittal view of the robot swimming in granular media that shows it rises as it progresses forward. (A-C) The square block head robot [80] swimming subsurface within 6 mm plastic particles. The red and blue arrows indicate the position of the mast at the head and tail segments of the robot.

Our previous study [80] found that the robot (with a square block head) rises to the surface of the media as it progressed forward within $2-3$ cycles of motion (Fig. 63). To ensure that this phenomenon was not an artifact of a torque imbalance resulting from the wires tethered to the robot tail mast, we reversed the direction of the traveling wave along the robot such that the tail became the head and found that it continued to rise at the head (first segment in the direction of motion). Hydrostatic buoyancy was also disregarded as an explanation as the robot experienced no lift unless it was dragged or moved, and the ratio of the density of the robot to the plastic particles, $1.16:1$, was greater than one. Also, the observed surfacing behavior was different from the Brazil nut effect [103] in which lift results from agitation of the medium by shaking the container.

4.7.1 Robot kinematic control: traveling vs. standing wave

To investigate whether the lateral or forward motion of the robot as it undulated produced the observed lift, we tested the robot with standing wave kinematics given as

$$\beta(i,t) = \beta_0 \xi \sin(2\pi f t)\sin(2\pi \xi i/N). \tag{6}$$

As expected, the robot did not progress forward due to the symmetry of its undulatory motion. Contrary to the observations for the traveling wave kinematics, the robot did not rise (Fig. 64). This indicated that forward motion was necessary for the robot to rise and motivated us further to investigate the effect of head shape on the vertical motion of the robot.

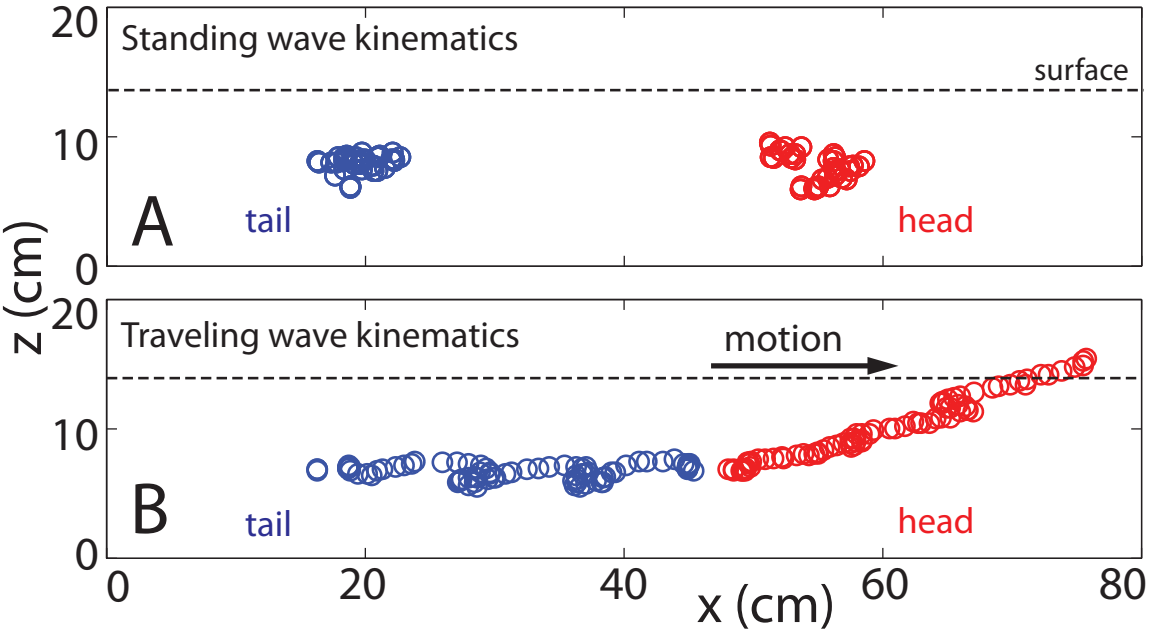

Figure 64: Effect of varying robot kinematic control: traveling vs. standing wave. (A) The square block head robot [80] (A) does not rise or advance with standing wave kinematics but (B) does rise and advance with traveling wave kinematics. The red and blue symbols correspond to the tracked position of the robot head and tail respectively as it swims subsurface. The dashed line indicates the surface.

4.7.2 Drag induced lift in granular media

Experiments on slow horizontal and vertical drag [2, 44] of objects within granular media have provided some understanding of the observed drag forces, but few have investigated the associated lift forces. Studies have examined the scaling of the lift force with intruder depth and width for a partially submerged vertical rod moving horizontally and for a rotating plate [120, 113], the drag force on submerged objects with curved surfaces [2], and, only recently, the lift forces acting on horizontally translated submerged objects [30].

We tested our hypothesis that an object dragged through granular media would generate shape dependent lift force. Inspired by the head shape of the sandfish lizard (Fig. 62), we confined our testing to wedge shaped objects (Fig. 65 A). These objects (Group I) have the normal of their bottom face perpendicular to the direction of motion through the medium and the angle of the upper surface of the wedge is varied, while keeping the height, and projected front and lateral areas fixed. Only the length of the longest dimension (flat base)

varied with the wedge angle (α). The maximum and minimum α tested was limited to the maximum head size that would not interfere with the sides of the container as the robot undulated. The weight of each object was matched to the weight of the block robot head (110 g).

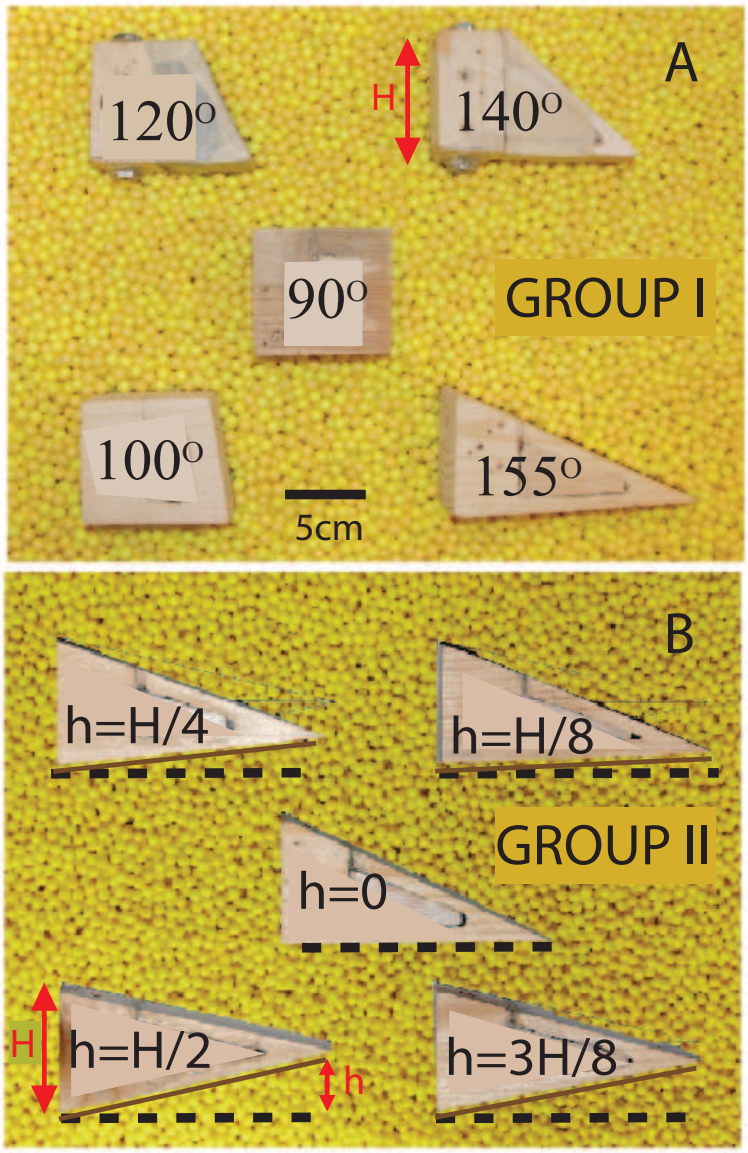

Figure 65: Top view of head shapes tested in both the physics drag and robot experiments resting on 6 mm plastic particles. All objects have fixed height ($H = 5$ cm) and transverse projected area = 27.5 cm^2. (A) Group I: objects with fixed lateral projected area for various wedge angles α. Each object reflected horizontally corresponds to objects with $\alpha = 180°$ minus the labeled α. (B) Group II: objects with fixed length (11 cm) with vertical position of the leading edge varying as a function of $H = 5$ cm. See text for detailed description of objects.

Each wedge was dragged through a container ($40 \times 30 \times 24\,\mathrm{cm}^3$) filled with the same 6 mm plastic particles used in the robot experiment. Since forces are independent of speed in granular media in the range of interest (drag force changes by less than 10% for speed between 0 and 40 cm/s in 0.3 mm glass particles [82]) drag tests in experiment were performed at a constant speed of 5 cm/s with the object's vertical mid-point at depth d = 6.5 cm and its long axis parallel to the motion direction (see Fig. 66). The object was attached to a robotic arm (CRS Robotics) via a thin but stiff supporting rod which moved the intruder at constant depth and velocity while a 6 d.o.f. force sensor (ATI industrial) mounted to the robotic arm measured the drag and lift force. Force on the supporting rod was measured separately and subtracted to obtain the force on the object alone. The test was repeated three times for each object and the average values are reported.

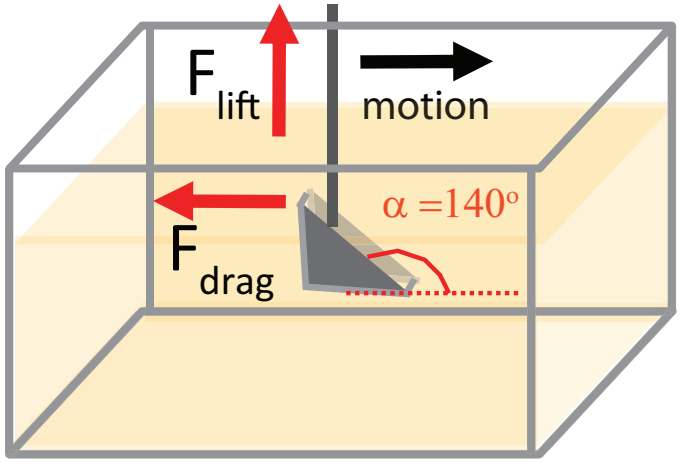

Figure 66: Schematic of the experimental setup used to measure lift and drag forces on objects dragged through the granular medium. The objects shown in Fig. 65 A were attached to the connecting rod, submerged to a depth of 6.5 cm from the object center and dragged through the 6 mm plastic particles at 5 cm/s. For each run the lift and drag forces on the object were measured.

We found that the lift force corresponding to the block square head ($\alpha = 90°$) was positive, indicating that if vertically unconstrained the object would rise to the surface as it progressed forward, which agreed with our observations for the robot (Fig. 63). Interestingly, for $\alpha < 80°$ the object experienced a positive lift and for $\alpha > 120°$ a negative lift, while for $80° < \alpha < 120°$ it experienced no lift (Fig. 67).

To gain an understanding of the lift forces, we dragged in simulation three representative

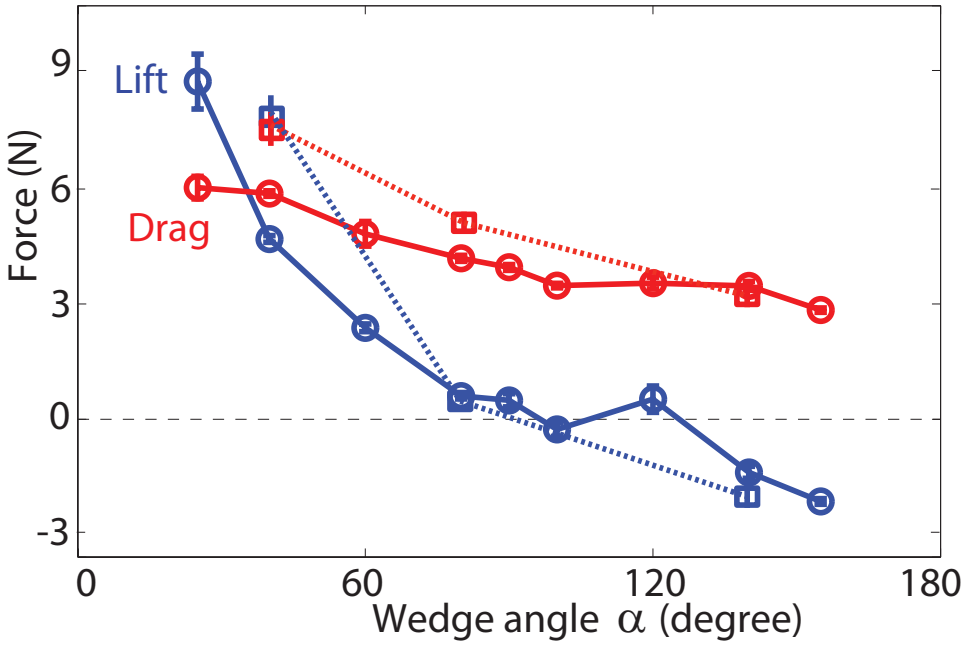

Figure 67: Measured lift (blue) and drag (red) force on wedge shaped objects (Group I, see Fig. 65 A) ($25° <$ wedge angle (α) $< 155°$) translated at a depth (top of object to surface) of 4 cm through 6 mm plastic particles. The circle (solid lines) and square (dashed lines) symbols correspond to the experimental and simulated forces.

shapes in experimentally validated 6 mm particles (same as used in drag experiment). The simulation predicted average drag and lift forces to within 10% over the range of wedge angles studied. As in [30], we found the drag and lift on these intruders resulted mainly from the force on the leading surface of the object as forces on surfaces parallel to the motion of direction were small (Fig. 68). The normal force was relatively larger than the tangential force (the frictional force). The positive lift corresponds to objects with $\alpha < 90°$ and negative lift corresponds to $\alpha > 90°$. However, the magnitudes of the drag and lift forces were larger for $\alpha < 90°$ because the inclined surface pushes the media downward where the yield stress is larger. The increase of yield stress with depth in granular media also makes the flow asymmetric such that for all shapes tested most particles in front of the intruder move upward. For the square shape this upward flow generates a small lift via the friction force on the leading surface. For further details on the physics of the granular drag, refer to [30].

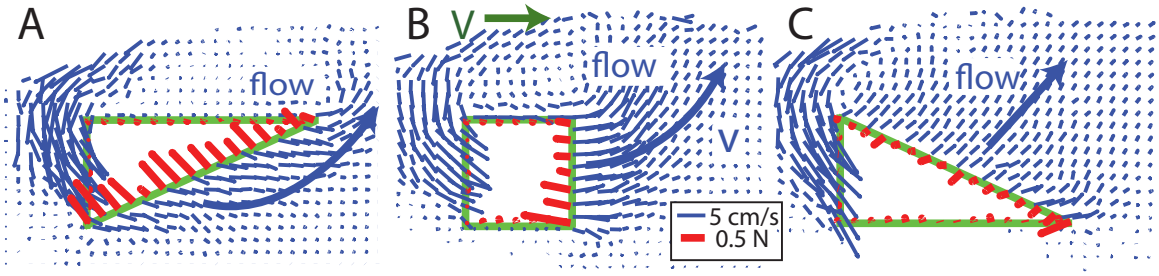

Figure 68: Numerical simulation of objects dragged through experimentally validated 6 mm plastic particles. (A), (B), and (C) correspond to $\alpha = 40°$, 90°, and 140° respectively. Red and blue lines denote the magnitude and direction of force on the surface of the objects and the velocity of the particles respectively. The thick blue arrows indicate the average direction of flow. Velocity is averaged over 0.8 cm×0.8 cm cells along the thickness of the plate (into the page) and 2 time instants separated horizontally by 0.05 cm. The force is similarly averaged except the volume is replaced by a area on the surface of the intruder.

4.7.3 Lift control by varying robot head shape

Motivated by our observations of how lift force varied with the shape of the dragged object, we tested the objects in Group I (Fig. 65 A) as a robot head to see how the head shape affected the trajectory of the robot in the vertical plane (Fig. 69). For each test, we quantified the effect by measuring the rate of vertical displacement of the robot (cm/cycle).

We found that similar to the results in the previous section, the head of the robot experienced a lift force as it moved forward. The lift force resulted in a torque imbalance which caused the robot to pitch and rise to the surface for head shapes with $\alpha < 90°$, and for $\alpha > 120°$ the robot head descended into the media. For $100° < \alpha < 120°$, the robot did not move vertically until it encountered the end of the container because for these shapes there was no net lift force on the robot head. The forward speed for head shapes with no lift was 0.28 ± 0.02 body-length/cycle, approximately the same as measured in [80]. Testing the robot's ability to dive deeper into the material was not possible due to motor torque limitations.

Increasing the length of the longest dimension of the robot head to modulate α and hence control lift is not a practical method to actively control force. Another potential mechanism of trajectory control could be to vary the inclination of the robot's head which is equivalent to varying α, and hence the associated lift forces.

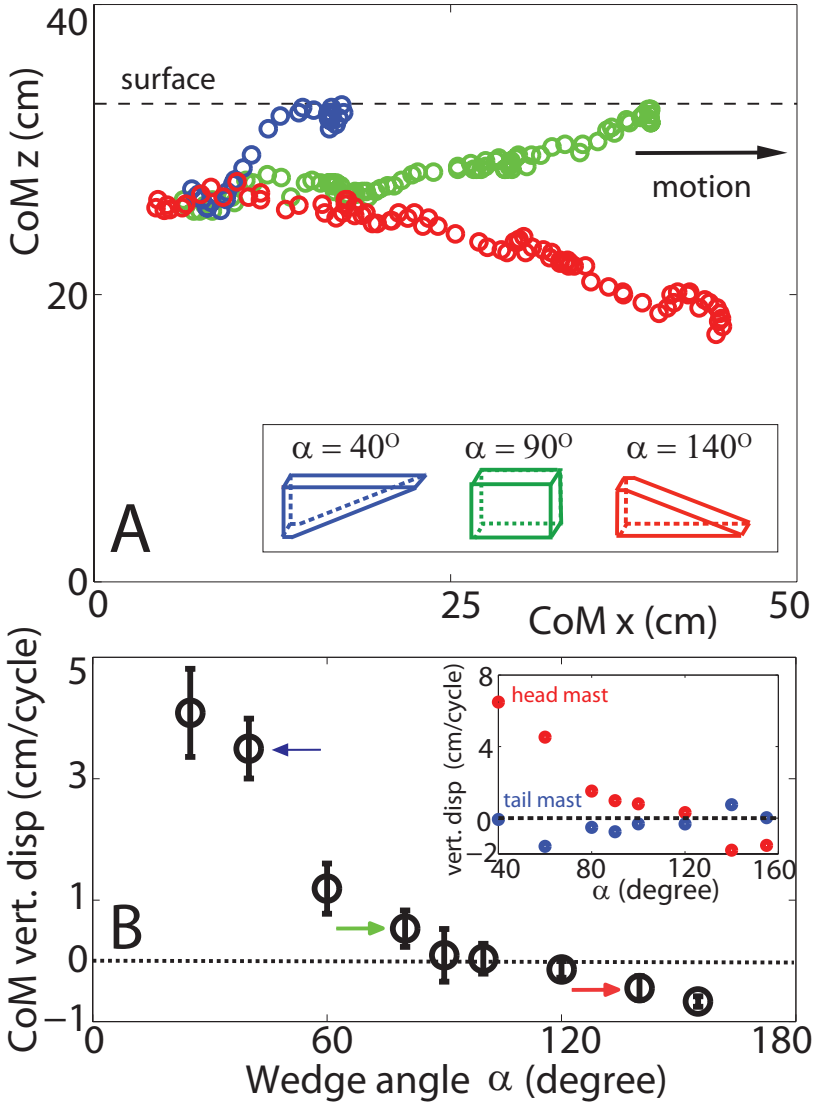

Figure 69: Vertical trajectories and average vertical displacement per cycle of the sand-swimming robot tested with head shapes with a single inclined surface (Group I, Fig. 65 A). (A) X-Z trajectory of center of mass (CoM) for α equal to 40° (blue), 90° (green), and 140° (red). Inset: head shapes. (B) Average vertical displacement of CoM per cycle ($N = 3$ runs) vs. head angle α. Inset shows the lift induced at the head and tail segments of the robot for each representative head shape.

We tested this mechanism with the second set of head shapes (Fig. 65 B, (Group II)), for which angle of both the upper and lower face of the wedge were varied, while keeping the height, length, and projected front and lateral areas fixed. These head shapes approximated the variations in α (effective) that would be introduced by inclining the head, by varying the height of the leading edge (h) between zero and the half the height of the wedge ($H/2$)

(Fig. 70 inset). For these head shapes, the height, and projected front and lateral area were fixed (same as the Group I shapes), and the length of the head was same as the wedge with $\alpha = 155°$ in Group I.

For the head shape with $h = 0$ and $\alpha = 155°$, the robot head generated a negative lift force, which pitched it downward allowing it to progress deeper into the media. For $h = H/4$, their was no net lift force on the head as the robot moves forward and consequently no motion in the vertical plane. Contrary to a symmetric object moving in a fluid which experiences no lift, a symmetric head shape in granular media ($h = H/2$) generates positive lift. The Group II head shape may be decomposed into two Group I shapes with their bases attached: the net drag and lift is then a sum of the forces on each face. For the symmetric wedge, α for the top and bottom wedges are 170° and 10° which corresponds to a net positive lift force and which explains the robot's upward motion. A similar decomposition was successfully used to calculate net drag and thrust on the sandfish in the horizontal plane [82].

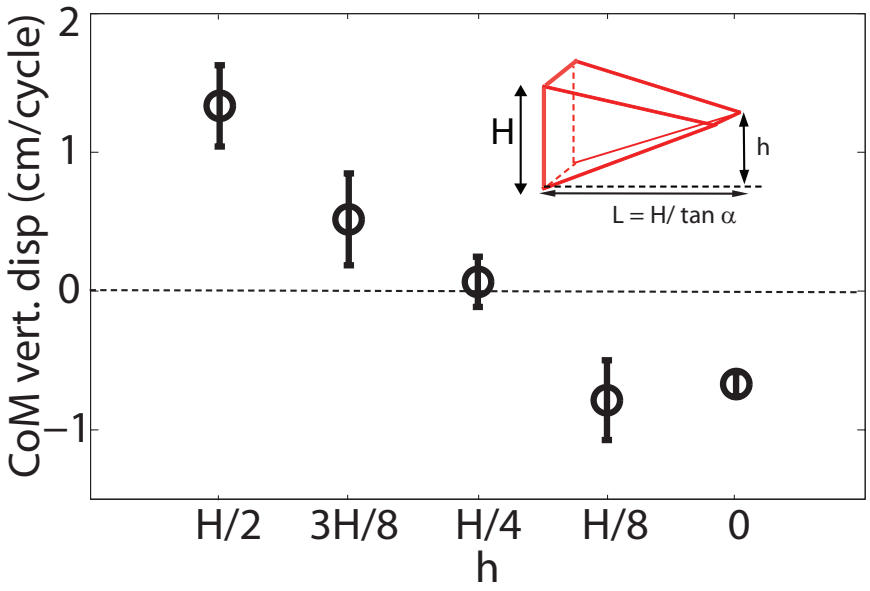

Figure 70: Average vertical displacement of a sand-swimming robot tested with head shapes with two inclined surfaces (Group II). Average vertical displacement per cycle for robot with heads in Fig. 65 B. Inset shows the dimensions of the head. The height H and length L of the wedge were fixed at 5 cm and 11 cm, respectively and corresponding to the values measured for the dimensions of the wedge with $\alpha = 155°$ tested as an object in Group I.

Having identified robot head shapes that produced either positive, negative or zero lift of the center of mass as it progressed forward, we now describe further details of the robot kinematics. As the robot began to move forward the head experienced a lift force that caused a torque imbalance. The torque caused the head segment to pitch (at angle γ) about the tail segment which raised the center of mass. For the different head shapes tested the robot head generated varied lift while the tail experienced nearly no lift (Fig. 69 inset). For head shapes with positive lift, the robot's head always exited the material first, and the tail only rose upward after the head reached the surface.

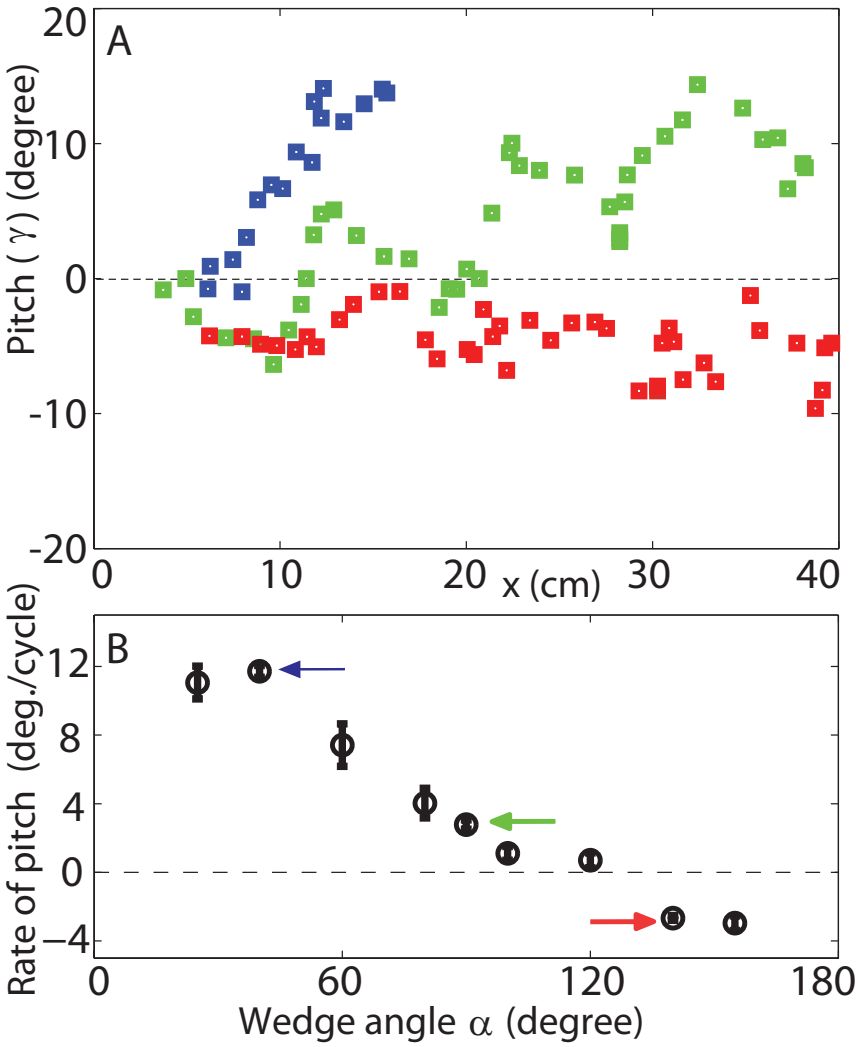

Figure 71: Pitch of the robot with Group I head shapes as it swims within 6 mm plastic particle. Pitch of the robot vs. forward displacement. (A) Blue, green, and red squares correspond to the robot with α equal to 40°, 90°, and 140°. (B) Change in pitch per cycle measured for the Group I heads tested.

Tracking the pitching of the head and tail (which are equal because the robot undulates in a plane) for the robot tested with the Group I head shapes revealed that γ increased continuously as the robot progressed forward for all head shapes tested (Fig. 71 A).

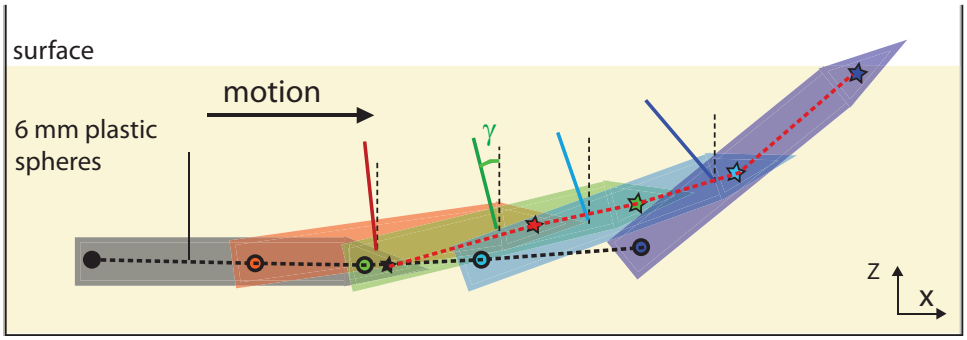

Figure 72: Cartoon of illustrating the lift and pitch experienced by the robot ($h > H/4$) swimming within granular media. The different colors indicate the position of the robot as it advances in time. Dashed red and black lines connecting the circles and stars correspond to the position of the head and tail segments of the robot. The lines perpendicular to the robot body indicate the pitch (γ).

4.7.4 Lift control by varying robot body shape

Drag induced lift results from the vertical component of the normal force on an inclined surface dragged through a granular medium. The previous section showed how these lift forces can be manipulated by varying the robot head shape as it swims within the granular medium to control the robot's vertical position. For these experiments the sides of the robot were flat. In this study, we investigated whether it was possible to generate and manipulate drag induced lift forces by modifying the robot body shape with light-weight wedges bonded to its side-walls (see Fig. 73). We hypothesized that as the robot with body wedges undulated its sides would induce a lift, and that its performance would be determined by the angle of the wedge.

Adding the wedges to the sides of the robot affected its performance (measured as number of cycle to reach the surface). We found that for the robot with large angled wedges (oriented as seen in Fig. 73) rises upward much slower than for the robot with small angled wedges (robot orientation rotated 180° along its long axis) (see Fig. 74). Based on the drag experiments from the previous section we had expected the robot with large angled

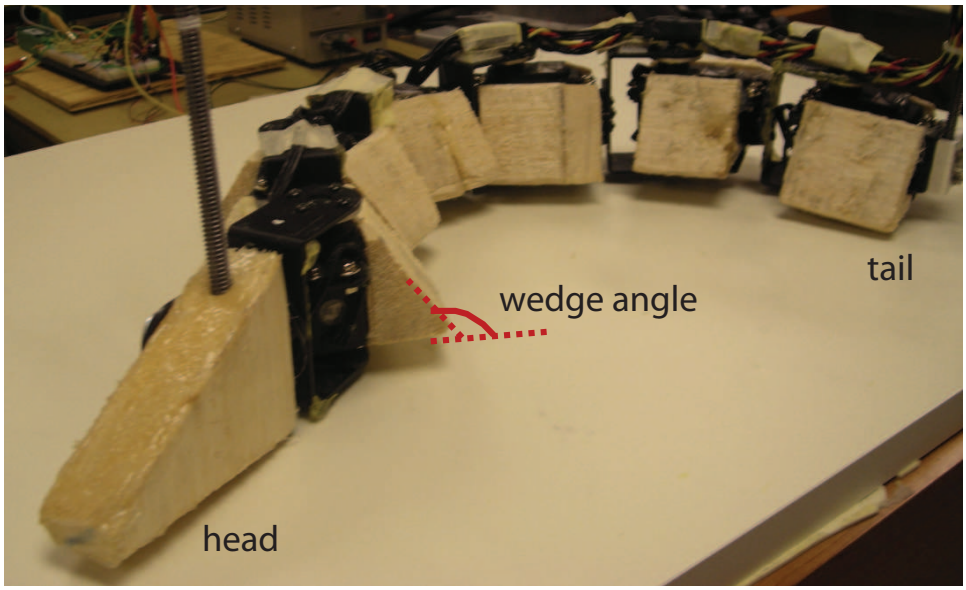

Figure 73: Construction of the sand-swimming robot with light-weight wedges fixed to each segment side wall, except the head.

wedges on its head and body to move deeper into the material, but instead the robot moved up toward the surface as it progressed forward. A potential cause for this may be the sharp transition in shape from the head to the second segment (see Fig. 73). Also variations shape of the wedges and possible upward inclination of the robot head might have contributed to this result.

The major issue with doing this study for a range of wedge angles is that depending on the anlge of the wedges the maximum angle that the joint between segments can move through changes making testing the effect of spatial characteristics on performance difficult. Also, for each wedge design new casings for the robot have to be made. Overall, modulating the vertical position of the sand-swimming robot subsurface is more convenient, and probably as effective by controlling only the robot head shape.

4.7.5 Summary

In this section, inspired by the head shape of the sandfish lizard and informed by dragging various objects through granular media we identified head shapes that could control the vertical motion of the sand-swimming robot as it swam forward within a granular medium. We used a numerical simulation of object drag to describe the mechanism of force generation

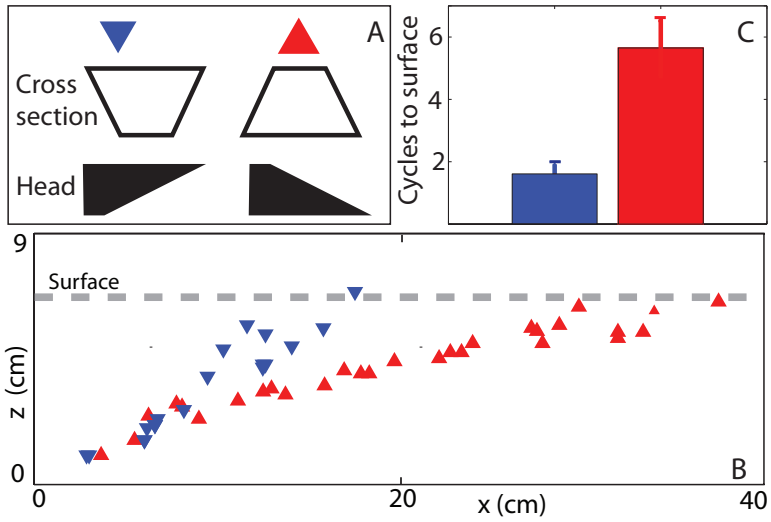

Figure 74: Effect of body shape on the vertical motion trajectory of the sand-swimming robot. (A) Diagrams of the different body cross-sections (and head shapes) tested, and the red and blue symbols used in (B) and (C) to represent them. (B) The x-z trajectories of the robot with the different body shapes. (C) Shows the number of cycles the robot took to reach to the surface with the different body shapes tested. The robot was tested in 6 mm plastic particles.

at the particle level, and used our drag experiments to set up hypothesis for the lift generated for a robot tested with different head shapes. For wedge shapes with $\alpha < 100°$ the robot rose to the surface while for $\alpha > 120°$ the robot moved deeper into the media. We were also able to show that lift can be controlled by varying the inclination of the robot head with respect to its long axis plane. We also showed that varying the body shape of the robot can control the lift generated but found this mechanism not as inconvenient or as effective as using head shape to control lift. These robot lift results generate the testable hypothesis that the sandfish could vary its α by varying the inclination of its head to maintain a straight line trajectory while swimming subsurface. This however has not been tested in animal experiment.

4.8 Above surface performance of the sand-swimming robot

Robot on a rigid surface

Snakes on rigid surfaces progress forward using lateral undulations largely due to an anisotropy in their forward and lateral frictions [60]. Inspired by this observation we tested the locomotor ability of our robot (encased in a spandex skin) on a flat rigid surface covered with a thin cotton fabric. We found that the due to the isotropy in friction between the two interacting surfaces the robot did not progress forward as it undulated (see Fig. 75 A-C). We then introduced a similar frictional anisotropy that allows a snake to progress forward to the casing of the robot. We did this by gluing to appropriate locations on the base of the robot a nylon material known as ski skin which is used to line the underside of skis. This material enable the skier to glide forward but not backward as they ascend a snow slope. We found that with this modified casing the robot moved forward as it undulated on the same rigid surface with an η of approximately 0.2 (see Fig. 75 D-F). Only a single video was collected for this experiment, *

Robot on the surface of granular media

We tested the ability of the robot (with the isotropic casing) to use lateral undulation to progress forward on the surface of granular material (6 mm plastic particles used for our subsurface robot experiments) (see Fig. 76). For $A/\lambda = 0.2$ and $\xi = 1$, the robot progressed above surface with $\eta = 0.39$ (subsurface, η was 0.34 (experiment) and 0.36 (simulation) for the robot, see Section 4.3 and 4.4 for details)

To test whether the kinematic conditions that maximized the forward speed of the robot subsurface remained the same for an undulator on the surface of granular media, we varied the ratio of A to λ (as in Chapter III, Section 3.3.2) and measured the forward speed. We found that the robot progressed forward fastest for a single period wave with $A/\lambda = 0.2$ (See Fig. 77).

These results show that the mechanism employed by snakes to move forward on rigid flat

*In collaboration with Dr.Hu's Group at Georgia Tech.

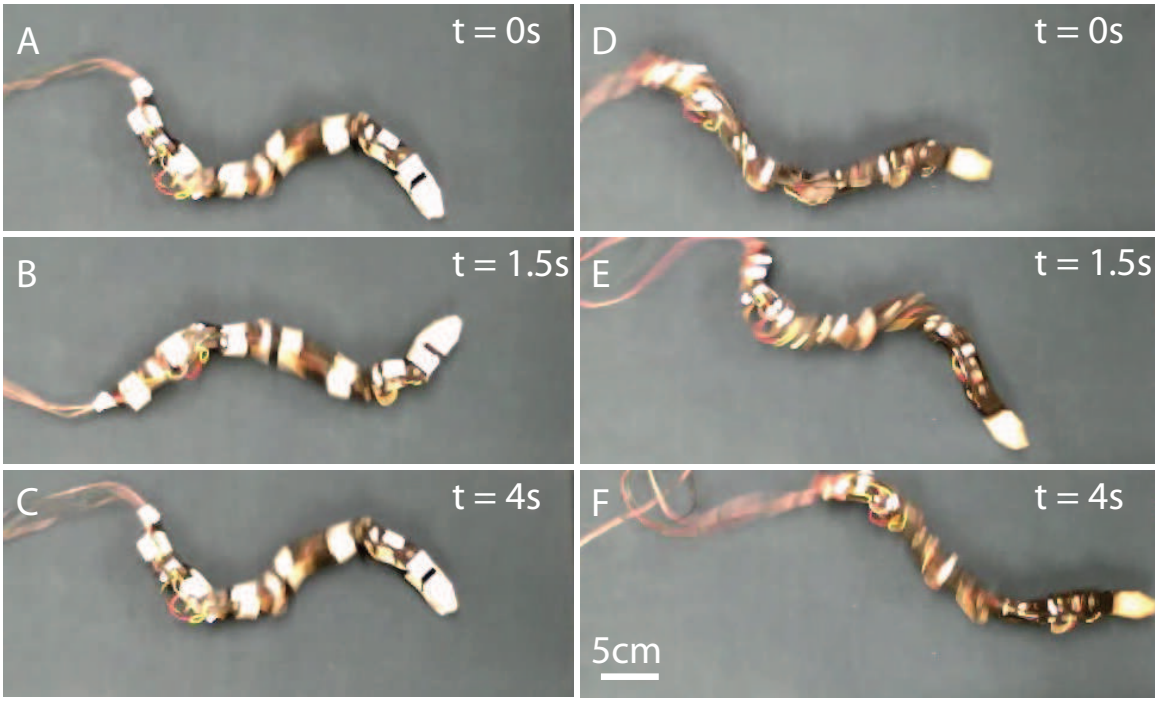

Figure 75: Top view images of the robot tested with both (A-C) isotropic and (D-F) anisotropic casings on a rigid surface covered with a thin cotton fabric. The spatial and temporal parameters were kept fixed for both tests.

surfaces is fundamentally different from that employed when moving on deformable media. On deformable media the undulators (including snakes and the robot) utilize the resistive force generated by pushing their body laterally against the medium to generate thrust and move forward. In this case the motion is not driven by the anisotropic friction properties of the interacting surfaces alone.

For snakes moving on the surface of deformable media η is reported to be closer to 0.9 [60]. Contrary to the simple planar gait of the robot in the tests above, the mechanics of a snake is more complicated. As a snake undulates laterally to progress forward its entire body does not make contact with the media instead it lifts parts of its body off the medium to reduce frictional losses and maintains contact at only a few points.

We tested the performance of the robot on poppy seeds to check if it was a function of the particle friction (6 mm plastic particle with $\mu_{pp} = 0.1$). When placed on the surface of a level bed of poppy seeds we found that the robot moved forward with a low η (< 0.15). As the robot was submerged to different depths (less that its height) it moved forward with

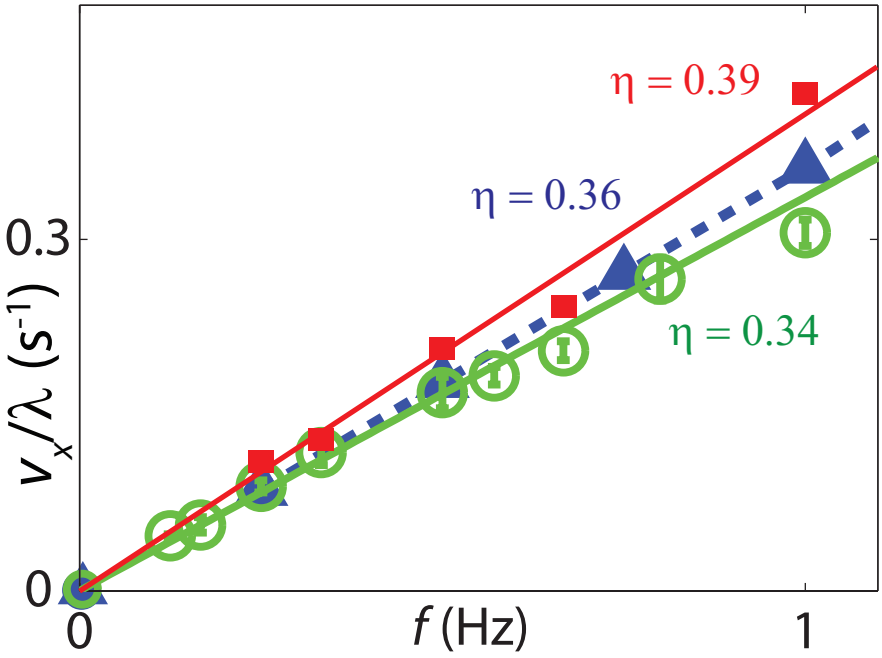

Figure 76: Forward velocity vs. oscillation frequency relationship for the robot subsurface in experiment (green circles) and in simulation (blue triangles), and above surface (red squares) in experiment ($A/\lambda = 0.2$ and $\xi = 1$). The slope of the dashed blue (subsurface simulation), solid green (subsurface experiment), and red solid (above surface experiment) fit lines give wave efficiencies η of 0.36, 0.34, and 0.39, respectively. The granular medium tested was 6 mm particles.

a visually higher η initially (first half cycle) after which η rapidly decreased to what was observed when the robot was placed on the surface. Visually, the material flowed back faster toward the robot as it undulated for the 6 mm particles than for the poppy seeds, which potentially provided the robot with more material to push off from as it progressed forward. In Chapter III (Section 3.5) we showed that η for an undulator subsurface did not vary if both μ_{bp} and μ_{pp} increased or decreased simultaneously, as in the case of the robot swimming with poppy seeds and plastic particles ($\eta \approx 0.35$ for both). However, the above surface performance of the robot on these media was different, suggesting that the physics governing the locomotion above and within granular media may be very different.

Overall, results of these above surface experiments were insightful and additional work beyond the scope of this dissertation is required to explain undulatory locomotion on granular media. This has been suggested as a potential project in Chapter V.

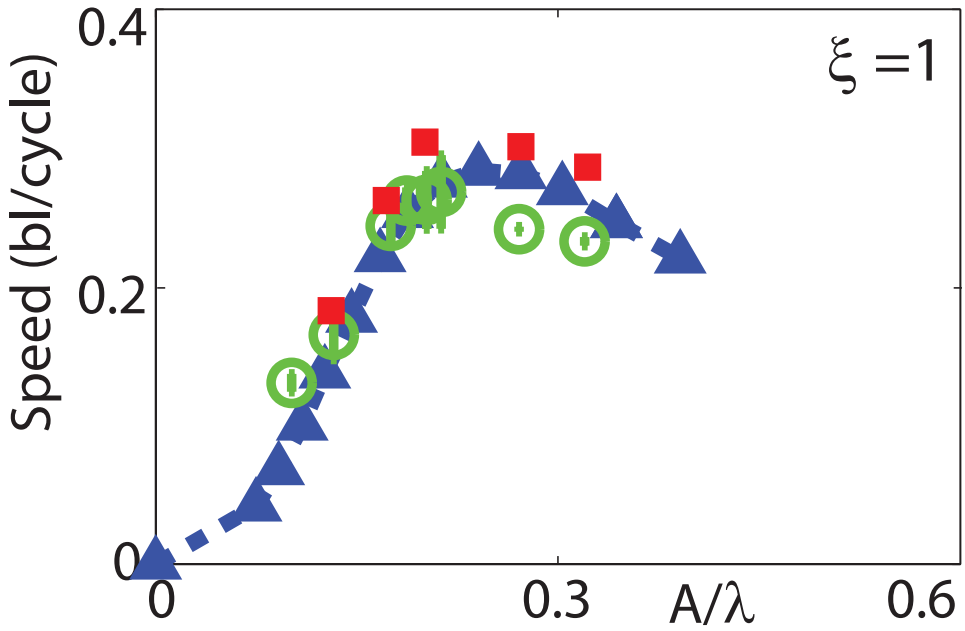

Figure 77: Effect of varying A/λ on the swimming speed of the physical robot swimming on the surface of (red), and within (green) granular media. The results for the simulated robot are shown in blue. The granular medium was 6 mm plastic particles.

4.9 Conclusion

In this chapter, inspired by the biological sandfish experiments and challenged by the absence of robotic devices with comparable subterranean locomotor abilities, we built a physical sand-swimming robot. We showed that in both simulation and experiment the robot could swim subsurface by using body undulations and, like the animal, increased its speed by increasing its oscillation frequency. We also showed that the physical and simulated robot agreed with the optimality hypothesis that the kinematics of the sandfish maximized the forward swimming speed of an undulator with granular media. Finally, we showed that it was possible to control the lift forces and hence the vertical position of a robot swimming within granular media by controlling its head shape.

The design tools (physical and simulated robot) we have developed can be used to generate testable hypotheses of mechanical control [92] that can lead to an improved understanding of how organisms exploit the solid and fluid-like properties of granular media to move effectively within it. Results of this work also supports biological hypotheses like

morphological adaptation of desert dwelling organisms aid in their subsurface locomotion. In addition, our results provide principles for the creation of robots that can maneuver and follow arbitrary trajectories within complex substrates like sand.

CHAPTER V

CONCLUSIONS AND FUTURE DIRECTIONS

In this dissertation, we have described the development of experimental and modeling techniques to study subsurface sand-swimming. We utilized these approaches to show that like the animal, it is possible to progress forward within granular media by propagating a single period sinusoidal traveling wave posteriorly along the body and without limb use. We showed with each approach that the speed of forward progress could be increased by increasing the undulation frequency of the locomotor. Also the wave efficiency (η) of the progress was independent of the undulation frequency but dependent on the amplitude of undulation. By systematically varying kinematic parameters we discovered an optimality condition ($A/\lambda = 0.2$ and $\xi = 1$), which results from competition between η and λ, that maximizes the forward speed of a sand-swimmer. Finally, inspired by the head shape of the sandfish we showed that by choosing the appropriate head shape the vertical position of a locomotor as it swims subsurface within granular media may be controlled. Results of this work provide principles for swimming within sand by using kinematics that maximize speed, and robot head shape control to improve maneuverability. This work lends support to the hypotheses that morphological adaptations of desert dwelling organisms aid in their subsurface locomotion, and that discovery of biological principles of high performance locomotion can help create robots that can follow arbitrary trajectories within complex substrates like sand.

In this chapter we discuss questions which are natural extensions to the work described in Chapters II-IV. We have divided this into biological experiment and mechanical modeling sections.

5.1 Biological experiment

This dissertation work has only begun to probe the subsurface locomotor abilities of the sandfish. The aim of the experiments on the sandfish should be twofold: improve our

understanding of its locomotor behavior, and provide intuition to improve our modeling approaches.

(I) Varying the sandfish head shape

(A) We showed conclusively in Chapter IV that the head shape of the robot can effect its vertical position. To tie this result back to the animal and validate the biological hypothesis [6, 90] that head shape effects the sand-swimming ability of lizards with similar morphology and sand-swimming capability, we should vary the head shape of the animal in experiment.

The adjustments to the sandfish head should be non-invasive, temporary, and cause the animal minimal discomfort. An idea for this is to make a 'half-muzzle' for the sandfish such that only the shape of the top or bottom of the snout is modified. One way of doing this would be to make a CAD model of the head and fabricate it using a 3D printer. The half-muzzle can be attached to the head of the sandfish via velcro straps (light-weight and flexible) that run under its fore limbs (to avoid sliding off as the sandfish has no neck). The animal once instrumented should be allowed to recover/get used to the muzzle for a day before testing. Since the entire snout is not muzzled it should not interfere with the animal's daily function. The performance of the sandfish so instrumented should be tested using sagittal view x-rays.

(B) An alternative to animal experiments is a detailed quantitative survey/study of head and body shapes of sand-swimming lizards by accessing specimens at Natural History museums.

(II) Energetics of sand-swimming

(A) Previous studies have shown that limbless locomotion on land consumes that same amount of energy as limbed locomotion [117]. To explore the energetic cost of moving within granular material one could use a respirometer to continuously monitor the oxygen consumption levels (V_{O_2}) of the sandfish as it swims subsurface (as used in [39]). An interesting extension could be to compare this subsurface performance to measures of oxygen consumption of the animal as it runs on granular material, and on a treadmill. This study could be furthered by comparing these results for the sandfish (a sand specialist) to the

results of similar tests on a sand generalist (ex. *Callisaurus*) during running or burial.

(B) The oxygen monitoring setup could be used in conjunction with the x-ray imaging system to investigate the subsurface breathing mechanism quantitatively and test the various biological hypotheses that have been previously made about it [98].

(III) Maneuverability of the sandfish

(A) For all the animal studies presented in this dissertation, runs for which the sandfish did not move in a straight line were rejected. The turning ability of the sandfish constitutes an interesting locomotor behavior and must be studied. The numerical and physical models presented in this dissertation provide a hypothesis for the turning behavior that should be tested in the animal. The models indicate that a potential mechanism utilized by the sandfish to execute a turn could be by varying the number of periods along its body (ξ), which results in a yaw motion due to a torque imbalance (as the spatial form of the animal is not symmetric). Dorsal ventral x-ray imaging will help provided evidence to support this hypothesis.

(B) We have studied how the animal rapidly enters the material and then swims subsurface, but we have never studied the kinematics of the sandfish as it exits the medium. A limiting factor for such a study is that the sandfish spends long amounts of time ($> 2-3$ hours) within the media which make utilizing x-ray imaging for this entire duration impossible. One way to obtain images of the sandfish exiting is by triggering the x-rays only when movement of particles on the surface due to the subsurface motion of the sandfish is detected. The detection of particle movement may be done by taking laser line images of the surface every few seconds and correlating it with the previous image.

(IV) Granular particle image velocimetry (PIV) to study the sandfish

Digital Particle Image Velocimetry is an optical measurement technique which provides a means of measuring the velocity of particles in the flow of interest over/around an object or animal [50, 115]. Similar techniques have been used to study 2D granular flow fields. In these experiments the granular medium is seeded with opaque particles for flow visualization [78].

A potential study would be to extend this technology to visualize the flow of material around the sandfish as it swims subsurface. Potential problems with this technology include: it is hard to discern the exact direction of motion of the seeded particles, dispersing the seeded particles uniformly, the image would be an average of many 2D slices due to the third dimension (example: effect of height of the material during dorso-ventral granular PIV), and reseting the medium to a similar state before each run.

5.2 Mechanical modeling

The physical and numerical models could benefit from work on the following issues before they are used to test further hypotheses.

- Studying problems related to maneuvering within granular media requires a test container with dimensions much larger than that currently used in simulation, but increasing the number of particles would increase the computational time significantly. One suggestion for reducing the number of particles (and computational time) required is to generate a limited vertical section of simulated granular material that is placed before the advancing sandfish while the section behind it is removed.

- For the physical robot the wiring has been an issue to the constant wear and tear. Wires coming in contact with the moving joints has led to the insulation getting stripped and the control signal being affected. Care must be taken to encase the wires in a sheath of heat shrink to add a layer of insulation while not adding to much to its overall stiffness.

- The technique for leveling the granular material once the robot is placed subsurface should be standardized.

The infrastructure (numerical and physical model) that has been developed has opened the doors to a range of fascinating questions. Below are some studies that could utilize these modeling approaches to test biological hypotheses, and also develop a better robot.

(I) Further studies on lift control in the robot

(A) We observed that when a robot with a head that experiences no lift (when oriented in the horizontal plane) is placed out of the plane of the robot it rises or sinks based on the orientation of its wedge head with respect to gravity. Of immediate interest would be to systematically study this effect on the robot and to study the physics of lift on wedges dragged within granular media at different incline angles.

(B) In [82], we found that the thrust and drag on the end caps of a cylindrical segment, dragged through 3 mm glass particles, varies with its orientation (ψ) with respect to its velocity direction. For the robot, we can test the hypothesis that the forces (including lift) on its head would vary with ψ. Knowing how the magnitude and direction of lift force varies as the robot undulates would help identify phases of the wave traveling along the undulator that maximize the lift forces while minimizing the drag.

(C) To overcome the torque limitations of our motors in the physical device, we should adapt the numerical robot simulation developed in [80] to allow us to test the performance of the robot when placed at various incline angles, and how this couples with the wedge angle (α). The robotic simulation can also tune parameters like media properties like particle friction and hardness, and test for the effect of depth on our current observations on the effect of shape on lift.

(I) Effect of choice of waveform on locomotion

The sandfish swims subsurface by propagating a sinusoidal traveling wave posteriorly along its body. The animal may utilize a traveling wave that was well modeled by a sinusoid due to reasons like anatomical limitations. The aim of the study suggested here is to determine the effect of varying the shape of the waveform propagating along the body. Lighthill [76] showed that for fluid the most efficient wave propagating along the body for locomotion within fluids is a triangular waveform. We could test whether the kinematic conditions that maximizes forward speed for a sinusoidal traveling wave varied with wave shape within granular material. Pilot studies revealed that for the robot its finite number of segments [7] results in only small differences between the different wave shapes tested.

These experiments can better done in simulation as the undulator models can be more easily adjusted to have a larger number of segments.

(II) Scallop theorem in granular material

Purcell proposed the scallop theorem which showed that an animal with only one joint cannot propel itself in a low Reynolds number environment [100]. To move the animals must move its appendage fast enough to increase its Re number so that it propels itself due to inertial reaction. Similarly, testing the ability of a 2 segment single joint robot to propel itself within granular material would be interesting because for a relatively large range in velocities ($0 - 40\,\mathrm{cm/s}$) the forces generated are independent of velocity. As the velocity of the appendages is increased the robot would create a void in the region through which its appendages sweeps as the particles would not be able to refill the space fast enough. The question to ask would be whether/how a single joint sand-swimmer could move within granular material.

(III) Maneuverability of the sand-swimming robot

In this dissertation we have shown that it is possible to regulate the vertical position of the robot by choosing an appropriate head shape and varying its angle of attack. We have also shown in simulation that varying the number of periods along the body of the robot results in a yaw motion. If both these controls (number of periods and head shape) are modulated correctly it would be possible to achieve desired 3D trajectories.

(IV) Limbless locomotion on the surface of granular media

A survey of the snake robot literature reveals that no emphasis has been placed on testing robot designed for moving on complex substrates like building rubble following natural disasters to study the effect of kinematics, morphology etc on performance metrics like speed, stability and energetics [57]. The simulation and robotic tools used in this dissertation can be directly utilized to study limbless locomotion on granular media.

All the projects part of this dissertation have had their own set of challenges, but each of them has been fascinating and enjoyable to work on. The range in experimental and modeling tools developed has helped lead me to a large number of ideas, hypotheses, and questions related to both the biology and engineering. I look forward to hearing about (and possibly working on) some of these.

REFERENCES

[1] Albert, R., Pfeifer, M. A., Barbási, A.-L., and Schiffer, P., "Slow drag in a granular medium," *Phys. Rev. Lett.*, vol. 82, p. 205, 1999.

[2] Albert, R., Pfeifer, M. A., Barbási, A. L., and Schiffer, P., "Slow drag in a granular medium," *Physical Review Letters*, vol. 82, no. 1, pp. 205–208, 1999.

[3] Alexander, R. M., *Principles of Animal Locomotion*. Princeton University Press, 2003.

[4] Arena, P., Di Giamberardino, P., Fortuna, L., La Gala, F., Monaco, S., Muscato, G., Rizzo, A., and Ronchini, R., "Toward a mobile autonomous robotic system for Mars exploration," *Planetary and Space Science*, vol. 52, no. 1-3, pp. 23–30, 2004.

[5] Arnold, E., "Why do Morphological Phylogenies Vary in Quality? An Investigation Based on the Comparative History of Lizard Clades," *Proceedings of the Royal Society of London. B. Biological Sciences*, vol. 240, no. 1297, p. 135, 1990.

[6] Arnold, E., "Identifying the effects of history on adaptation: Origins of different sand-diving techniques in lizards," *Journal of Zoology*, vol. 235, no. 3, pp. 351–388, 1995.

[7] Arnold, E., "Identifying the effects of history on adaptation: origins of different sand-diving techniques in lizards," *J. Zool., Lond*, vol. 235, pp. 351–388, 1995.

[8] Ashcheulov, A., Gutsul, I., and Maevski, V., "Device for monitoring the radiation temperature in coal mines," *Journal of Optical Technology*, vol. 67, no. 3, p. 281, 2000.

[9] Bagnold, R. A., *The Physics of Blown Sand and Desert Dunes*. Methuen and Co. Ltd., 1954.

[10] Baumgartner, W., Fidler, F., Weth, A., Habbecke, M., Jakob, P., Butenweg, C., and Böhme, W., "Investigating the locomotion of the sandfish in desert sand using nmr-imaging," *PLoS ONE*, vol. 3, no. 10, pp. e3309:1–10, 2008.

[11] Baumgartner, W., Saxe, F., Weth, A., Hajas, D., Sigumonrong, D., Emmerlich, J., Singheiser, M., Boehme, W., and Schneider, J., "The Sandfish's Skin: Morphology, Chemistry and Reconstruction," *Journal of Bionic Engineering*, vol. 4, no. 1, pp. 1–9, 2007.

[12] Bekker, M., *Theory of Land Locomotion*. The University of Michigan Press, 1956.

[13] Berri, S., Boyle, J., Tassieri, M., Hope, I., and Cohen, N., "C. elegans locomotion: a unified multidisciplinary perspective," *BMC Neuroscience*, vol. 10, no. Suppl 1, p. P16, 2009.

[14] Biewener, A. A. and Gillis, G. B., "Dynamics of muscle function during locomotion: Accommodating variable conditions," *Journal of Experimental Biology*, vol. 202, no. 23, pp. 3387–3396, 1999.

[15] Bizon, C., Shattuck, M. D., Swift, J. B., McCormick, W. D., and Swinney, H. L., "Patterns in 3-dimensional vertically oscillated granular layers: Simulation and experiment," *Phys. Rev. Lett.*, vol. 80, pp. 57–60, 1998.

[16] Charbonneau, P., Hare, L., and Carignan, R., "Use of X-ray images and a contrasting agent to study the behavior of animals in soft sediments," *Limnology and Oceanography*, vol. 42, no. 8, pp. 1823–1828, 1997.

[17] Chen, I., Yeo, S., and Senanayake, R., "Navigation and gait planning for Planar Walker," in *Proceedings of the 8th International Symposium on Advances in Robot Kinematics*, pp. 491–500, 2002.

[18] Chigisaki, S., Mori, M., Yamada, H., and Hirose, S., "Design and control of amphibious Snake-like Robot" ACM-R5".," *Nippon Kikai Gakkai Robotikusu, Mekatoronikusu Koenkai Koen Ronbunshu (CD-ROM)*, vol. 2005, 2005.

[19] Chirikjian, G. and Burdick, J., "The kinematics of hyper-redundant robot locomotion," *IEEE transactions on robotics and automation*, vol. 11, no. 6, pp. 781–793, 1995.

[20] Choset, H., Luntz, J., Shammas, E., Rached, T., Hull, D., and Dent, C., "Design and motion planning for serpentine robots," in *Proceedings of SPIE*, vol. 3990, p. 148, 2000.

[21] Christy, J., "Burrow structure and use in the sand fiddler crab, Uca pugilator (Bosc)," *Animal Behaviour*, vol. 30, no. 3, pp. 687–694, 1982.

[22] Cohen, N. and Boyle, J., "Undulatory Locomotion," *Imprint*, 2009.

[23] Cortez, R., Fauci, L., Cowen, N., and Dillon, R., "Simulation of swimming organisms: coupling internal mechanics with external fluid dynamics," *Computing in Science & Engineering*, vol. 6, no. 3, pp. 38–45, 2005.

[24] Crespi, A., Badertscher, A., Guignard, A., and Ijspeert, A., "Swimming and crawling with an amphibious snake robot," in *IEEE International Conference On Robotics And Automation*, vol. 3, p. 3024, Citeseer, 2005.

[25] Darwin, C., *The Formation of Vegetable Mould, Through the Action of Worms: with Observations on Their Habits*. D. Appleton & Company, 1882.

[26] Darwin, C. R., *The formation of vegetable mould, through the action of worms: with observations on their habits*. London: John Murray, 1881.

[27] Desai, R., Rosenberg, C., Jones, J., and Inc, I., "Kaa: an autonomous serpentine robot utilizes behavior control," in *Proceedings of the 1995 International Conference on Intelligent Robots and Systems, Pittsburgh*, Citeseer, 1995.

[28] Dickinson, M. H., Farley, C. T., Full, R. J., Koehl, M. A. R., Kram, R., and Lehman, S., "How animals move: An integrative view," *Science*, vol. 288, p. 100, 2000.

[29] Dickinson, W. W. and Ward, J. D., "Low depositional porosity in eolian sands and sandstones, namib desert," *Journal of Sedimentary Research Section A–Sedimentary Petrology and Processes*, vol. 64, no. 2, pp. 226–232, 1994.

[30] Ding, Y., Gravish, N., and Goldman, D. I., "Drag induced lift in granular media," *Phys. Rev. Lett., In review.*

[31] Dorgan, K., Arwade, S., and Jumars, P., "Burrowing in marine muds by crack propagation: kinematics and forces," *Journal of Experimental Biology*, vol. 210, no. 23, p. 4198, 2007.

[32] Dorgan, K., Jumars, P., Johnson, B., Boudreau, B., and Landis, E., "Burrowing mechanics: burrow extension by crack propagation.," *Nature*, vol. 433, no. 7025, p. 475, 2005.

[33] Dowling, K., "Limbless locomotion: learning to crawl," in *1999 IEEE International Conference on Robotics and Automation, 1999. Proceedings*, vol. 4, 1999.

[34] Downing, J. and Rigler, F., *A Manual on Methods for the Assessment of Secondary Productivity*. Blackwell Scientific Publications, Oxford, UK, 1984.

[35] Ezcurra, E., *Global Deserts Outlook*. United Nations Educational, 2006.

[36] Farley, C. and Ko, T., "Mechanics of locomotion in lizards," *Journal of Experimental Biology*, vol. 200, pp. 2177–2188, 1997.

[37] Fish, F., "Wing design and scaling of flying fish with regard to flight performance," *Journal of Zoology*, vol. 221, no. 3, pp. 391–403, 1990.

[38] Fish, F. and Lauder, G., "Passive and active flow control by swimming fishes and mammals," *Annual Review of Fluid Mechanics*, p. 38, 2006.

[39] Full, R. I., Assad, J. A., and Herreid, C. F., I., "The economics of cockroaches exercising with loads," *American Zoologist*, vol. 24, no. 3, p. 123A, 1984.

[40] Gans, C., "Terrestrial locomotion without limbs," *American Zoologist*, vol. 2, no. 2, pp. 167–182, 1962.

[41] Gans, C., "Tetrapod limblessness: evolution and functional corollaries," *Integrative and Comparative Biology*, vol. 15, no. 2, p. 455, 1975.

[42] Gillis, G., "Undulatory locomotion in elongate aquatic vertebrates: Anguilliform swimming since Sir James Gray," *Integrative and Comparative Biology*, vol. 36, no. 6, p. 656, 1996.

[43] Goldman, D. I. and Umbanhowar, P., "Scaling and dynamics of sphere and disk impact into granular media," *Physical Review E*, vol. 77, no. 2, pp. 021308–021321, 2008.

[44] Goldman, D. and Umbanhowar, P., "Scaling and dynamics of sphere and disk impact into granular media," *Physical Review E*, vol. 77, no. 2, p. 21308, 2008.

[45] Granosik, G., Hansen, M., and Borenstein, J., "The OmniTread serpentine robot for industrial inspection and surveillance," *Industrial Robot: An International Journal*, vol. 32, no. 2, pp. 139–148, 2005.

[46] Gray, J., "The mechanism of locomotion in snakes," *Journal of Experimental Biology*, vol. 23, no. 2, p. 101, 1946.

[47] Gray, J. and Hancock, G., "The propulsion of sea-urchin spermatozoa," *Journal of Experimental Biology*, vol. 32, no. 4, p. 802, 1955.

[48] Gray, J. and Lissmann, H., "The locomotion of nematodes," *Journal of Experimental Biology*, vol. 41, no. 1, p. 135, 1964.

[49] Gutiérrez, J., Jones, C., Groffman, P., Findlay, S., Iribarne, O., Ribeiro, P., and Bruschetti, C., "The contribution of crab burrow excavation to carbon availability in surficial salt-marsh sediments," *Ecosystems*, vol. 9, no. 4, pp. 647–658, 2006.

[50] Haam, S. J. and Brodkey, R. S., "Motions of dispersed beads obtained by particle tracking velocimetry measurements, part II," *International Journal of Multiphase Flow*, vol. 26, 2000.

[51] Hershey, A., "Tubes and foraging behavior in larval Chironomidae: implications for predator avoidance," *Oecologia*, vol. 73, no. 2, pp. 236–241, 1987.

[52] Hirose, S., *Biologically Inspired Robots: Serpentile Locomotors and Manipulators*. Oxford University Press, 1993.

[53] Hirose, S. and Morishima, A., "Design and control of a mobile robot with an articulated body," *The International Journal of Robotics Research*, vol. 9, no. 2, p. 99, 1990.

[54] Hirose, S., Morishima, A., Tukagosi, S., Tsumaki, T., and Monobe, H., "Design of practical snake vehicle: Articulated body mobile robot KR-II," in *Advanced Robotics, 1991.'Robots in Unstructured Environments', 91 ICAR., Fifth International Conference on*, pp. 833–838, IEEE, 2002.

[55] Hoffstetter, R. and Gasc, J., "Vertebrae and ribs of modern reptiles," *Biology of the Reptilia*, vol. 1, no. 5, pp. 201–310, 1969.

[56] Hoover, A. M., Steltz, E., and Fearing, R. S., "Roach: An autonomous 2.4 g crawling hexapod robot," 2008.

[57] Hopkins, J., Spranklin, B., and Gupta, S., "A survey of snake-inspired robot designs," *Bioinspiration & Biomimetics*, vol. 4, p. 021001, 2009.

[58] Horst, T., "Population dynamics of the burrowing mayfly Hexagenia limbata," *Ecology*, vol. 57, no. 1, pp. 199–204, 1976.

[59] Howard, J., "X-Ray Radiography for Examination of Burrowing in Sediments by Marine Invertebrate Organisms," *Sedimentology*, vol. 11, no. 3-4, pp. 249–258, 1968.

[60] Hu, D., Nirody, J., Scott, T., and Shelley, M., "The mechanics of slithering locomotion," *Proceedings of the National Academy of Sciences*, vol. 106, no. 25, p. 10081, 2009.

[61] Humphrey, C. and Adams, J., "Robotic Tasks for Chemical, Biological, Radiological, Nuclear and Explosive Incident Response," *Advanced Robotics*, vol. 23, no. 9, pp. 1217–1232, 2009.

[62] Ijspeert, A., Crespi, A., Ryczko, D., and Cabelguen, J., "From swimming to walking with a salamander robot driven by a spinal cord model," *Science*, vol. 315, no. 5817, p. 1416, 2007.

[63] Jaeger, H. M., Nagel, S. R., and Behringer, R. P., "The physics of granular material," *Physics Today*, vol. 49, no. 4, pp. 32–38, 1996.

[64] Jayne, B., "Kinematics of terrestrial snake locomotion," *Copeia*, pp. 915–927, 1986.

[65] Jayne, B., "Muscular mechanisms of snake locomotion: an electromyographic study of the sidewinding and concertina modes of Crotalus cerastes, Nerodia fasciata and Elaphe obsoleta," *J. exp. Biol*, vol. 140, no. 1, pp. 1–33, 1988.

[66] Kim, H., Shim, D., and Sastry, S., "Flying robots: modeling, control and decision making," in *IEEE International Conference on Robotics and Automation, 2002. Proceedings. ICRA'02*, vol. 1, 2002.

[67] Kim, S., Clark, J. E., and Cutkosky, M. R., "isprawl: Design and tuning for high-speed autonomous open-loop running," *International Journal of Robotics Research*, vol. 25, no. 9, 2006.

[68] Klaassen, B. and Paap, K., "GMD-SNAKE 2: a snake-like robot driven by wheels and a method for motion control," in *Proceedings from the IEEE International Conference On Robotics And Automation*, vol. 4, pp. 3014–3019, 1999.

[69] Korta, J., Clark, D., Gabel, C., Mahadevan, L., and Samuel, A., "Mechanosensation and mechanical load modulate the locomotory gait of swimming C. elegans," *Journal of Experimental Biology*, vol. 210, no. 13, p. 2383, 2007.

[70] Kotay, K. and Rus, D., "The inchworm robot: A multi-functional system," *Autonomous Robots*, vol. 8, no. 1, pp. 53–69, 2000.

[71] Lauder, G. and Drucker, E., "Forces, Fishes, and Fluids: Hydrodynamic Mechanisms of Aquatic Locomotion," *Physiology*, vol. 17, no. 6, pp. 235–240, 2002.

[72] Lee, J. and Herrmann, H., "Angle of repose and angle of marginal stability: molecular dynamics of granular particles," *Journal of Physics A: Mathematical and General*, vol. 26, pp. 373–383, 1993.

[73] Li, C., Umbanhowar, P. B., Komsuoglu, H., and Goldman, D. I., "The effect of limb kinematics on the speed of a legged robot on granular media," *Journal of Experimental Mechanics, in review*, 2010.

[74] Li, C., Umbanhowar, P. B., Komsuoglu, H., Koditschek, D. E., and Goldman, D. I., "Sensitive dependence of the motion of a legged robot on granular media," *Proceedings of the National Academy of Science*, vol. 106, no. 9, pp. 3029–3034, 2009.

[75] Lighthill, J. and Lighthill, M., *Mathematical biofluiddynamics*. Society for Industrial Mathematics, 1975.

[76] Lighthill, J., *Waves in Fluids*. Cambridge: Cambridge University Press, 1978.

[77] Liu, H., "Simulation-based biological fluid dynamics in animal locomotion," *Applied Mechanics Reviews*, vol. 58, p. 269, 2005.

[78] Lueptow, R., Akonur, A., and Shinbrot, T., "PIV for granular flows," *Experiments in Fluids*, vol. 28, no. 2, pp. 183–186, 2000.

[79] Lyman, F., "Environmental factors affecting distribution of mayfly nymphs in Douglas Lake, Michigan," *Ecology*, vol. 37, no. 3, pp. 568–576, 1956.

[80] Maladen, R., Ding, Y., Umbanhowar, P., Kamor, A., and Goldman, D., "Biophysically inspired development of a sand-swimming robot," in *Proceedings of Robotics: Science and Systems*, (Zaragoza, Spain), June 2010.

[81] Maladen, R., Ding, Y., Kamor, A., Umbanhowar, P., and Goldman, D., "Mechanical models of sandish locomotion reveal principles of high performance subsurface sand-swimming," *Journal of The Royal Society Interface, In review*.

[82] Maladen, R., Ding, Y., Li, C., and Goldman, D., "Undulatory Swimming in Sand: Subsurface Locomotion of the Sandfish Lizard," *Science*, vol. 325, no. 5938, p. 314, 2009.

[83] Marcus, W., Legleiter, C., Aspinall, R., Boardman, J., and Crabtree, R., "High spatial resolution hyperspectral mapping of in-stream habitats, depths, and woody debris in mountain streams," *Geomorphology*, vol. 55, no. 1-4, pp. 363–380, 2003.

[84] McKean, J., Buechel, S., and Gaydos, L., "Remote sensing and landslide hazard assessment," *Photogrammetric engineering and remote sensing*, vol. 57, no. 9, pp. 1185–1193, 1991.

[85] Menciassi, A. and Dario, P., "Bio-inspired solutions for locomotion in the gastrointestinal tract: background and perspectives," *Philosophical Transactions of the Royal Society of London. Series A: Mathematical, Physical and Engineering Sciences*, vol. 361, no. 1811, p. 2287, 2003.

[86] Metternicht, G., Hurni, L., and Gogu, R., "Remote sensing of landslides: An analysis of the potential contribution to geo-spatial systems for hazard assessment in mountainous environments," *Remote sensing of Environment*, vol. 98, no. 2-3, pp. 284–303, 2005.

[87] Meysman, F., Middelburg, J., and Heip, C., "Bioturbation: a fresh look at Darwin's last idea," *Trends in Ecology & Evolution*, vol. 21, no. 12, pp. 688–695, 2006.

[88] Miller, G., "Snake robots for search and rescue," *Neurotechnology for Biomimetic Robots*, pp. 271–284, 2002.

[89] Moon, B. R. and Gans, C., "Kinematics, muscular activity and propulsion in gopher snakes," *Journal of Experimental Biology*, vol. 201, no. 19, pp. 2669–2684, 1998.

[90] Mosauer, W., "Adaptive convergence in the sand reptiles of the Sahara and of California: a study in structure and behavior," *Copeia*, pp. 72–78, 1932.

[91] Nedderman, R., *Statics and kinematics of granular materials*. Cambridge Univ Pr, 1992.

[92] Nishikawa, K., Biewener, A. A., Aerts, P., Ahn, A. N., Chiel, H. J., Daley, M. A., Daniel, T. L., Full, R. J., Hale, M. E., Hedrick, T. L., Lappin, A. K., Nichols, T. R., Quinn, R. D., Satterlie, R. A., and Szymik, B., "Neuromechanics: an integrative approach for understanding motor control," *Integrative and Comparative Biology*, vol. 47, no. 1, pp. 16–54, 2007. Times Cited: 13 Annual Meeting of the Society-for-Integrative-and-Comparative-Biology JAN 04-08, 2006 Orlando, FL.

[93] Ohno, H. and Hirose, S., "Design of slim slime robot and its gait of locomotion," in *Intelligent Robots and Systems, 2001. Proceedings. 2001 IEEE/RSJ International Conference on*, vol. 2, pp. 707–715, IEEE, 2002.

[94] Perry, R., "Principles of conventional radiography and fluoroscopy.," *The Veterinary clinics of North America. Small animal practice*, vol. 23, no. 2, p. 235, 1993.

[95] Pesch, C., Hansen, D., Boothman, W., Berry, W., and Mahony, J., "The role of acid-volatile sulfide and interstitial water metal concentrations in determining bioavailability of cadmium and nickel from contaminated sediments to the marine polychaete Neanthes arenaceodentata," *Environmental Toxicology and Chemistry*, vol. 14, no. 1, pp. 129–141, 1995.

[96] Pfeifer, R., Lungarella, M., and Iida, F., "Self-organization, embodiment, and biologically inspired robotics," *Science*, vol. 318, no. 5853, p. 1088, 2007.

[97] Playter, R., Buehler, M., and Raibert, M., "Bigdog," in *Unmanned Ground Vehicle Technology VIII* (Grant R. Gerhart, Charles M. Shoemaker, D. W. G., ed.), vol. 6230 of *Proceedings of SPIE*, pp. 62302O1–62302O6, 2006.

[98] Pough, F., "The morphology of undersand respiration in reptiles," *Herpetologica*, vol. 25, no. 3, pp. 216–223, 1969.

[99] Pough, F., "The burrowing ecology of the sand lizard, Uma notata," *Copeia*, vol. 1970, no. 1, pp. 145–157, 1970.

[100] Purcell, E., "Life at low Reynolds number," *Am. J. Phys*, vol. 45, no. 1, pp. 3–11, 1977.

[101] Rapaport, D. C., *The art of molecular dynamics simulation*. Cambridge University Press, 2nd ed., 2004.

[102] Ritzmann, R., Quinn, R., and Fischer, M., "Convergent evolution and locomotion through complex terrain by insects, vertebrates and robots," *Arthropod structure and development*, vol. 33, no. 3, pp. 361–379, 2004.

[103] Rosato, A., Strandburg, K., Prinz, F., and Swendsen, R., "Why the Brazil nuts are on top: Size segregation of particulate matter by shaking," *Physical Review Letters*, vol. 58, no. 10, pp. 1038–1040, 1987.

[104] Sane, S. and Dickinson, M., "The control of flight force by a flapping wing: lift and drag production," *Journal of experimental biology*, vol. 204, no. 15, p. 2607, 2001.

[105] Saranli, U., Buehler, M., and Koditschek, D., "Rhex: A simple and highly mobile hexapod robot," *The International Journal of Robotics Research*, vol. 20, no. 7, p. 616, 2001.

[106] Saunders, A., Goldman, D. I., Full, R. J., and Buehler, M., "The rise climbing robot: body and leg design," in *Unmanned Systems Technology VIII* (Gerhart, G. R., Shoemaker, C. M., and Gage, D. W., eds.), vol. 6230, p. 623017, SPIE, 2006.

[107] Schofield, A. N. and Wroth, C. P., *Critical State Soil Mechanics*. London: McGraw-Hill, 1968.

[108] Seymour, R., Withers, P., and Weathers, W., "Energetics of burrowing, running, and free-living in the Namib Desert golden mole (Eremitalpa namibensis)," *Journal of Zoology*, vol. 244, no. 01, pp. 107–117, 1998.

[109] Shafer, D., Young, M., Zitzer, S., Caldwell, T., and McDonald, E., "Impacts of interrelated biotic and abiotic processes during the past 125 000 years of landscape evolution in the northern Mojave Desert, Nevada, USA," *Journal of Arid Environments*, vol. 69, no. 4, pp. 633–657, 2007.

[110] Shafer, D., Young, M., Zitzer, S., McDonald, E., Caldwell, T., University, and of Nevada. Desert Research Institute, C. C. S., *Coupled environmental processes and long-term performance of landfill covers in the Northern Mojave Desert*. Division of Hydrologic Sciences, Desert Research Institute, 2004.

[111] Shan, Y. and Koren, Y., "Obstacle accommodation motion planning," in *Intelligent autonomous systems, IAS–3: proceedings of the international conference, Pittsburgh, Pennsylvania, February 15-18, 1993*, p. 94, Ios Pr Inc, 1993.

[112] Siegwart, R., Lamon, P., Estier, T., Lauria, M., and Piguet, R., "Innovative design for wheeled locomotion in rough terrain," *Robotics and Autonomous systems*, vol. 40, no. 2-3, pp. 151–162, 2002.

[113] Soller, R. and Koehler, S., "Drag and lift on rotating vanes in granular beds," *Physical Review E*, vol. 74, no. 2, p. 21305, 2006.

[114] Tritton, D., *Physical Fluid Dynamics*. Oxford University Press, 1989.

[115] Tytell, E. D. and Lauder, G. V., "The hydrodynamics of eel swimming - i. wake structure," *Journal of Experimental Biology*, vol. 207, no. 11, pp. 1825–1841, 2004.

[116] Vogel, S., *Life in Moving Fluids*. Princeton University Press, 1994.

[117] Walton, M., Jayne, B., and Bennet, A., "The energetic cost of limbless locomotion," *Science*, vol. 249, no. 4968, p. 524, 1990.

[118] Wang, W., Zhang, H., Zong, G., and Zhang, J., "Design and realization of a novel reconfigurable robot with serial and parallel mechanisms," in *Robotics and Biomimetics, 2006. ROBIO'06. IEEE International Conference on*, pp. 697–702, IEEE, 2007.

[119] White, C., "The energetics of burrow excavation by the inland robust scorpion, Urodacus yaschenkoi (Birula, 1903)," *Australian Journal of Zoology*, vol. 49, no. 6, pp. 663–674, 2001.

[120] Wieghardt, K., "Experiments in granular flow," *Annual Review of Fluid Mechanics*, vol. 7, pp. 89–114, 1975.

[121] Wong, J., "On the study of wheel-soil interaction," *Journal of Terramechanics*, vol. 21, no. 2, pp. 117–131, 1984.

[122] YAMADA, H. and HIROSE, S., "The Development of Practical 3-dimensional Active Cord Mechanism ACM-R4," *Nippon Kikai Gakkai Robotikusu, Mekatoronikusu Koenkai Koen Ronbunshu (CD-ROM)*, vol. 2005, 2005.

[123] Zufferey, J., Klaptocz, A., Beyeler, A., Nicoud, J., and Floreano, D., "A 10-gram vision-based flying robot," *Advanced Robotics*, vol. 21, no. 14, pp. 1671–1684, 2007.

VITA

Ryan Dominic Maladen was born and grew up in New Delhi, India. He completed his Bachelor of Engineering degree in Electronics from the University of Pune, India, with distinction and was ranked among the top 0.1% in the graduating class of 2002. Motivated to pursue inter-disciplinary research, he joinded the Rehabilitation Laboratory, Center of Biomedical Engineering at the Indian Institute of Technology (IIT), Delhi as a technical associate and worked on assistive technology projects for two years. In 2004, he joined the Biomechanics and Movement Science Program at the University of Delaware where he worked on projects related to functional electrical stimulation of human skeletal muscle in the Department of Physical Therapy. In 2006, Ryan joined the Interdisciplinary Bioengineering Graduate Program at the Georgia Institute of Technology, Atlanta to pursue his doctoral degree. Ryan's PhD research resulted in a several peer-reviewed publications including one in the prestigious journal, Science, and was also featured in the popular press. He was awarded the 'Bud' Suddath award for excellence in bioscience (2009), and the 'Best Paper' award at the Robotics: Science and Systems conference in Zaragoza, Spain (2010). Concurrently with his PhD, Ryan has also earned a certificate in the Management of Technology from the College of Management, Georgia Tech. He was also selected to be part of the Georgia Tech Leadership Program which is aimed at honing value-based leadership awareness and skills. Ryan also met his wife in the Bioengineering Program at Georgia Tech in 2006, and they got married in February, 2009. He successfully defended his doctoral dissertation in November, 2010. In the future, he hopes to pursue a career in research focused on the development of innovative devices for applications in industry.